université de BORDEAUX

THÈSE PRÉSENTÉE

POUR OBTENIR LE GRADE DE

DOCTEUR DE L'UNIVERSITÉ DE BORDEAUX

ÉCOLE DOCTORALE DES SCIENCES PHYSIQUES ET DE L'INGÉNIEUR SPÉCIALITÉ : LASERS, MATIÈRE ET NANOSCIENCES

par Zaicheng Zhang

Nano-Rheology at Soft Interfaces Probed by Atomic Force Microscope

Sous la direction de : M. Abdelhamid MAALI

Soutenue le 30 Octobre 2020

Membres du jury:

M. Alois WÜRGER	Université de Bordeaux, Président
M. Lionel BUREAU	Université Grenoble Alpes, Rapporteur
M. Frédéric RESTAGNO	Université Paris-Saclay, Rapporteur
Mme. Annie COLIN	ESPCI, Université PSL, Examinatrice
M. Carlos DRUMMOND	Université de Bordeaux, Examinateur
M. Thierry ONDARÇUHU	Université de Toulouse, Examinateur
M. Abdelhamid MAALI	Université de Bordeaux, Directeur de thése

Nano-rhéologie aux interfaces molles sondées par microscope à force atomique

Résumé: Des progrès récents dans les études expérimentales et théoriques ont montré que l'écoulement liquide à l'échelle micro/nano se comporte différemment de celui à l'échelle macroscopique. À l'échelle microscopique, les propriétés de surface sont prédominantes pour le comportement d'écoulement proche des parois. Pour un confinement élevé, non seulement la physico-chimie des surfaces de confinement est importante, mais leur comportement élastique doit également être pris en compte. Dans cette thèse, nous avons utilisé l'AFM dynamique pour sonder l'écoulement confiné sur des surfaces molles (bulles d'air et échantillons PDMS) et nous avons montré que:

- A l'interface air-eau, la présence d'impuretés tensioactives modifie le flux à proximité des interfaces de manière drastique, ce qui conduit aux réponses viscoélastiques. Les forces visqueuses et élastiques agissant sur la sphère sont extraites de la mesure du mouvement de la sphère. En raison de la contamination par l'agent tensioactif, la force visqueuse présente un croisement des conditions aux limites antidérapantes aux conditions limites de glissement complet et la force élastique apparaît également avec une valeur comparable à la force visqueuse.
- A faible distance, la pression visqueuse induite par la vibration de la sonde colloïdale déforme la surface de la bulle et donne lieu à l'interaction visco-capillaire. Une excitation par bruit thermique ou une excitation acoustique externe sont utilisées pour entraîner la sonde AFM. Pour expliquer nos mesures, nous avons développé un modèle simplifié basé sur un ressort-dashpot en série et nous avons également effectué la résolution numérique de l'équation de Navier-Stokes combinée à l'équation de Young-Laplace. L'ajustement de nos résultats expérimentaux nous permet de mesurer la tension superficielle de l'interface de la bulle sans contact.
- Le cantilever AFM est un outil puissant pour sonder le mouvement thermique de l'interface de la bulle hémisphérique. Le spectre de telles oscillations thermiques nanométriques de la surface de la bulle présente plusieurs pics de résonance et révèle que la ligne de contact de la bulle hémisphérique est fixée sur le substrat. La viscosité de surface de l'interface bulle due à la contamination par le tensioactif est obtenue à partir de l'analyse de ces pics.
- Une force de portance élastohydrodynamique agit sur la sphère se déplaçant à proximité et le long d'un substrat mou dans un liquide visqueux. La force de levage est sondée en fonction de la taille de l'espace, pour diverses vitesses d'entraînement, viscosités du liquide et rigidité de l'échantillon. À grande distance, les résultats expérimentaux sont en excellent accord avec un modèle développé à partir de la théorie de la lubrification douce. À petite distance de l'espace, une saturation de la force de portance est observée et une loi d'échelle pour cette saturation est donnée et discutée.

Mots-clés : AFM dynamique, Nano-rhéologie, Interfaces molles, Écoulement visqueux, Accouchement, Réponses viscoélastiques

---

Nano-rheology at soft interfaces probed by atomic force microscope

Abstract: Recent progresses in experimental and theoretical studies have shown that the liquid flow at micro/nano scale behaves differently from that at macroscale. At microscale, surface properties are predominant for the flow behavior at the boundaries. For high confinement, not only the physico-chemistry of the confining surfaces are important, their elastic behavior should also be taken into account. In this thesis, we used the dynamic AFM to probe the confined flow at soft surfaces (Air bubbles and PDMS samples) and we have shown that:

- At the air-water interface, the presence of surfactant impurities modifies the flow near the interfaces in a drastic manner, which leads to the viscoelastic responses. The viscous and elastic forces acting on the sphere are extracted from the measurement of the sphere motion. Due to the surfactant contamination, the viscous force shows a crossover from non-slip to full slip boundary conditions and the elastic force also appears with a comparable value to the viscous force.
- At small distance, the viscous pressure induced by the colloidal probe vibration deforms the bubble surface and gives rise to the visco-capillary interaction. Thermal noise excitation or external acoustic excitation are used to drive the AFM probe. To explain our measurements, we have developed a simplified model based on a spring-dashpot in series and we have also performed numerical solution of the Navier-Stokes equation combined with Young-Laplace equation. Fitting our experimental results allow us to measure the surface tension of bubble interface without contact.
- The AFM cantilever is a powerful tool to probe the thermal motion of the hemispherical bubble interface. The spectrum of such nanoscale thermal oscillations of the bubble surface presents several resonance peaks and reveals that the contact line of the hemispherical bubble is fixed on the substrate. The surface viscosity of the bubble interface due to the surfactant contamination is obtained from the analysis of these peaks.
- An elastohydrodynamic lift force is acting on a sphere moving near and along a soft substrate within a viscous liquid. The lift force is probed as a function of the gap size, for various driving velocities, liquid viscosities, and sample stiffnesses. At large distance, the experimental results are in excellent agreement with a model developed from the soft lubrication theory. At small gap distance, a saturation of the lift force is observed and a scaling law for this saturation is given and discussed.

Keywords: Dynamic AFM, Nano-rheology, Soft interfaces, Viscous flow, Confinement, Viscoelastic responses

---

Unité de recherche
UMR 5798 LOMA, Université, 33000 Bordeaux, France.

Acknowledge

Approaching the completion of my thesis, I would like give my appreciation and thanks to all those who have helped and supported me during my study in Bordeaux.

First and foremost, I would like to thank my supervisor, Dr. Abdelhamid Maali. His attitude for doing research impressed me a lot. In my mind, he is a real scientist and one of the most important guiders for me. At the beginning, I was a rookie of researching. He led me into the world of scientific research. He has given me great guidance and encouragement throughout the process of starting the project, designing and doing experiment, operating with atomic force microscope and presenting the scientific results. He taught me hand by hand and I learned a lot from this experience. Not only in the academic study, he gave me a lot of help in the daily life. When I just arrived at Bordeaux, Dr. Maali picked me up and help me to settle in the new life in France. Without him, I would not be able to finish my PhD such smoothly.

I would like to thank the members of the jury for having accepted to evaluate my thesis: thank M. Lionel Bureau and M. Frédéric Restagno to make a report for my manuscript, thank Mme Annie colin, M. Carlos Drummond, M. Thierry Ondarcuhu and M. Alois Würger to exam my defense.

I would also like to thank Dr. Thomas Salez, Prof. Alois Würger, Prof. Hamid Kelly, Prof. Elie Raphaël, Dr. Yacine Amarouchene, Prof. Rodolphe Boisgard, Dr. Christine Grauby-Heywang, Prof. Yuliang Wang. I got much support from them during all projects and they have shown me their great passion for research, which inspired me a lot.

I would like to thank Fabio Pistolesi, Sophie Grandet, Josiane Parzych and Suzanne Bessus for their help for the life in LOMA. I would like to thank Fabien Morote. He gave me a lot of support in the experimental material and help to take imaging using atomic force microscope. I would like to thank the stuff of informatics service: David Riviere, Eric Basier, Alain Bluck, for their support to resolving the problems with compurters. Electronics service: Bernard Tregon, Sébastien Cassagnère and William Benharbone for their help with electronics devices and mechanical service: Anne Tempel and Levi Haelman for their help with the experimental pieces.

Next, I would like to thank my colleagues, Muhammad Arshad, Fredric Dutin, Valerian Freysz, Samir Almohamad for their help during my stay in LOMA. Specially to Vincent Bertin and Marcela Rodriguez Matus, I was happy to collaborate with them to achiever the same goal. I also thank Dongshi Guan, Binglin Zeng, Xiaomeng Cui, Xiaolai Li and Hao Zhang for their comments for my manuscript. Thanks to Maxime Lavaud, Elodie Millan, Nicolas-Alexandre Goy and Gabriel Amiard Hudebine for their help to improve my presentation for the defense.

I would like to thank all my Chinese friends in Bordeaux: Yulin Cai, Hanyang Cao, Zhen Cao, Zhenhui Chen, Wei Chen, Huifang Deng, Miaomiao Guo, Hao Guan, Mengqi Li, Mingzhi Liu, Xinghui Qi, Zhaodan Qin, Zaiyi Shen, Zhengyan Shen, Kaili Xie, Cong Xin, Lina Wang,

Jiaojiao Wang, Ruiqi Wang, Qi Wang, Luming Zhao, Juanjuan Zhang. Without you, the life would be boring in Bordeaux.

I deeply thank my parents and my sister for their unconditional trust and support. Last, I will give my special thank to my wife, Xueping Wang. Thanks for her supporting and understanding. She dedicated enormous time and effort to take care of our daughter and I really appreciate it.

Contents

Acknowledge i

Introduction 1

1 General Methods Used in the Thesis 5

1.1 Description of the AFM . . . 5

1.2 Experimental Methods . . . 10

1.2.1 Attachment of colloidal probe to AFM cantilever . . . 10

1.2.2 Roughness of the colloidal probes . . . 12

1.2.3 Calibration of the piezo . . . 13

1.2.4 Surface tension measurement: Wilhelmy plate method . . . 15

1.3 Calibration of the Cantilever . . . 17

1.3.1 Cantilever motion . . . 17

1.3.2 Thermal noise method . . . 20

1.3.3 The drainage method . . . 24

1.4 Conclusion . . . 27

2 Visco-Elastic Effects at Air-Water Interface: Contamination Effect 29

2.1 Context . . . 29

2.2 Theoretical Model . . . 30

2.2.1 Numerical Calculations . . . 33

2.2.2 Limiting Cases $\omega \ll \omega_0$ and $\omega \gg \omega_0$: Asymptotic Calculation . . . 34

2.2.3 Analytical Calculations using analogy with the disc bubble interaction . . . 35

2.3 Experiment . . . 37

2.3.1 Dynamic AFM method with colloidal probe . . . 37

2.3.2 Results & Discussion . . . 43
2.4 Conclusion . . . 48

3 Visco-Elastic Effects at Air-Water Interface: Capillary Effect 49
3.1 Context . . . 49
3.2 Analytical Model for Visco-Capillary Effect: Simplified Model . . . 50
3.3 Experimental Results . . . 52
3.3.1 Visco-capillary effect studied by thermal noise excitation of the AFM probe . . . 52
3.3.2 Visco-capillary effect studied by acoustic excitation of the AFM probe . . . 56
3.4 Numerical Model for Visco-Capillary Effect . . . 59
3.5 Conclusion . . . 62

4 Thermal Capillary Wave on Hemispherical Bubble Probed by AFM 63
4.1 Context . . . 63
4.2 Modeling of Bubble Shape Vibration . . . 64
4.3 Method and Experimental Results . . . 72
4.3.1 Experimental setup and method . . . 72
4.3.2 Results . . . 75
4.4 Conclusion . . . 79

5 Nanoscale Measurement of the Elastohydrodynamic Lift Force 81
5.1 Context . . . 81
5.2 Methods . . . 84
5.2.1 PDMS samples preparation and characterization . . . 84
5.2.2 Calibration of the piezo . . . 86
5.3 Experiment . . . 88
5.3.1 Experimental Setup . . . 88
5.3.2 Results & Disscussion . . . 90
5.4 Conclusion . . . 95

General Conclusion and Perspective 97

Bibliography 99

Publications 113

Introduction

Recent progresses in experimental and theoretical studies have shown that the liquid flow at micro and nano scales behaves differently to that at macroscale [1, 2]. At microscale, for example, for microfluidic devices, surface properties are predominant for the flow behavior [1, 3]. Such like, the Navier slip length of water, which quantifies the hydrodynamic boundary condition, has been shown with strongly vary with the surface hydrophobicity [4, 5, 6, 7]. In many instances, the liquid-boundary interactions are caused by the presence of molecular solutes or surface charges.

Due to the very low viscosity of the air, an air-water interface is expected to behave as a free surface. In ideal case, the liquid flow should satisfy the full-slip boundary conditions at the air-water interface [8, 9, 10, 11]. However, a recent experimental study showed that the full-slip condition is not realized in general. Measurements of the drag force acting on sphere moving toward the interface corresponds to an intermediate situation [12, 13, 14]. As a possible explanation for this increase of viscous force for the 'bare' water surface, the authors invoked the presence of impurities. Surfactant molecules adsorbed at the interface induce a shear stress that corresponds to the gradient of surface tension and leads to the modification of the flow profile. In some cases, it also leads to viscoelastic behavior. Moreover, surfactant molecules at interfaces give rise to a surface shear viscosity which has been observed through the damping of surface waves [15, 16], the enhancement of the drag coefficient of floating beads [17] or disks [18] and the self-propulsion velocity of colloidal micro-swimmers [19].

For high confinement, not only the physico-chemistry of the confining surfaces are important, their elastic behavior also should be taken into account. Indeed, at small gap, the hydrodynamic pressure between the confining surfaces can be very large, which may induce elastic deformation of the surfaces. Elastohydrodynamic is the generic term used to describe the hydrodynamic coupling between the liquid flow and the elastic deformation of the confining surfaces. Much attention was given to the study of this effect at microscale in the last decade using optical microscopy, Surface Force Apparatus (SFA) and Atomic Force Microscopy (AFM). Based on this elastohydrodynamic coupling, new tools were developed to probe the mechanical properties of soft interfaces without contact. For example, using dynamic SFA [20, 21, 22] and AFM [23, 24], the mechanical properties of several surfaces have been measured.

In such a context, a novel elastohydrodynamic lift force was theoretically predicted for an object moving past soft surface within a fluid. This force arises from a symmetry breaking in the contact shape and the associated flow, due to the elastohydrodynamic coupling introduced

above. Specifically, for a non-deformable surface (rigid surface), the contact shape and even the lubrication pressure field (*i.e.* the dominant hydrodynamic stress) are antisymmetric, resulting in no normal force. In contrast, a soft surface is deformed by the pressure field which then loses its symmetry, resulting in a finite normal lift force. The lift force effect was calculated for different elastic media and geometries [25, 26, 27], added effects of intermolecular interactions [28], self-similar properties of the soft lubricated contact [29], the inertial-like motion of a free particle a [30], viscoelastic effects [31], the motion of vesicles along a wall [32, 33], and the case of membranes [34, 35]. Theoretical calculations show that, as the gap between the object and the soft substrate reduces, the force increases. Eventually, at very small gap, the competition between symmetry breaking and decreasing pressure leads to a saturation of the lift force [25, 26, 27, 28]. Despite the abundant theoretical literature, experimental evidence for such an elastohydrodynamic lift force remains recent and scarce [36, 37].

In this thesis, we have used AFM to study some aspects of soft interfaces introduced above. The manuscript is organized as follows:

- In chapter 1, we will address the tools and methods used during this thesis. First, I will introduce, the experimental setup, the process of preparation of the colloidal probe, the calibration of the piezo stage and the Wilhelmy plate method used to measure the surface tension. Second, two methods of AFM cantilever calibration will be presented: thermal noise method and the drainage method.

- Chapter 2 is dedicated to the study of the viscoelastic properties of the air-water interfaces due to the surfactant contamination. We will show that vibrating a small sphere mounted on an AFM cantilever near a gas bubble immersed in water is an excellent probe of surface contamination. Both viscous and elastic forces are exerted by an air-water interface on the vibrating sphere even when very low doses of contaminants is present. The viscous drag force shows a crossover from no-slip to slip boundary conditions while the elastic force shows a nontrivial variation as the vibration frequency changes. We provide a model to explain these results and propose a simple way of evaluating the concentration of such surface impurities.

- In chapter 3, the study of the visco-capillary coupling between an oscillating colloidal probe and a bubble will be presented. The measurements are performed using two different methods for the cantilever driving, one with a thermal noise driving and the other one with acoustic external driving. To investigate the interaction at very small distance, we have performed numerical calculation to solve the combined Navier-Stokes and Young-Laplace equations in the frame of lubrication approximation. The numerical calculations are in a good agreement with the experimental results and allow us to measure the surface tension of bubble interface without contact.

- In chapter 4, we will present the measurements of the thermal capillary fluctuation of a bubble deposited on solid substrates. The cantilever deflection signal can reflect the thermal fluctuation of the bubble surface directly. The spectrum of the thermal fluctuation

presents sharp resonance peaks for specific frequencies where the motion of the interface is much more important than that for other frequencies. The analysis of these peaks allows to measure the resonance frequencies, effective mass and the damping coefficient for each mode of oscillation. To explain the experimental results, we will present a model for the bubble shape oscillation. The experimental results show that the contact line of a hemispherical bubble resting on a solid surface is fixed on the substrate. The measurement of additional damping due to the presence of minute amounts of contaminants allows us to extract the surface viscosity of the bubble surface

- In chapter 5, we will report the experimental study of the lift force acting on spherical particle moving along thick, soft samples in viscous liquid. We will show that, as the gap between the sphere and the sample is reduced, a lift force acting on the sphere is observed, and increases with a power law of -5/2. Moreover, the measurements for various amplitudes, frequencies, viscosities, and Young moduli collapse will be shown and the experimental results will be compared with the prediction based on the soft lubrication theory. At small distance, a saturation of the lift force is observed and a scaling law will be discussed.

Chapter 1

General Methods Used in the Thesis

Contents

1.1 Description of the AFM 5
1.2 Experimental Methods 10
1.2.1 Attachment of colloidal probe to AFM cantilever 10
1.2.2 Roughness of the colloidal probes 12
1.2.3 Calibration of the piezo 13
1.2.4 Surface tension measurement: Wilhelmy plate method 15
1.3 Calibration of the Cantilever 17
1.3.1 Cantilever motion 17
1.3.2 Thermal noise method 20
1.3.3 The drainage method 24
1.4 Conclusion 27

1.1 Description of the AFM

Since the invention of Atomic Force Microscope (AFM) by Binning et al. [38] in 1986, it has been widely used for topography imaging of both conducting and insulating surfaces up to atomic resolution. AFM exceeds the limitation of Scanning Tunneling Microscope (STM) [39] which only allows the imaging of conducting and semiconducting surfaces.

Figure 1.1 shows the Bioscopy II AFM (Bruker, USA) that is used for experimental work presented in this thesis. The schematic of an AFM is shown in Fig. 1.2. A cantilever with a sharp tip (see Fig. 1.3a) is fixed on a cantilever holder (see Fig. 1.3b) or a liquid cell (see Fig. 1.3c). The backside of the cantilever is usually coated with a thin gold or aluminum layer to enhance its optical reflectivity. When it works, a laser beam is focused on the end of the cantilever which

is placed on the AFM's head scanner. Then the position of the reflected laser beam is monitored by a four quadrant photo detector. For any variation of the cantilever deflection, the position of reflected laser beam on the the photo detector will change. Therefore, the motion of the cantilever can be traced by the photo detector signal.

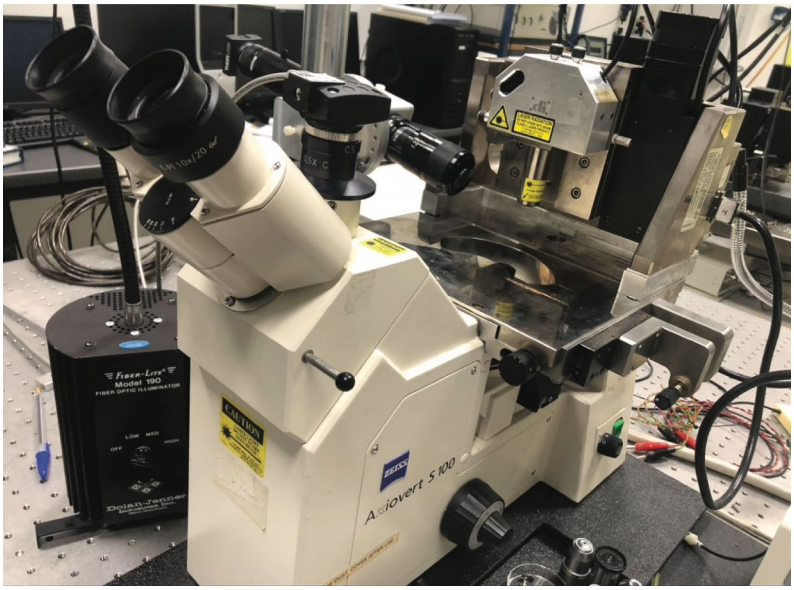

Figure 1.1: *The Bioscope II AFM.*

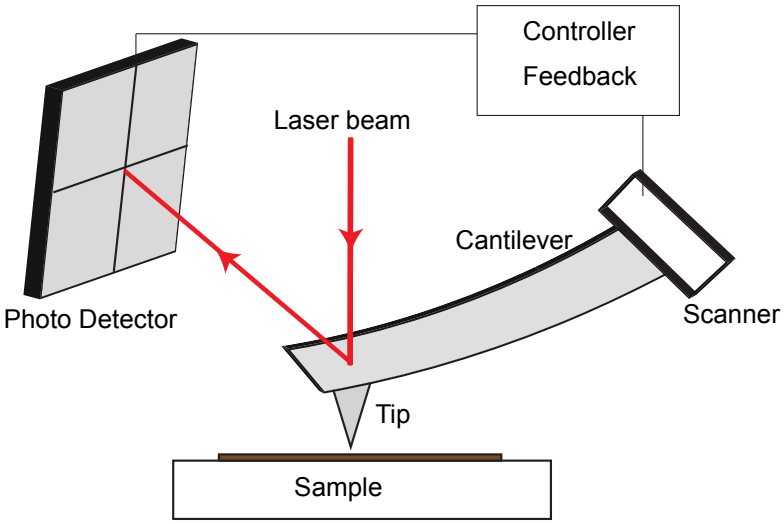

Figure 1.2: *Schematic of AFM.*

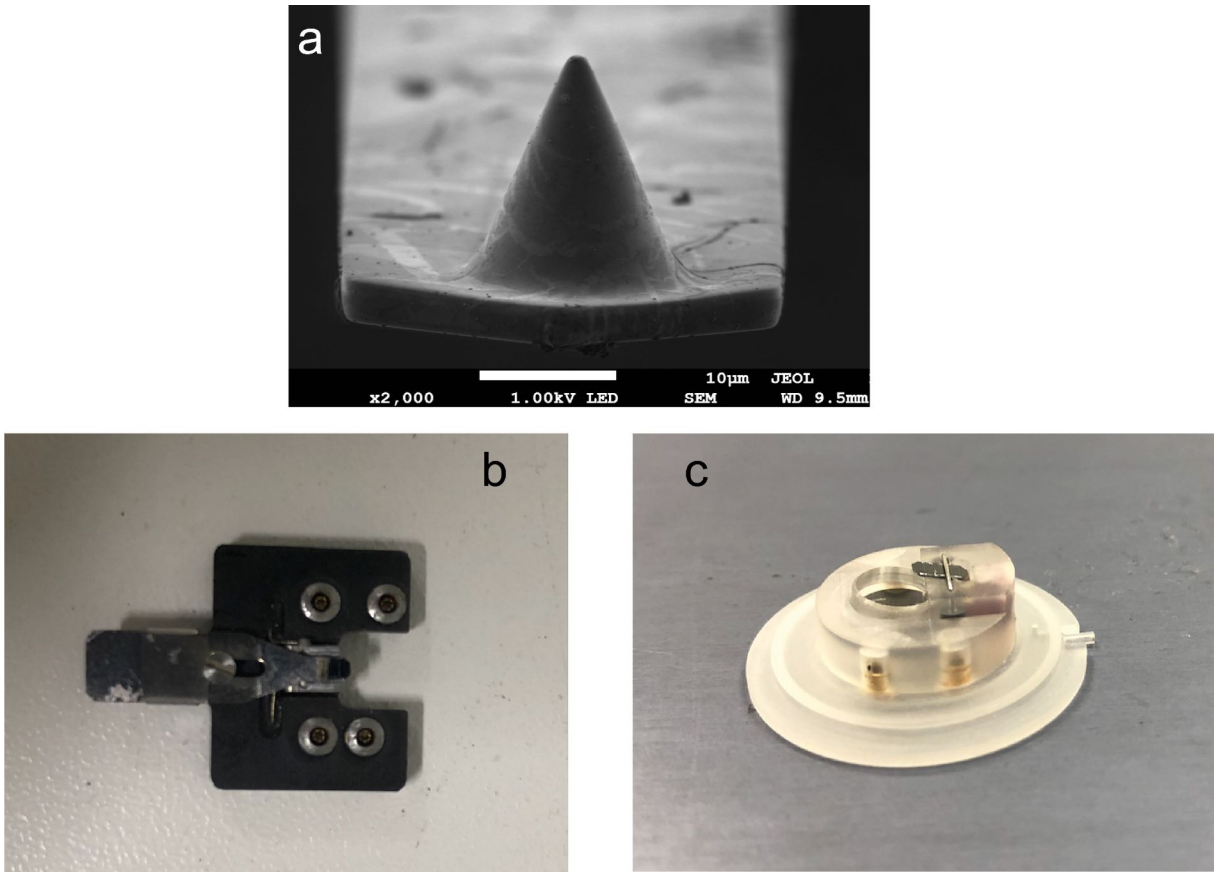

Figure 1.3: ***a**) A SEM image of cantilever (LRCH tip, 225 C3.0-R). **b**) A cantilever holder for imaging in air or in vacuum. **c**) A liquid cell for imaging in liquid medium.*

AFM imaging

The imaging by AFM is usually operated in one of two modes: contact mode (static mode) or dynamic mode.

Contact mode is the basic mode in which the cantilever probe is in contact with the sample during the scanning. As the tip moves along the surface, the topography of sample induces a vertical deflection of the cantilever. To maintain the deflection at a constant value during the scanning, the feedback loop imposes to the piezo a vertical displacement that corresponds to the local height of the topography of the imaged sample. By recording the height information at each point of the sample, the topographic image is generated. Generally, in contact mode, a soft cantilever is used to avoid the deformation of the sample.

Dynamic modes are emerging as powerful tools for nanometer and atomic scale characterization and manipulation of a wide variety of surfaces. One of the major dynamic AFM modes is Amplitude Modulation Atomic Force Microscope (AM-AFM, tapping mode AFM) [38], and the other one is Frequency Modulation Atomic Microscope (FM-AFM) [40]. In AM-AFM, a

stiff cantilever is excited near its free resonance frequency, and the amplitude and phase of the cantilever oscillation are measured. For the acquisition of the image, the amplitude is kept as constant at a given value via the feedback loop [41]. In AM-AFM mode, in addition to the topography image, a phase image is recorded which corresponds to the variation of the properties in heterogeneous sample. The AM-AFM is usually used to image the soft material without destroying the interface. Figure 1.4 shows an example of AM-AFM mode image of nanobubbles on a polystyrene surface.

In contrast to AM-AFM, in FM-AFM mode, the cantilever acts as the oscillator in an active feedback loop (Phase-Locked Loop, PLL). The resonant frequency value of the cantilever depends on the interaction force between the cantilever tip and sample. Changes in the resonant frequency are detected by a frequency modulation demodulator of the PLL. The feedback is used to keep the cantilever oscillating at the given resonant frequency during the acquisition of the image. To compensate the dissipation due to the interaction with the sample that reduces the amplitude of the cantilever, the feedback monitors the excitation force to keep constant oscillation amplitude [40, 42].

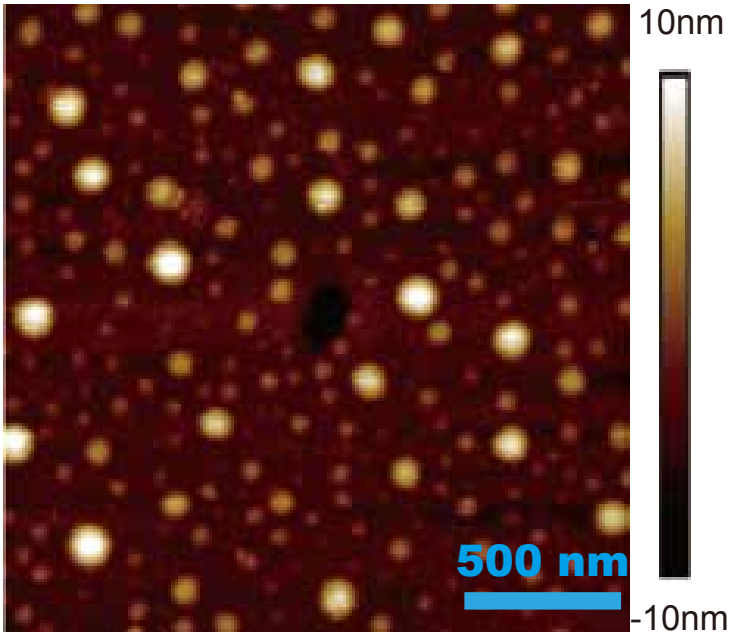

Figure 1.4: *An AFM image of nanobubbles on polystyrene surface measured in AM-AFM mode.*

Force curve

AFM is a powerful tool, not only can image the topography of surfaces but also measure surface forces. The colloidal probe AFM measurement was first introduced by Ducker *et al.* [43, 44] and then by Butt [45], and now it becomes a well-established and powerful tool for the study of surface forces [46]. The force versus distance curves (*i.e.* force curves) record the vertical

position of the tip and the deflection of cantilever in contact mode. Data from such force curves provides valuable information for studing surface forces and material properties like elasticity, hardness, Hamaker constant, adhesion and surface charge densities, etc [47]. By analyzing the force curve, we can study the interaction between particles or between particle and interface in a fluid. When a force is applied to the probe, the cantilever deflects and the reflected light beam moves on the four quadrant photo detector.

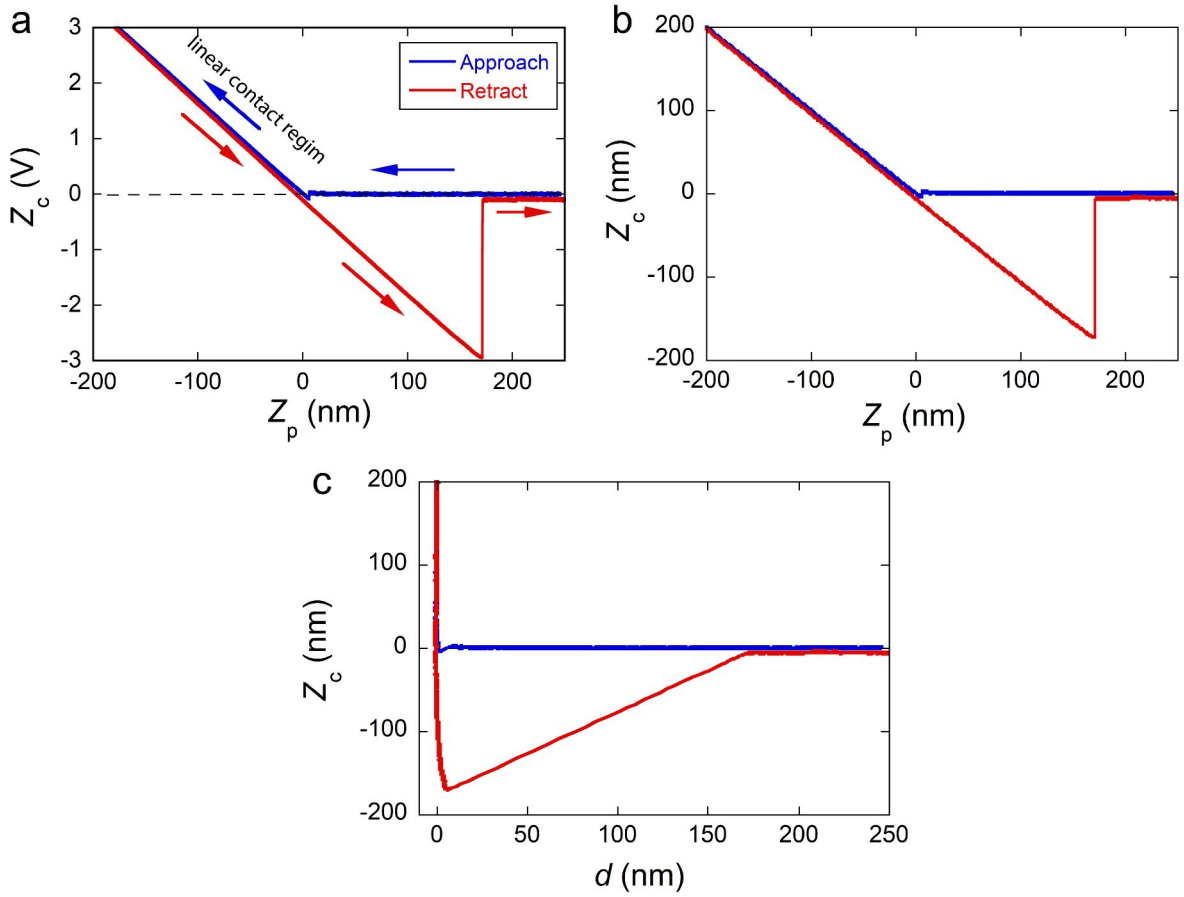

Figure 1.5: *The force curve obtained with cantilever (MLCT type B, Bruker) on mica surface in air using the Bioscope II AFM (Bruker).* ***a****) The cantilever deflection (Z_{c}) in volts versus piezo displacement (Z_{p}) that was obtained directly from the photo detector.* ***b****) The deflection is converted into nm by multiplying the measured deflection in volts with the value of the sensitivity (sens $= 58.4\ \mathrm{nm/V}$).* ***c****) The corresponding Z_{c} versus d plot, with $d = Z_{\mathrm{p}} + Z_{\mathrm{c}}$.*

The detector measures the deflection of the cantilever(Z_{c}) in voltage versus the piezo displacement (Z_{p}) (see Fig. 1.5a). To obtain the force curve, the deflection has to be converted into nm by multiplying the measured deflection in volts with the value of the sensitivity expressed in nm/V. To get the value of the sensitivity, we fit the linear contact regime (hard contact between the tip and hard sample, see Fig. 1.5a), and we get the relation between the measured

deflection in volts and the piezo displacement in nm, $Z_c(V) = kZ_p$. For a hard sample, the piezo displacement should be equal to the cantilever deflection, $Z_c(nm) = Z_p = Z_c(V)/k$ in the hard contact regime, and then the sensitivity is equal to: sens $= 1/k$. Finally, the tip-sample separation distance is obtained by adding the cantilever deflection to the piezo displacement (ie. $d = Z_p + Z_c$) (see Fig. 1.5c). Knowing the spring constant of the cantilever (k_c), the deflection can easily be converted into a force: $F = k_c Z_c$.

1.2 Experimental Methods

1.2.1 Attachment of colloidal probe to AFM cantilever

The colloidal probe has the advantage of well-defined geometry and controllable size, which simplifies the modeling of the interaction forces. Furthermore, for large sphere size, the lubrication approximation is also satisfied even for large separations. Successful and accurate measurement at nano-metric scale requires appropriate preparation of colloidal probes and free from contamination at their surfaces. A home made three-axis motion stage is used to attach the sphere to the end of the cantilever. As shown in Fig. 1.6, the stage is placed on the optical microscope (B2 series, Motic microscope). The attachment process is performed in the following steps:

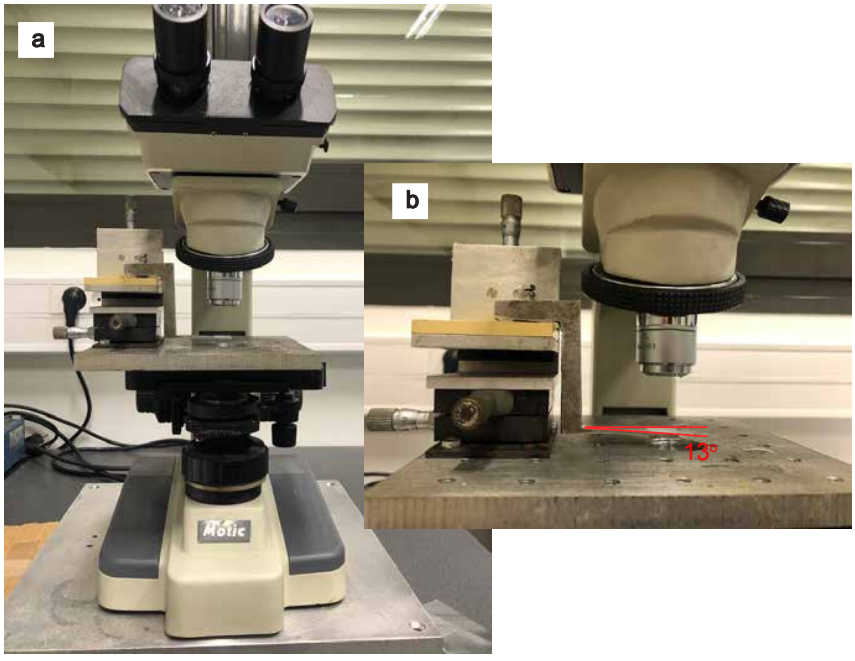

Figure 1.6: *The stage used to make colloidal probes.*

- Step 1: The particles are first washed with hellmanex solution followed by a rinsing with pure water and then cleaned with anhydrous ethanol solution under ultrasonic treatment for tens of minutes. The process of cleaning with ethanol is repeated several times.
- Step 2: We shake the ethanol solution containing the particles gently to make the particles more evenly distributed in the solution, and spread a drop of this solution on cleaned glass surface. After the evaporation of the ethanol, the cleaned particles are left on the glass surface (see Fig. 1.7 a-b).

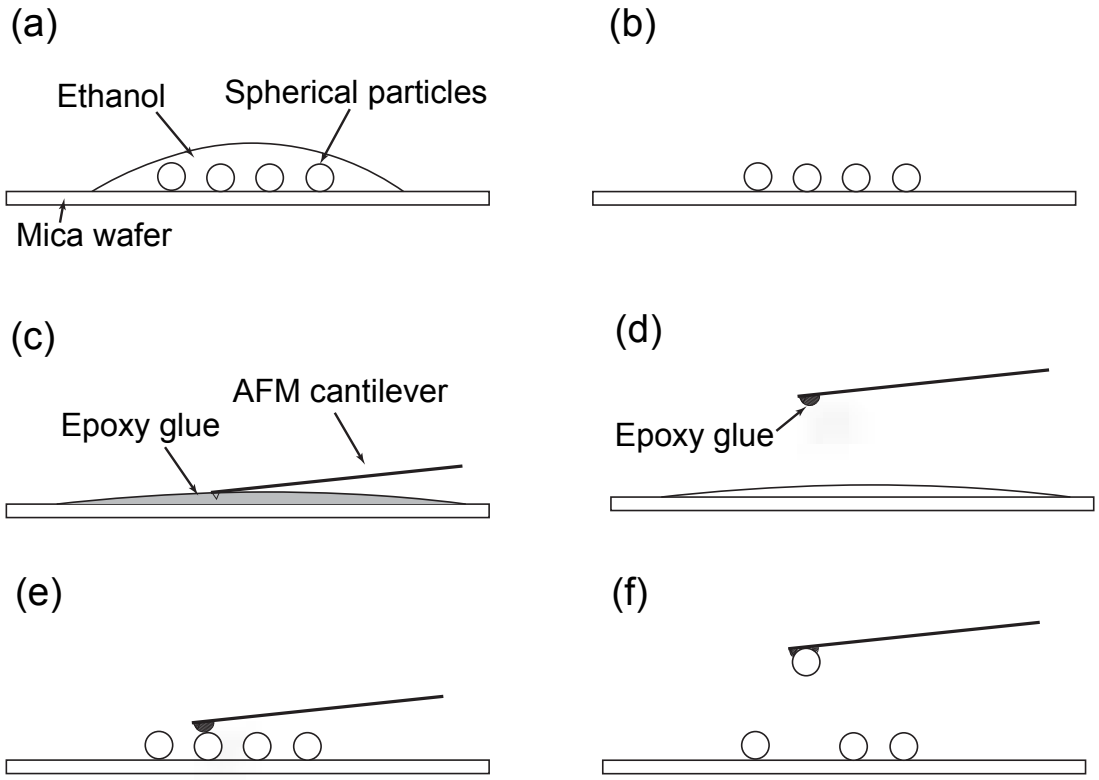

Figure 1.7: *The process of making colloidal probes.* ***a****) The colloidal particles in ethanol solution are spread on the mica surface.* ***b****) After the evaporation of the ethanol, the particles are left on the surface.* ***c****) The AFM cantilever contacts with epoxy glue to wet the cantilever.* ***d****) The glue is attached on the cantilever.* ***e****) The wetted cantilever contacts the colloidal particle.* ***f****) The colloidal particle is glued to the end of the cantilever.*

- Step 3: We deposit a very thin layer of epoxy glue (Araldite Rapid) on another piece of glass surface, and place an AFM cantilever on the leg of the three-axis platform with an angle around $13\ ^\circ$ with respect to the horizontal direction (see Fig. 1.6b). Under the microscope, bring down the AFM cantilever to touch with the epoxy glue layer. After lifting the cantilever up, a small amount of glue is attached on the edge of the cantilever (see Fig. 1.7 c-d).

- Step 4: We replace glass surface containing the glue with that containing particles, and bring down the cantilever to be in contact with one of the particles. After several minutes for the cross-link of the epoxy glue, the cleaned particle will be glued on the AFM cantilever (see Fig. 1.7 e-f). An attached colloidal probe is shown in Fig. 1.8. The size of the particle can be obtained from this optical image.

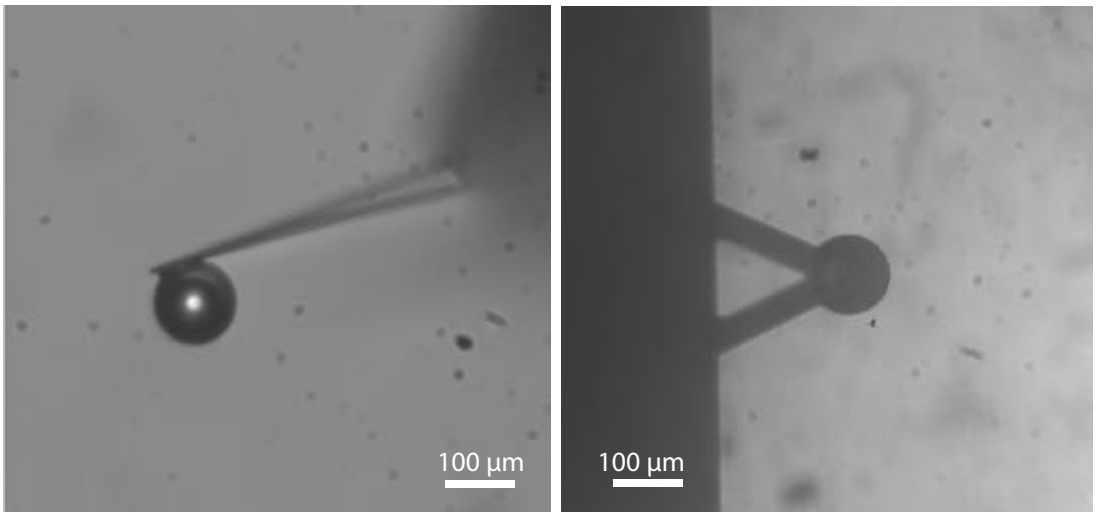

Figure 1.8: *Optical images of the particle which was glued on the end of a V-shaped cantilever (SNL-10, Bruker).*

1.2.2 Roughness of the colloidal probes

Using AFM, the roughnesses and the radius of the colloidal probe can easily be obtained. Figure 1.9a shows the 3D AFM image of a spherical borosilicate particle (MO-Sci Corporation) obtained in contact mode. The size of the imaged area is $10\ \mu\mathrm{m} \times 10\ \mu\mathrm{m}$. In Fig. 1.9b, the open circles shows the height section (the red line in Fig. 1.9a) and the solid line represents the fitting curve using the circle equation. The fitted radius for this colloidal sphere is $R = 47 \pm 0.5\ \mu\mathrm{m}$.

Figure 1.9c shows the plane fitted image with a size of $1\ \mu\mathrm{m} \times 1\ \mu\mathrm{m}$ and Fig. 1.9d shows the height section (the green line in Fig. 1.9c), where the modulation of the surface height is presented clearly. The roughness measured on this image is Rq $= 0.5 \pm 0.1$ nm, where Rq is the root mean squared roughness.

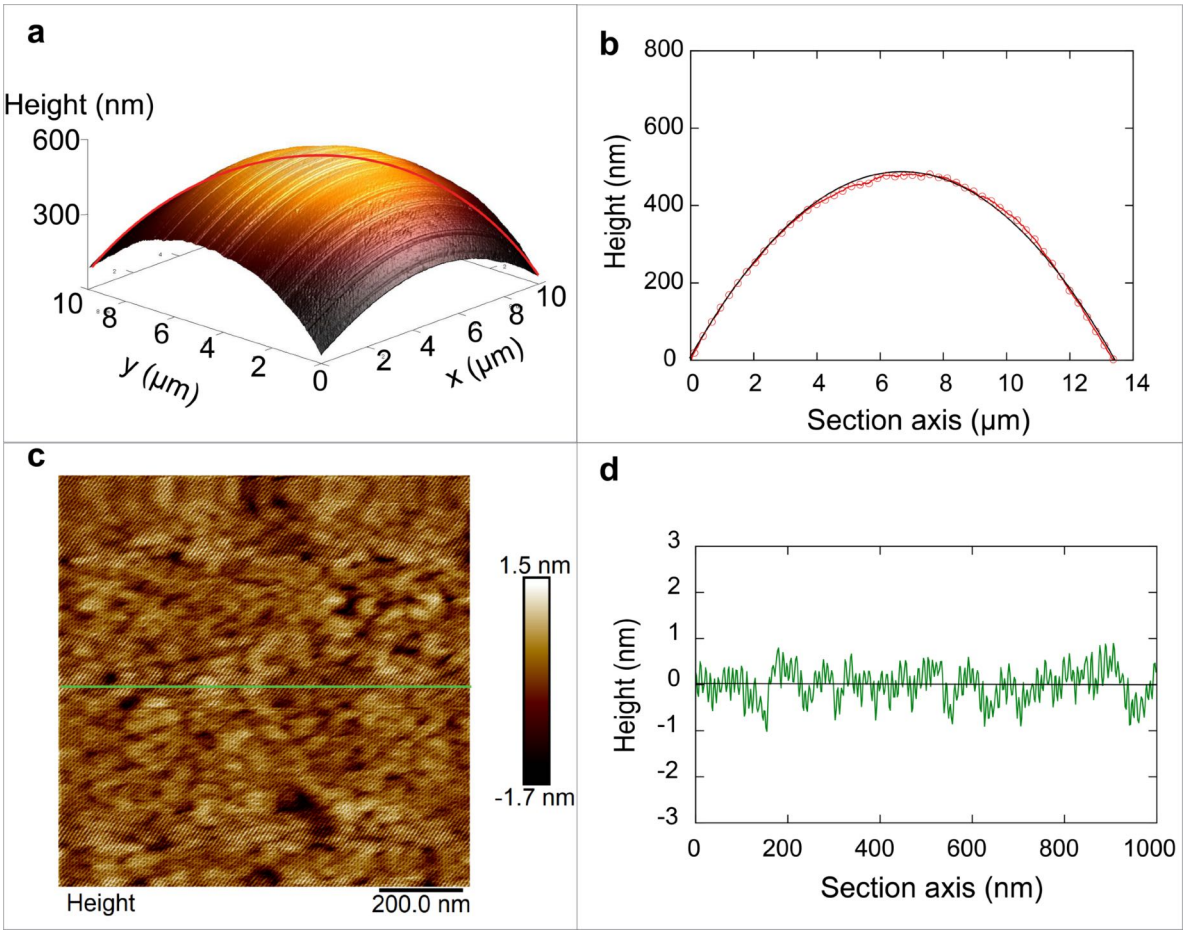

Figure 1.9: ***a)*** *The 3D AFM height image for a spherical colloidal particle with a size of* $10\ \mu\text{m} \times 10\ \mu\text{m}$. ***b)*** *The plot of height section along the direction of the red line in* ***a****. From the fitting of the height section using circle equation, the radius of the particle is obtained as* $R = 47 \pm 0.5\ \mu\text{m}$. ***c)*** *The plane fitted height image of the particle with a size of* $1\ \mu\text{m} \times 1\ \mu\text{m}$*, from which we get the roughness is Rq* $= 0.5 \pm 0.1$ *nm.* ***d)*** *The height section of the plane fitted image at the positioin of the green line in* ***c****.*

1.2.3 Calibration of the piezo

In the measurement by AFM, a piezoelectric system is used to scan the sample in either vertical direction or lateral direction. In this thesis, a piezo from MAD CITY LABS with a large travel range (see Fig 1.10) is used to control the position of the samples. An accurate calibration of the displacements of the piezo as a function of the applied voltage is necessary to obtain quantitative information about the motion. A number of methods [48, 49, 50, 51, 52] have been developed to calibrate the piezo. We have calibrated the piezo using optical camera, which is simple and with a good accuracy.

A microscopic calibrated slide (Motic) is chosen and fixed on the piezo stage. The calibrated

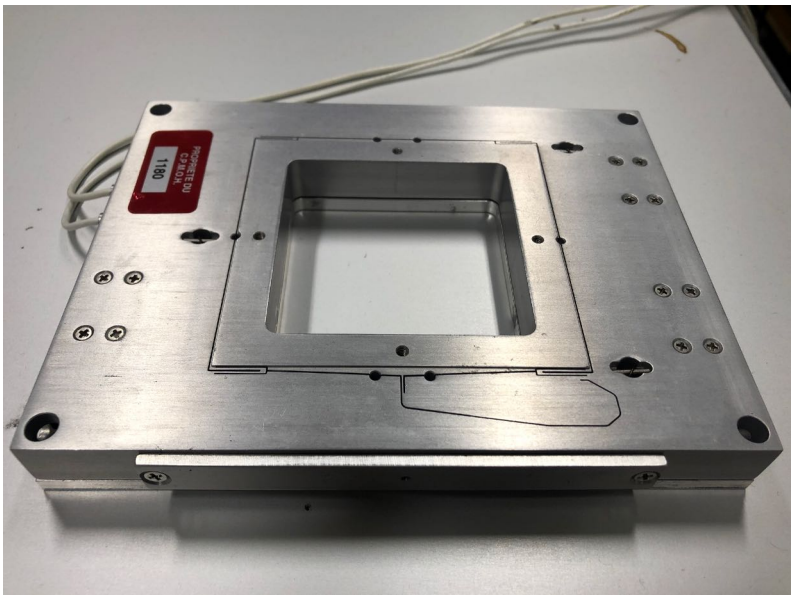

Figure 1.10: *Image of the piezo (NanoT series, MAD CITY LABS) used in the thesis.*

slide contains calibrated girds and several disk with different sizes. We apply voltage to the piezo at a given frequency. A camera (DCC1545M, Thorlabs) is used to track the motion of one of the disks. As shown in Fig. 1.11, the image of the calibrated disk with a radius of $75\ \mu\mathrm{m}$ is obtained. From the image, we calibrate the pixel. The displacement of the piezo can be obtained from two extreme positions of the disk.

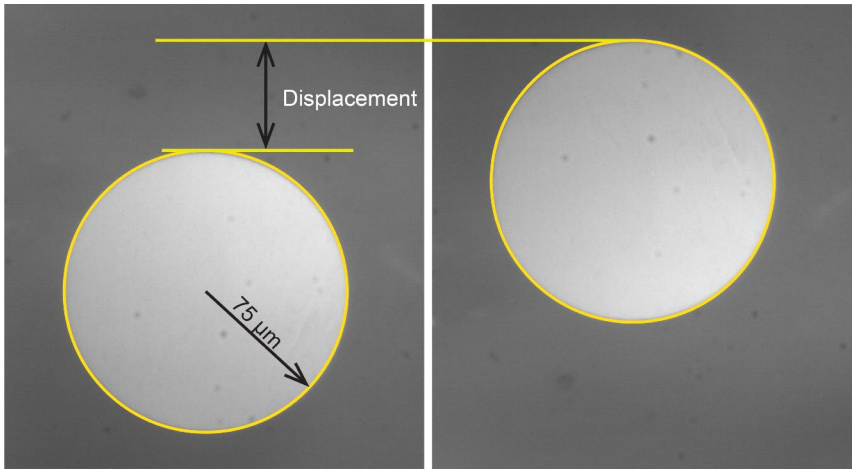

Figure 1.11: *Image of the disk driven by the piezo.*

We calibrate the piezo at $0.1\ \mathrm{Hz}$ with different driving amplitudes. The results are shown in Fig 1.12. From the linear fitting of results, we get the piezo displacement per volt equals to $4.9 \pm 0.03\ \mu\mathrm{m/V}$.

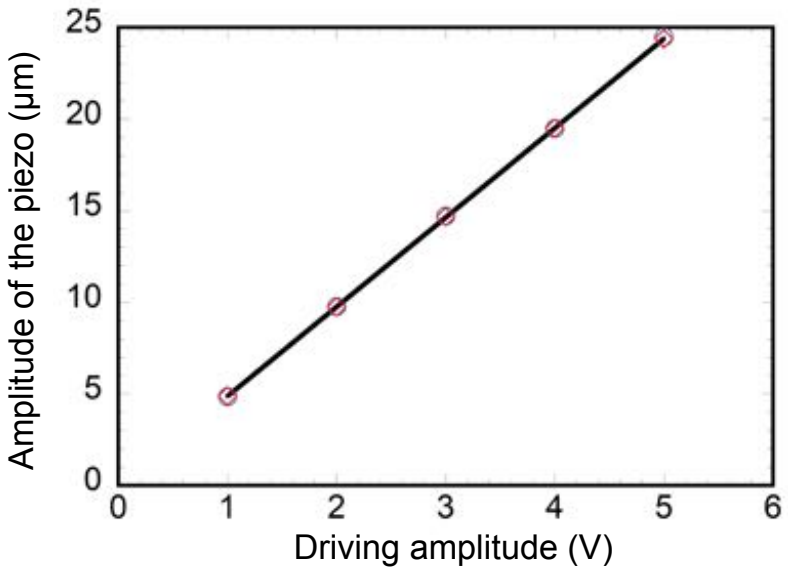

Figure 1.12: *The amplitudes of the piezo displacement measured by the camera versus driving amplitudes in volt (at 0.1 Hz). The black line is the linear fitting curve from which we get the displacement of the piezo per unit voltage equals to* $4.9 \pm 0.03\ \mu\mathrm{m/V}$.

1.2.4 Surface tension measurement: Wilhelmy plate method

In this thesis, the Wilhelmy plate method is used to measure the surface tension of air-water interface. Figure 1.13 shows the schematic of the static Wilhelmy plate measurement. A thin plate is held at the air-water interface, which gives rise to the capillary force F:

$$F = \sigma l_{\mathrm{p}} \cos(\theta_{\mathrm{c}}), \tag{1.1}$$

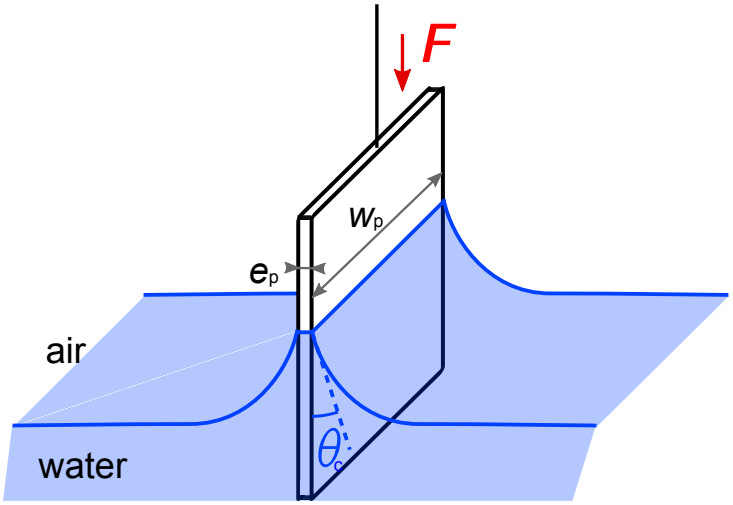

Figure 1.13: *The schematic of static Wilhelmy plate measurement.*

where σ is the surface tension of the interface, $l_\mathrm{p} = 2(w_\mathrm{p} + e_\mathrm{p})$ is the perimeter of the contact line on the plate, e_p is the thickness of the plate, w_p is the width of the plate, and θ_c is the contact angle between the water and the plate as shown in Fig. 1.13.

In the laboratory, a tensiometer from Nima technology (see Fig. 1.14) with a Whatman chromatography paper is used to perform the Wilhelmy plate measurement. As the paper is brought into contact with the water surface, the tensiometer will detect the exact amount of the tension acting on the plate at the position of the plate before it snaps off from the surface. The contact angle here is equal to $0°$.

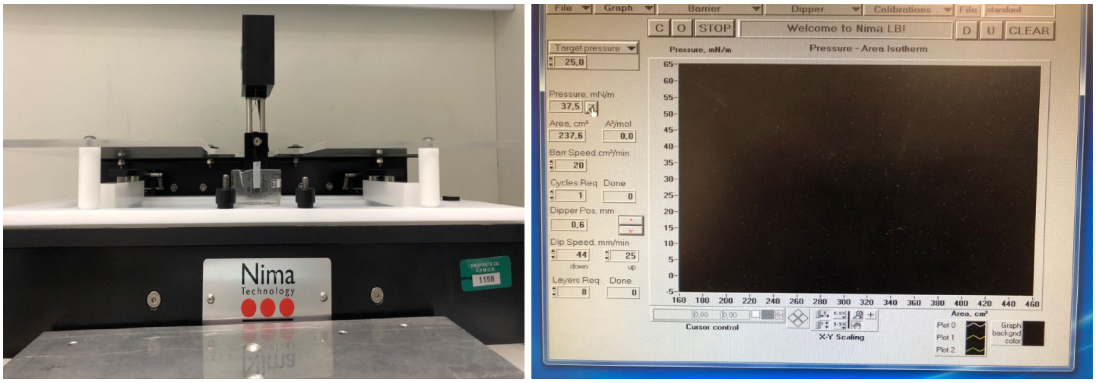

Figure 1.14: *The system to perform Wilhelmy plate measurement.* ***a****) The tensiometer from Nima technology.* ***b****) The operation software for the tensiometer.*

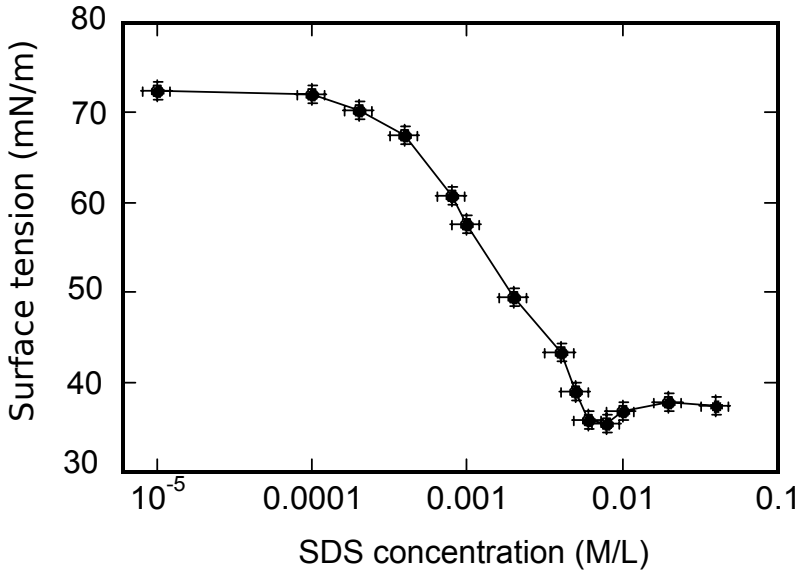

Figure 1.15: *The measured surface tension as a function of the concentration of SDS solutions.*

Figure 1.15 shows the measured surface tension with different concentrations of SDS (Sodium Dodecyl Sulfate) solutions. In this measurement, a paper plate with a thickness of $e_\mathrm{p} = 918\ \mathrm{nm}$

and width of $w_p = 20.50$ mm was used as Wilhelmy plate. In order to minimize the error, the measurements were performed from low concentrations to high concentrations of SDS solutions.

1.3 Calibration of the Cantilever

1.3.1 Cantilever motion

As shown in Fig. 1.16, the cantilever is considered as a beam with length of l, width of w and thickness of e.

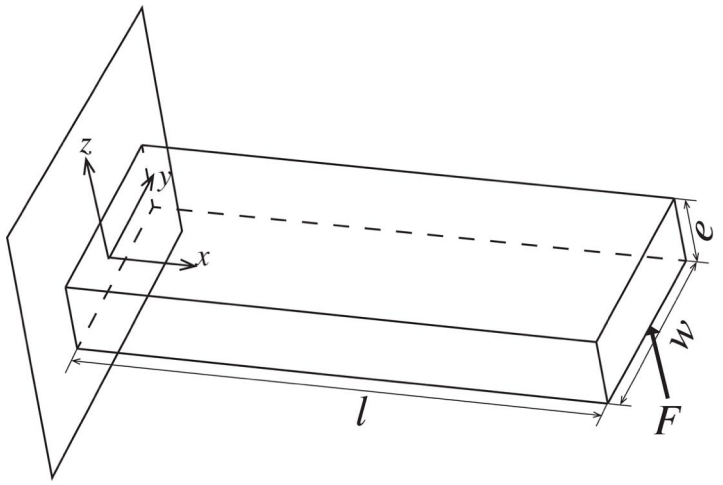

Figure 1.16: *Schematic of the cantilever with a length of l, a width of w and a thickness of e. A force F is applied to the end of the cantilever in z direction.*

In the static situation, the cantilever is deflected by a constant force F, and we have

$$EI\frac{\partial^3 Z(x)}{\partial x^3} = -F, \tag{1.2}$$

where E is the Young's modulus of the cantilever, $I = we^3/12$ is the area moment of inertia of the beam, and Z is cantilever deflection in z direction. Integrating Eq. (1.2) with boundary conditions of $\frac{\partial z(x=0)}{\partial x} = 0$, $\frac{\partial^2 z(x=l)}{\partial x^2} = 0$, we have

$$\frac{\partial Z\,(x)}{\partial x} = \frac{F}{EI}(lx - \frac{x^2}{2}). \tag{1.3}$$

At the end of the beam, Eq. (1.3) becomes to

$$\frac{\partial Z\,(x=l)}{\partial x} = \frac{Fl^2}{2EI} = \frac{F}{k_c}\frac{3}{2l} = \frac{3}{2l}Z(x=l), \tag{1.4}$$

where

$$k_{\mathrm{c}} = \frac{3EI}{l^3} = \frac{Ewe^3}{4l^3} \tag{1.5}$$

is the definition of the cantilever stiffness, and $Z\left(x=l\right) = F/k_{\mathrm{c}}$ is the deflection of the cantilever induced by the applied force.

Standard AFM uses optical deflection method to measure the motion of the cantilever. In this method, the inclination at the end of the cantilever $\mathrm{d}Z(x=l)/\mathrm{d}x$ is measured rather than the cantilever deflection $Z(x=l)$ itself. The corresponding deflection Z_c[1] is determined by the inclination $\mathrm{d}Z(x=l)/\mathrm{d}x$ of the cantilever at the end, multiplied by the factor $2l/3$ [53], *i.e.*

$$Z_c = Z(x=l) = \frac{2l}{3}\frac{\partial Z(x=l)}{\partial x}. \tag{1.6}$$

For the dynamic motion of the cantilever, the bending of the cantilever is described by Euler-Bernoulli theory, which is given by

$$EI\frac{\partial^4 Z}{\partial x^4} + \rho_{\mathrm{c}} we\frac{\partial^2 Z}{\partial t^2} = 0, \tag{1.7}$$

where ρ_{c} is the density of the cantilever material. The solution of Eq. (1.7) is given in the form:

$$Z(x,t) = \chi(x)a(t), \tag{1.8}$$

with $a(t)$ is the amplitude of the cantilever vibration and $\chi(x)$ is the beam profile of the cantilever. Substituting Eq. (1.8) into Eq. (1.7), we have

$$\frac{\partial^4\chi(x)}{\partial x^4} = \frac{\alpha^4}{l^4}\chi(x), \tag{1.9}$$

where

$$\alpha^4 = \frac{12\rho_{\mathrm{c}}\omega^2 l^4}{Ee^2} \tag{1.10}$$

and ω is the angular frequency of cantilever. For the cantilever with a free end, $\chi(x)$ must satisfies the boundary conditions [53, 54, 55]:

$$\chi(0) = 0, \frac{\mathrm{d}\chi(0)}{\mathrm{d}x} = 0, \frac{\mathrm{d}^2\chi(l)}{\mathrm{d}x^2} = 0, \frac{\mathrm{d}^3\chi(l)}{\mathrm{d}x^3} = 0.$$

Using the normalization of $\chi\left(x=l\right) = 1$, we get

$$\chi(x) = \frac{1}{2}\left(\left(\cos\frac{\alpha}{l}x - \cosh\frac{\alpha}{l}x\right) - \frac{(\cos\alpha + \cosh\alpha)}{(\sin\alpha + \sinh\alpha)}\left(\sin\frac{\alpha}{l}x - \sinh\frac{\alpha}{l}x\right)\right), \tag{1.11}$$

with

$$\cos\alpha\cosh\alpha + 1 = 0. \tag{1.12}$$

i	1	2	3	4	5	6
α_i	1.875	4.694	7.855	10.995	14.137	17.279

Table 1.1: *The values of α_i for free end cantilever, and the subscript of i indicates the mode number.*

The solutions of Eq. (1.12) give different values of α corresponding to each mode of the cantilever vibration. The values of α for the first six modes are presented in Tab. 1.1. Here we denote i as the mode number of the cantilever vibration.

From Eq. (1.10), the resonance frequencies of the cantilever for each mode can be obtained as

$$\omega_i^2 = \frac{Ee^2\alpha_i^4}{12\rho_c l^4}. \tag{1.13}$$

Here, we introduce the effective mass $m^* = \rho_c we \int_0^l (\chi(x))^2 dx = \rho_c lwe/4$ of the cantilever [47, 54]. Eq. (1.13) becomes to

$$\omega_i^2 = \frac{k_i}{m^*}, \tag{1.14}$$

where the cantilever stiffness for mode i is given by

$$k_i = \frac{\alpha_i^4}{12} k_c. \tag{1.15}$$

In Fig. 1.17, the cantilever shapes for the first six modes are presented.

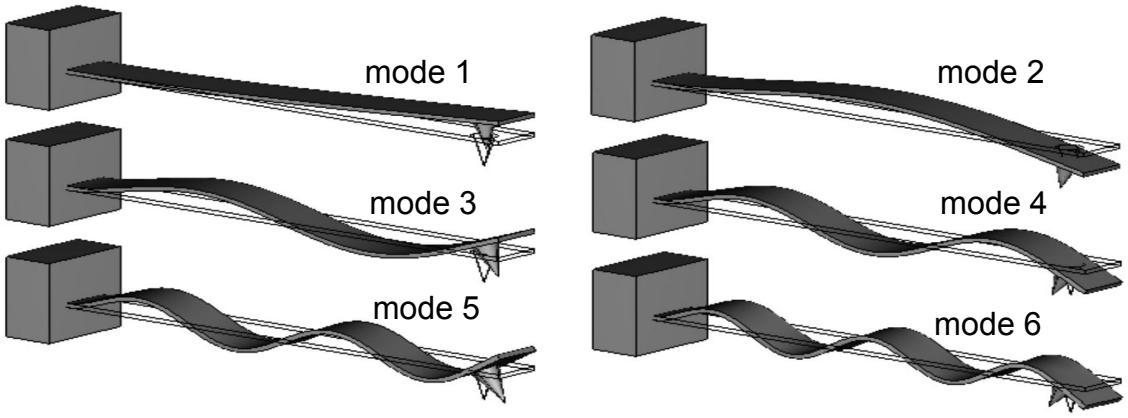

Figure 1.17: *The cantilever shape for the first six modes of a rectangular cantilever with a free end.*

Finally, we inject Eq. (1.11) and Eq. (1.8) into Eq. (1.6), to express the time dependent

[1]Notice that Z_c is not measured directly, but it is deduced from the measurement of the inclination at the end of the cantilever.

deflection of the cantilever for the mode corresponding to α_i,

$$Z_{\mathrm{c}}(t)_i = \frac{2\alpha_i}{3}\frac{\sin\alpha_i \sinh\alpha_i}{\sin\alpha_i + \sinh\alpha_i} a(t)_i, \tag{1.16}$$

Note here, the prefactor of $2/3$ in Eq. (1.16) comes from the fact that the deflection is inferred from the inclination of the cantilever.

1.3.2 Thermal noise method

As described in the previous section, to extract accurate values for the forces from the cantilever deflection, the spring constant of the cantilever k_{c} has to be determined precisely. In principle, the spring constant of the cantilever can be calculated from the geometric dimensions and the properties of the material (Young's modulus) by Eq. (1.5) [56, 57, 58]. However, the thickness and elastic modulus of the cantilever are not easy to be measured. Additionally, the cantilever is usually coated with aluminum or gold on the backside to increase the optical reflectivity. These coatings increase the complexity to determine the elastic properties of cantilever. Therefore it is desirable to measure the spring constants experimentally.

In the thesis, thermal noise methods [59] and drainage method [60] are both used to determine the stiffness of the cantilever.

Equipartition theorem method

Considering the contributions of all the modes to the deflection, we have [59, 53]

$$Z_{\mathrm{c}}(t) = \sum_{i=1}^{\infty} Z_{\mathrm{c}i}(t) = \sum_{i=1}^{\infty} \frac{2\alpha_i}{3}\frac{\sin\alpha_i \sinh\alpha_i}{\sin\alpha_i + \sinh\alpha_i} a(t)_i. \tag{1.17}$$

Each mode i is described by harmonic oscillator driven by a fluctuating noise force which is independent for each mode. In thermal equilibrium, each vibration mode has a mean thermal energy of $\frac{1}{2}k_{\mathrm{B}}T$. Thus the mean square amplitude at the end of the cantilever for the mode i $< a_i^2 >$ has to satisfy

$$< a_i^2 >= \frac{k_{\mathrm{B}}T}{k_i}, \tag{1.18}$$

where k_{B} is Boltzmann constant, T is the absolute temperature. k_i is the cantilever stiffness for mode i. From Eq. (1.17) and Eq. (1.15), we have

$$\begin{aligned} < Z_{\mathrm{c}}^2 > &= \sum_{i=1}^{\infty} \frac{4}{9\alpha_i^2}\left(\frac{\sin\alpha_i \sinh\alpha_i}{\sin\alpha_i + \sinh\alpha_i}\right)^2 < a_i^2 > \\ &= \frac{16k_{\mathrm{B}}T}{3k_c}\sum_{i=1}^{\infty}\frac{1}{\alpha_i^2}\left(\frac{\sin\alpha_i \sinh\alpha_i}{\sin\alpha_i + \sinh\alpha_i}\right)^2. \end{aligned} \tag{1.19}$$

With the values of α_i given in Tab. 1.1, we have

$$\sum_{i=1}^{\infty} \frac{1}{\alpha_i^2} \left(\frac{\sin \alpha_i \sinh \alpha_i}{\sin \alpha_i + \sinh \alpha_i} \right) = \frac{1}{4}. \tag{1.20}$$

Finally, we get [53]

$$k_{\mathrm{c}} < Z_{\mathrm{c}}^2 >= \frac{4}{3} k_{\mathrm{B}} T. \tag{1.21}$$

From the measurement of $< Z_{\mathrm{c}}^2 >$, one can deduce k_{c}. An example of the thermal noise for a cantilever (MLCT type B, Bruker) measured in pure water at the room temperature ($T = 297$ K) is shown in Fig 1.18 . The value of $< Z_{\mathrm{c}}^2 >$ is calculated as $0.22 \pm 0.03\ nm^2$, which gives the cantilever stiffness of $k_{\mathrm{c}} = 0.022 \pm 0.003$ N/m.

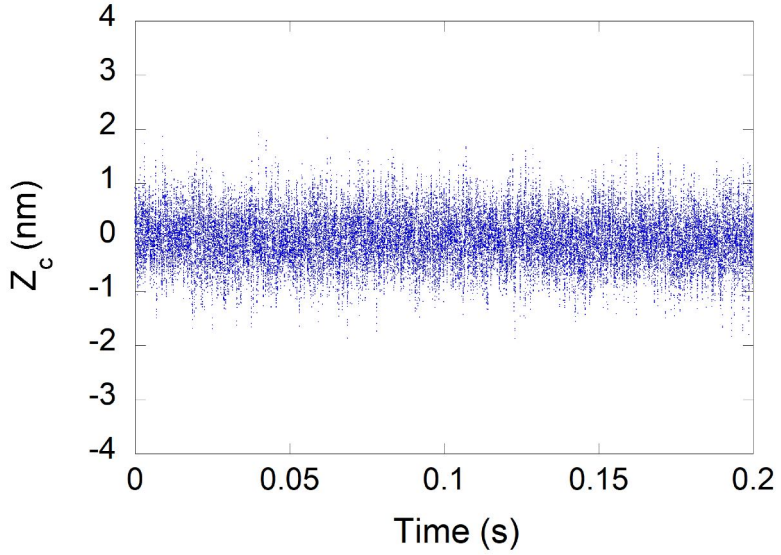

Figure 1.18: *The temporal thermal fluctuation of the cantilever (MLCT type B, Bruker) in pure water (sampling frequency:* 200 kHz*).*

Power spectral density method

The stiffness of cantilever can be obtained by fitting the power spectral density of the cantilever thermal fluctuation. The equation of the cantilever motion for mode i can be expressed as

$$m^* \ddot{a}_i + \gamma_{\mathrm{bulk}} \dot{a}_i + k_i a_i = F_{\mathrm{Thermal}i}, \tag{1.22}$$

where m^* is the effective mass of the cantilever, γ_{bulk} is the bulk damping and $F_{\mathrm{Thermal}i}$ is the thermal noise force. By Fourier transform, Eq. (1.22) becomes:

$$\left(-m^* \omega^2 + j\omega\gamma_{\mathrm{bulk}} + k_i\right) a_i(\omega) = F_{\mathrm{Thermal}i}(\omega). \tag{1.23}$$

Then, we have

$$|a_i(\omega)|^2 = \frac{|F_{\mathrm{Thermal}i}(\omega)|^2/m^*}{((\omega_i^2-\omega^2)^2+(\omega\omega_i/Q_i)^2)}, \tag{1.24}$$

where $Q_i = m^*\omega_i/\gamma_{\mathrm{bulk}}$ is the quality factor for mode i. Using the notation of $|F_{\mathrm{Thermal}i}(\omega)|^2 = \gamma_{\mathrm{bulk}}k_{\mathrm{B}}T$, we obtain

$$\mathrm{PSD}(a_i,\omega) = \frac{2k_{\mathrm{B}}T\omega_i/Q_i}{\pi m^*[(\omega_i^2-\omega^2)^2+(\omega_i\omega/Q_i)^2]}. \tag{1.25}$$

Since the cantilever deflection is deduced from the measurement of the cantilever inclination, using Eq. (1.16), The power spectral density for the deduced cantilever deflection $Z_{\mathrm{c}i}$ for mode i is given by

$$\mathrm{PSD}(Z_{\mathrm{c}i},\omega) = \frac{4\alpha_i^2}{9}\left(\frac{\sin\alpha_i\sinh\alpha_i}{\sin\alpha_i+\sinh\alpha_i}\right)^2 \frac{2k_{\mathrm{B}}T\omega_i/Q_i}{\pi m^*[(\omega_i^2-\omega^2)^2+(\omega_i\omega/Q_i)^2]}. \tag{1.26}$$

Finally, the measured power spectral density $\mathrm{PSD}(Z_{\mathrm{c}},\omega)$ is expressed as

$$\mathrm{PSD}(Z_{\mathrm{c}},\omega) = \sum_{i=1}^{\infty}\left(\frac{4\alpha_i^2}{9}\left(\frac{\sin\alpha_i\sinh\alpha_i}{\sin\alpha_i+\sinh\alpha_i}\right)^2 \frac{2k_{\mathrm{B}}T/Q_i}{\pi k_i\omega_i\left[\left(1-\left(\frac{\omega}{\omega_i}\right)^2\right)^2+\left(\frac{\omega}{\omega_i Q_i}\right)^2\right]}\right). \tag{1.27}$$

From the fitting of power spectral density of the cantilever thermal motion by Eq. (1.27), we can obtain the effective stiffness k_i, the resonance frequency ω_i and quality factor Q_i for each mode. In frequency domain, the power spectral density is expressed as

$$\begin{aligned}&\mathrm{PSD}(Z_{\mathrm{c}},f) = 2\pi\mathrm{PSD}(Z_{\mathrm{c}},\omega)\\ &= \sum_{i=1}^{\infty}\left(\frac{4\alpha_i^2}{9}\left(\frac{\sin\alpha_i\sinh\alpha_i}{\sin\alpha_i+\sinh\alpha_i}\right)^2 \frac{2k_{\mathrm{B}}T/Q_i}{\pi k_i f_i\left[\left(1-\left(\frac{f}{f_i}\right)^2\right)^2+\left(\frac{f}{f_i Q_i}\right)^2\right]}\right),\end{aligned} \tag{1.28}$$

with $\omega = 2\pi f$ and $\omega_i = 2\pi f_i$.

In Fig 1.19, we present the power spectral density for the cantilever motion calculated from the temporal signal of thermal fluctuation shown in Fig 1.18. The first three modes of the cantilever vibration are well defined. Figure 1.20 shows the fitting curve for the first mode in Fig 1.19 using Eq. (1.28). From the fitting, we get $k_1 = 0.019 \pm 0.005$ N/m, $f_1 = 3070$ Hz and $Q_1 = 1.46$. Similarly, by fitting the second mode, we obtain the values: $k_2 = 0.78 \pm 0.01$ N/m, $f_2 = 25490$ Hz and $Q_2 = 2.34$. Using Eq. (1.15), we conclude that the cantilever stiffness is calibrated as $k_{\mathrm{c}} = 0.02 \pm 0.005$ N/m.

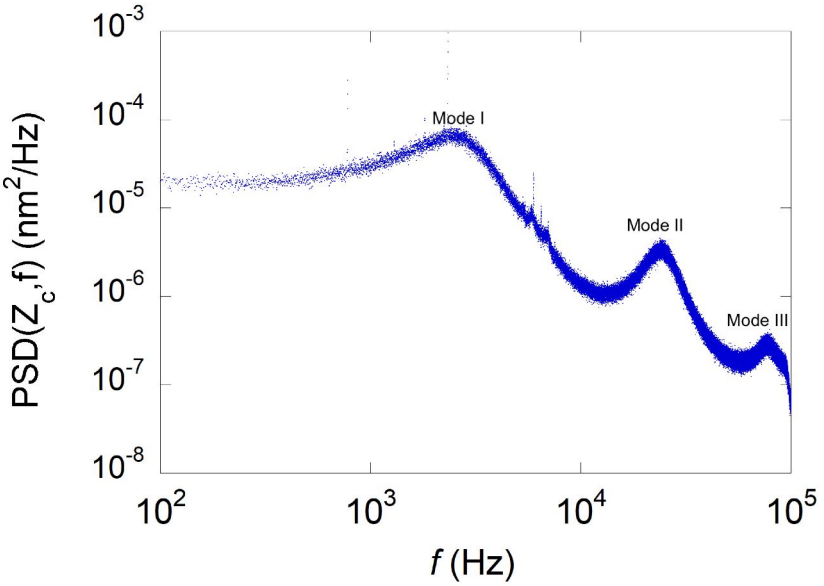

Figure 1.19: *The power spectral density measured for the cantilever (MLCT type B, Bruker) calculated from the thermal fluctuation shown in Fig 1.18.*

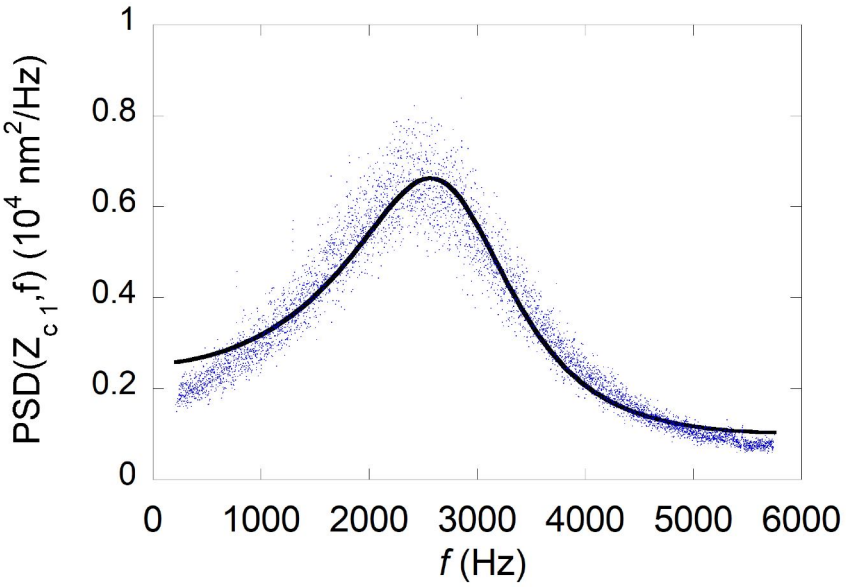

Figure 1.20: *The fitting curve for the first mode shown in Fig 1.19 by Eq. (1.28). The extracted stiffness* $k_1 = 0.019 \pm 0.005$ *N/m, resonance frequency* $f_1 = 3070$ *Hz and quality factor* $Q_1 = 1.46$ *for the first mode.*

1.3.3 The drainage method

When a spherical colloidal particle has been fixed on the end of the cantilever, the drainage method is applicable and simple. This method is suitable to all kinds of cantilevers but it requires the known radius of the sphere and the viscosity of the fluid [60]. This method employs the hydrodynamic drag force on a sphere approaching perpendicularly a flat surface immersed in a viscous liquid.

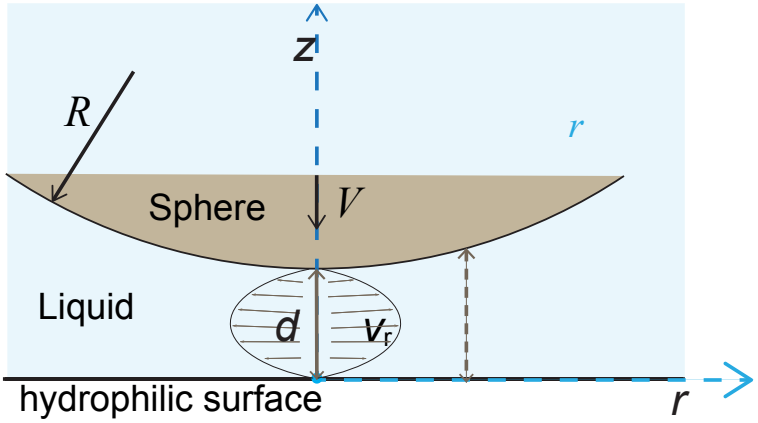

Figure 1.21: *Schematic of cantilever calibration by drainage force method. A spherical colloidal probe with a radius of R is approaching a hydrophilic surface with a velocity V in z direction in viscous liquid.*

As shown in Fig 1.21, a sphere with a radius of R is approaching a hydrophilic surface in a viscous liquid with a velocity of V. When the Reynolds number Re is small, and in the case of $d \ll \sqrt{2Rd}$, the confined fluid flow between the sphere and surface can be described by continuity equation and Navies-Stokes equation in the framework of the lubrication approximation:

$$\frac{\partial v_z}{\partial z} = -\frac{1}{r}\frac{\partial}{r}(rv_r), \tag{1.29a}$$

$$\frac{\partial p}{\partial r} = \eta\frac{\partial^2 v_r}{\partial z^2}, \tag{1.29b}$$

$$\frac{\partial p}{\partial z} = 0, \tag{1.29c}$$

where η is the dynamic viscosity of the fluid, v_r, v_z are the radical and vertical velocities of the fluid. Using parabolic approximation, the confined liquid thickness is given $h(r) = d + r^2/2R$ and d is the distance between the spherical particle and the flat surface. When the sphere and the wall are both hydrophilic, we have the boundary conditions of

- On the flat surface: $v_r(z = 0) = 0$, $v_z(z = 0) = 0$.
- On the sphere: $v_r(z = h) = 0$, $v_z(z = h) = -V$.

The solution of Eq. (1.29b) taking into account the boundary conditions leads to

$$v_r(z) = \frac{1}{2\eta}\frac{\partial p}{\partial r}\left(z^2 - hz\right). \tag{1.30}$$

By injecting Eq. (1.30) into the continuity equation of Eq. (1.29a), we get the expression for approaching velocity of the sphere as

$$V = -\int_0^h \frac{\partial v_z}{\partial z}\mathrm{d}z = \frac{1}{12\eta r}\frac{\partial}{\partial r}\left(rh^3\frac{\partial p}{\partial r}\right). \tag{1.31}$$

Then, the hydrodynamic force F_0 between the sphere and hydrophilic surface can be calculated by

$$F_0 = 2\pi\int_0^\infty rp(r)dr. \tag{1.32}$$

As a result, the drainage force reads [61],

$$F_0 = -\frac{6\pi\eta R^2}{d}V. \tag{1.33}$$

Here, we take a V-shaped cantilever (SNL-10, Bruker, USA) as an example. As shown in Fig. 1.8, a smooth spherical borosilicate sphere (MO-Sci Corporation) with a radius $R = 56.2 \pm 2\ \mu\mathrm{m}$ was glued to the end of the cantilever. The roughness of this sphere is $0.9\ \mathrm{nm}$ measured over a $1\ \mu\mathrm{m}^2$ surface area which was determined using the method shown in Sec. 1.2.2. The cantilever is placed on a liquid cell (see Fig. 1.3) which allows working in liquid environment. A freshly cleaved sheet of muscovite mica was used as a flat substrate. The bioscope II AFM (see Fig. 1.1) was used for force measurement. The measurement was carried on in $1\ \mathrm{M}$ NaCl solution in order to eliminate the effect of electrical double layer force. At room temperature ($21\ ^\circ\mathrm{C}$), the viscosity of $1\ \mathrm{M}$ NaCl solution is $\eta = 1\ \mathrm{mPa}\cdot\mathrm{s}$. The approaching velocity of the flat surface is controlled by a piezo (NanoT series, Mad City Labs). The data was captured by an analog to digital (A/D) acquisition board (PCI-4462, National Instrument, USA).The deflection versus piezo displacement was converted to deflection versus separation using the method given in Sec.1.1. The relative velocity for each separation is obtained from the time derivative of the separation distance [62].

The deflection Z_c and the relative velocity V versus distance for a typical measurement are shown in Fig. 1.22. As the surface approaches the particle, the cantilever starts to deflect away due to the hydrodynamic drag force. The relative velocity (time derivative of the distance) is the difference between the velocity of the piezo and the velocity at which the cantilever deflects away. At the small separation where the cantilever deflection is large, the relative velocity reduces.

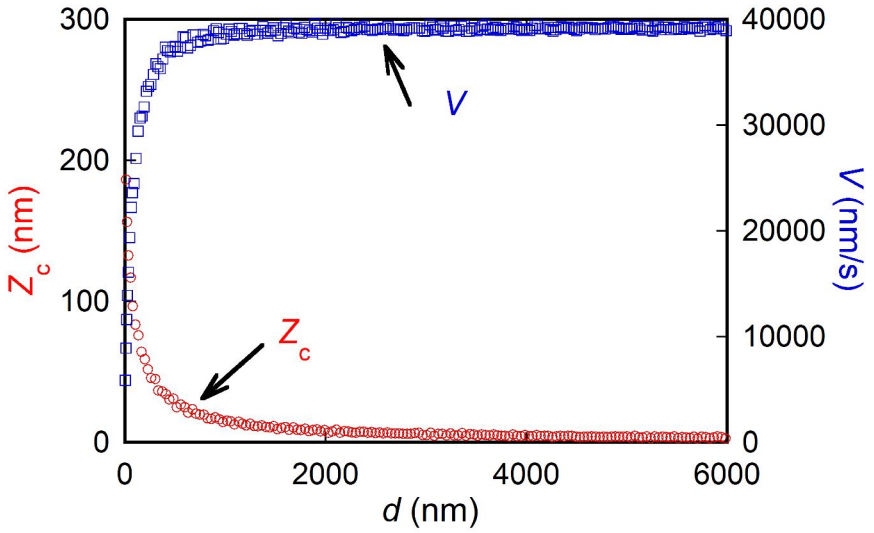

Figure 1.22: *The cantilever deflection (red circle) and relative velocity (blue square) versus the seperation distance. The relative velocity V is obtained from the time derivative of the separation distance.*

The measured force $F = k_c Z_c$ is equal to the drainage drag force acting on the particle:

$$k_c Z_c = \frac{6\pi\eta R^2}{d} V.$$

Then we have

$$\frac{V}{Z_c} = \frac{k_c}{6\pi\eta R^2} d. \tag{1.34}$$

Taking into account the values of the particle radius and the liquid viscosity, from the linear fitting (Eq. (1.34)) of the data of V/Z_c versus d shown in Fig. 1.23, we obtain the value of the cantilever stiffness $k_c = 0.16 \pm 0.01$ N/m.

However, at smaller separation distance the validity of Eq. (1.33) which is formulated using the no-slip boundary condition may be affected due to the contribution of partial boundary slip [63]. Additionally, roughness of the surfaces may also affect the accuracy at small separation distance. In order to avoid these effects at small distance, we just use the data from where the distance is large enough (> 200 nm) to extract the cantilever stiffness.

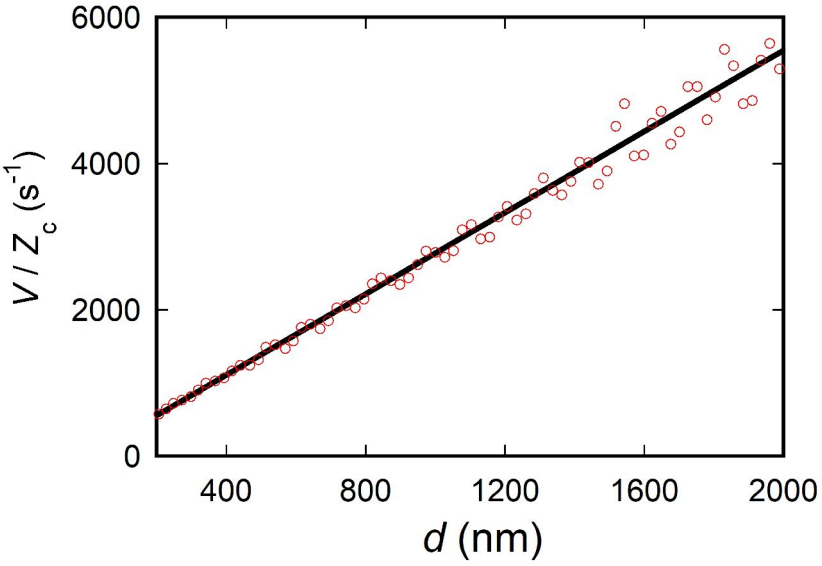

Figure 1.23: *The velocity divided by deflection versus distance. The solid line is the linear fitting by Eq.* (1.34)*, which gives us the cantilever stiffness* $k_c = 0.16 \pm 0.01$ N/m.

1.4 Conclusion

In this chapter, we introduced the AFM for topographic imaging and surface force measurement. The techniques: the attachment of the colloidal probe, the roughness characterization of the surface, the calibration of the piezo and the surface tension measurement were presented. Successively, we introduced thermal noise methods and the drainage method for the calibration of the cantilever.

Chapter 2

Visco-Elastic Effects at Air-Water Interface: Contamination Effect

Contents

2.1 Context 29
2.2 Theoretical Model 30
2.2.1 Numerical Calculations 33
2.2.2 Limiting Cases $\omega \ll \omega_0$ and $\omega \gg \omega_0$: Asymptotic Calculation 34
2.2.3 Analytical Calculations using analogy with the disc bubble interaction 35
2.3 Experiment 37
2.3.1 Dynamic AFM method with colloidal probe 37
2.3.2 Results & Discussion 43
2.4 Conclusion 48

2.1 Context

Recently, much progress has been achieved in the study of fluid flow in the vicinity of interfaces [64, 65]. Colloidal probe atomic force microscopy is one of the techniques used to characterize fluid flows on the nano-scale [65], such as to study capillary phenomena such as the interaction between bubbles [66, 67] or droplets [68, 69, 70], the hydrodynamic boundary condition at a water-air interface [13], and dynamical wetting [71, 72, 73, 74, 75, 76]. Assuming that the shear stress continues at liquid-gas interfaces, the much lower viscosity of the gas theoretically makes them behave as shear free interfaces. As a result, liquid-gas interfaces are thought to be good candidates for perfect slipping interfaces [8, 9, 10, 11]. However, Manor et al. [12, 13, 14] have experimentally shown that the slip length at liquid-gas interfaces is moderate (a

few of tens of nanometers) but not infinite as expected. This finite slip length value is due to the presence of the impurities at the liquid-gas interfaces. The air-water interface is generally prone to be contaminated by the surface impurities such as surfactant, particles or other surface active agents. The presence of such impurities can modify flow near such interfaces in a drastic manner.

In this chapter, the visco-elastic effect of air-water interfaces due to the surfactant contamination is studied by dynamic AFM method. From the measurement of the amplitude and phase of the sphere, we extract the viscous and elastic forces acting on the sphere. In the framework of the lubrication approximation, we developed a model that takes into account the advection of the impurities at the air-water interface to explain the measurements. In this study, we focus only on large distance between the sphere and the bubble where capillary deformation of the bubble surface due to the hydrodynamic pressure is very small (probe-bubble distance $d > 6\pi\eta R^2\omega/\sigma$ [77], where σ is the surface tension of water, η is the water viscosity, R is the radius of the sphere and ω is the oscillation frequency of sphere.).

2.2 Theoretical Model

We assume that the liquid-gas interface of the bubble may contain a very small quantity of insoluble surfactants. The presence of the surfactants with a local concentration c decreases the interfacial surface tension from a value σ to a value $\sigma - \Pi$. At low concentration, the surfactant behaves as dilute gas without interaction, and the surface pressure Π is related to the concentration by: $\Pi = ck_{\mathrm{B}}T$. The sketch of the study is shown in Fig. 2.1. The air-water interface is prepared by injecting an air bubble on PS surface in pure water. The sphere vibrates with frequency ω. We use cylindrical coordinate to describe the flow.

During the fluid flowing at the interface, some surfactant molecules (impurities) are driven by advection and diffusion. The concentration of surfactant is described by the advection-diffusion equation [12, 13, 14]:

$$\frac{\partial c}{\partial t} + \nabla \cdot (v_{\mathrm{s}} c) = D\Delta c, \tag{2.1}$$

where D is the diffusion coefficient, and the advection term arises from the radial velocity at the surface of the bubble, $v_{\mathrm{s}} = v_r(z = 0)$.

The confined fluid flow between the sphere and bubble is described by continuity and Navies-Stokes equations. Using the lubrication approximation, they can be expressed by Eqs. 1.29.

On the surface of the sphere, the radial and vertical velocities of the fluid satisfy the boundary conditions: $v_r(z = h) = 0$, $v_z(z = h) = V$, where V is the vertical velocity of the sphere glued at the end of the cantilever and h is the confined fluid thickness between the sphere and

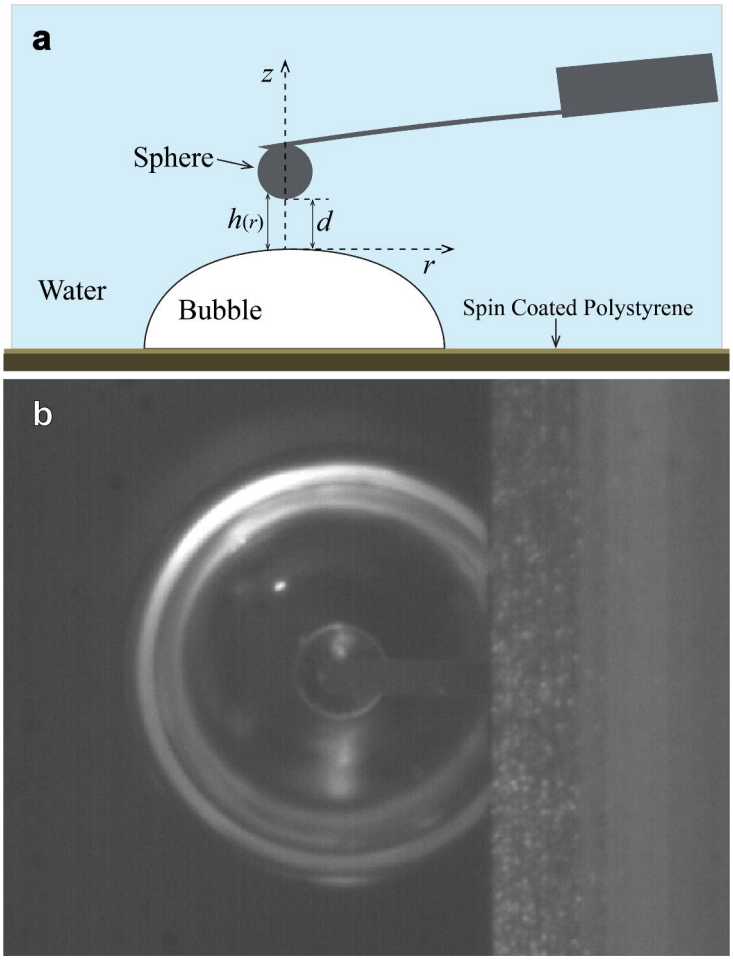

Figure 2.1: ***a)*** *Sketch of the hydrodynamic interaction measurement between a colloidal sphere and air-water interface. The interface is prepared by deposing a spherical bubble on polystyrene surface. A glass sphere glued at the end of the AFM cantilever vibrates at the distance* d*.* ***b)*** *The optical image of the experimental setup (top view).*

bubble, which is given by: $h(r) = d + r^2/2R_{\text{eff}}$, $R_{\text{eff}} = 1/(R_{\text{b}}^{-1} + R^{-1})$ is the effective radius and R_{b}, R are the radii of the bubble and sphere, respectively. d is the gap distance. On the bubble surface, shear stress is equal to the tangential stress induced by the Marangoni effect: $\eta\frac{\partial v_r(z=0)}{\partial z} = \frac{\partial \Pi}{\partial r}$. The vertical velocity should be equal to zero: $v_z(z=0) = 0$ (we neglect the bubble deformation). Integrating Eq. (1.29b) with respect to z and using these above boundary conditions for the radial velocity on the sphere and bubble surface, we get:

$$v_r(z) = \frac{1}{\eta}\left[\frac{1}{2}(z^2 - h^2)\frac{\partial p}{\partial r} + (z-h)\frac{\partial \Pi}{\partial r}\right], \tag{2.2}$$

Inserting Eq. (2.2) into the continuity equation of Eq. (1.29a) and integrating with respect to z,

we get:

$$v_z(z) - v_z(z=0) = \int_0^z \frac{\partial v_z(z)}{\partial z} dz = -\frac{1}{\eta r}\frac{\partial}{\partial r}\left[r\left((\frac{z^3}{6} - \frac{h^2 z}{2})\frac{\partial p}{\partial r} + (\frac{z^2}{2} - hz)\frac{\partial \Pi}{\partial r}\right)\right]. \quad (2.3)$$

Using the boundary conditions for the vertical velocity on the sphere and bubble surface, Eq. (2.3) can be rewritten as:

$$V = \frac{dZ}{dt} = j\omega Z = \frac{1}{3\eta r}\frac{\partial}{\partial r}(rh^3\frac{\partial p}{\partial r}) + \frac{1}{2\eta r}\frac{\partial}{\partial r}(rh^2\frac{\partial \Pi}{\partial r}), \quad (2.4)$$

where $Z = Z_0 e^{j\omega t}$ is the instantaneous position of the sphere. Eq. (2.4) can be integrated with respect to radial coordinate r and rearranged to get the expression for the pressure p in the form of:

$$\frac{\partial p}{\partial r} = \frac{3\eta V r}{2h^3} - \frac{3}{2h}\frac{\partial \Pi}{\partial r}, \quad (2.5)$$

Injecting Eq. (2.5) into Eq. (2.2), we get the value of the radial velocity of the fluid on bubble surface,

$$v_s = v_r(z=0) = -\frac{3Vr}{4h} - \frac{h}{4\eta}\frac{\partial \Pi}{\partial r}. \quad (2.6)$$

Equation (2.6) shows that the advection of the surfactants acts as a feedback on the velocity on the bubble surface.

In our study, the diffusion term in Eq. (2.1) is irrelevant. Indeed, with $R_{\text{eff}} \sim 50\ \mu m$, $d = 1 \sim 10\ \mu\text{m}$ and $D \sim 10^{-10}\ \text{m}^2/\text{s}$, one finds that the diffusion time $\tau = L^2/D$ over the lubrication length $L = \sqrt{2R_{\text{eff}}d}$ exceeds the period of the cantilever vibration. For weakly soluble impurities, the characteristic relaxation time which results from diffusion in the aqueous phase over the distance L turns into $\tau_b = L^2/D_b$ with the bulk diffusion coefficient D_b that is $D_b < D$. For the range of the oscillation frequencies used in the experiment, both $\omega\tau$ and $\omega\tau_b$ are significantly smaller than unity. Thus surfactants diffusion along the interface, or in the thin fluid film, is slow compared to the advection, and may be discarded in the Eq. (2.1).

Writing $\nabla \cdot (v_s c) = v_s \cdot \nabla c + c\nabla \cdot v_s$, and neglecting small terms proportional to the concentration gradient ∇c or to the concentration modulation with respect to the equilibrium value c_0, Eq. (2.1) is simplified to:

$$\frac{\partial c}{\partial t} - \frac{c_0 k_B T}{4\eta}\frac{\partial}{r\partial r}(rh\frac{\partial c)}{\partial r} = c_0\frac{3Vd}{2h^2}. \quad (2.7)$$

where the second term on the left hand side arises from $\nabla\Pi = k_B T\nabla c$ and the right hand side term arises from the divergence of the unperturbed surface velocity. By solving Eq. (2.7), we get the value of the surfactant pressure $\Pi = ck_B T$ which can be injected in to Eq. (2.5) and we obtain the hydrodynamic pressure $p(r)$. According to Eq. (1.29c), p is constant in z direction, and the hydrodynamic force acting on the sphere is calculated from the expression of $p(r)$ by

$$F_h = 2\pi\int_0^\infty rp(r)dr. \quad (2.8)$$

From the ansatz $\frac{\partial c}{\partial t} = j\omega c$, and using dimensionless variable $\overline{r} = \frac{r}{\sqrt{2R_{\text{eff}}d}}$, we transform Eq. (2.7) to

$$\frac{1}{\overline{r}}\frac{\partial}{\overline{r}}\left[\overline{r}(1+\overline{r}^2)\frac{\partial c}{\partial \overline{r}}\right] - j\frac{\omega}{\omega_0}c = \frac{12\eta RV}{k_{\text{B}}Td}\frac{1}{(1+\overline{r}^2)^2} \tag{2.9}$$

where

$$\omega_0 = \frac{c_0 k_{\text{B}} T}{8\eta R_{\text{eff}}} \tag{2.10}$$

is a characteristic frequency that depends on surfactant pressure $\Pi_0 = c_0 k_{\text{B}} T$, the viscosity of the liquid η and the effective bubble radius R_{eff}.

Equation (2.9) is solved numerically (Sec. 2.2.2) using finite-element method to get the value of the surface pressure $\Pi = ck_{\text{B}}T$ and then the hydrodynamic drag force F_{h} applied on the sphere. For only two limiting case $\omega \ll \omega_0$ and $\omega \gg \omega_0$, the expression of the hydrodynamic drag force can be calculated analytically (Sec.2.2.2). In Sec. 2.2.3, we use an analogy between the sphere-bubble interaction and the disc-bubble interaction to derive an approximated analytical expression for the hydrodynamic drag force for any given frequency of oscillation.

2.2.1 Numerical Calculations

Using the finite element method, we solve Eq. (2.9) numerically to get the value of surfactant concentration $c(r)$ on bubble surface and the gradient of the surface pressure $\nabla\Pi(r) = k_{\text{B}}T\nabla c(r)$. Injecting these values into Eq. (2.5) and integrating Eq. (2.8) over the sphere surface, we get the hydrodynamic force F_{h}. Our numerical results suggest that the general behavior of the hydrodynamic force is the in form of

$$F_{\text{h}} = g(\frac{\omega}{\omega_0})F_0, \tag{2.11}$$

where $F_0 = -\frac{6\pi\eta R_{\text{eff}}^2}{d}V$ is the non slip hydrodynamic force [61] and $g(\frac{\omega}{\omega_0})$ is a complex number, which is distance independent, and depend only on the ratio between the working frequency ω and the characteristic frequency ω_0 that depends on the surfactant concentrations.

The hydrodynamic force can be written as: $F_{\text{h}} = F_{\text{vis}} + jF_{\text{el}}$ with F_{vis} and F_{el} are the viscous and elastic hydrodynamic components respectively which are related to the function $g(\frac{\omega}{\omega_0})$ by

$$\left|\frac{F_{\text{vis}}}{F_0}\right| = \left|\text{Re}\left(g\left(\frac{\omega}{\omega_0}\right)\right)\right| \tag{2.12a}$$

$$\left|\frac{F_{\text{el}}}{F_0}\right| = \left|\text{Im}\left(g\left(\frac{\omega}{\omega_0}\right)\right)\right| \tag{2.12b}$$

In Fig. 2.2, the numerical calculation results for the viscous and elastic components divided by the non-slip hydrodynamic force are presented. These numerical calculation results can be

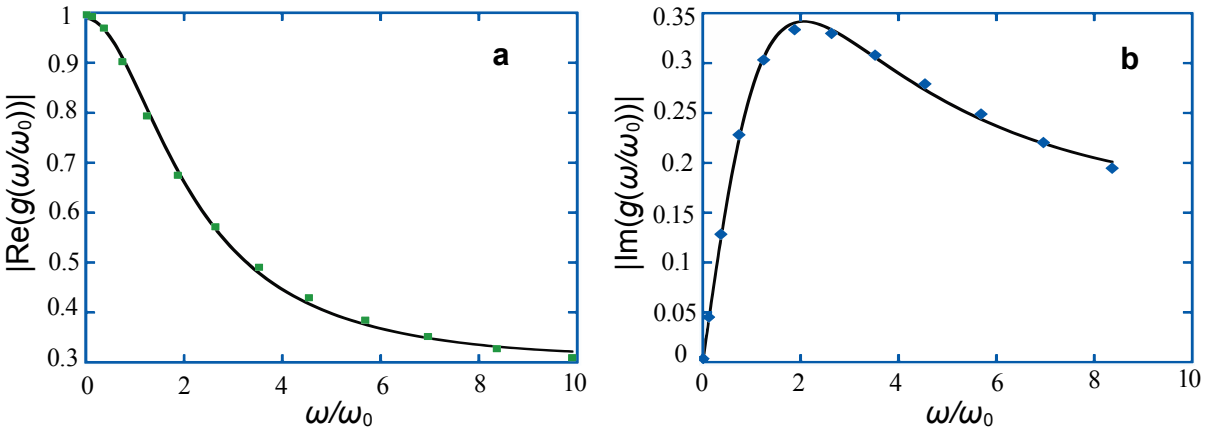

Figure 2.2: *Numerical results of the viscous component F_{vis} and elastic component F_{el} of the hydrodynamic force divided by the viscous non-slip hydrodynamic drag force F_0. And the continuous line in **a)** and **b)** are the fitting curves by the real and the imaginary terms of Eq. (2.13), respectively.*

approximated by an equation in the form of

$$g(\frac{\omega}{\omega_0}) = \frac{1}{4} + \frac{\frac{3}{4}}{a_1 + a_2(\frac{\omega}{\omega_0})^2 + a_3(\frac{\omega}{\omega_0})^3} - j\frac{\frac{3}{4}\frac{\omega}{\omega_0}}{a_4 + a_5(\frac{\omega}{\omega_0})^2 + a_6(\frac{\omega}{\omega_0})^3}. \tag{2.13}$$

From the fitting, we get the value of the constants, $a_1 = 1.01$, $a_2 = 1.01$, $a_3 = -0.01$, $a_4 = 1.08$, $a_5 = 0.29$ and $a_6 = -0.01$.

2.2.2 Limiting Cases $\omega \ll \omega_0$ and $\omega \gg \omega_0$: Asymptotic Calculation

In the quasi-static limit of small working frequency or for high impurity concentrations, $\omega \ll \omega_0$, we treat $\frac{\omega}{\omega_0}c$ in Eq. (2.9) as a perturbation, Solving the differential equation to linear order of the parameter of $\frac{\omega}{\omega_0}$ by iteration, and then integrating Eq. (2.5) and Eq. (2.8), we get

$$F_{\text{vis}} = F_0, F_{\text{el}} = F_0\frac{3\omega}{8\omega_0}, (\omega \ll \omega_0), \tag{2.14}$$

with non-slip hydrodynamic force $F_0 = -\frac{6\pi\eta R_{\text{eff}}^2 V}{d}$. The viscous term of the hydrodynamic drag force corresponds to that on solid surface with non-slip boundary conditions, which is four times larger than on a free surface [61]. This is arises from the surfactant-induced surface stress $\nabla\Pi = k_{\text{B}}T\nabla c$ and its back reaction on the surface flow.

On the contrary, at high working frequency or for sufficiently low impurity concentration, $\omega \gg \omega_0$, the first term on the left-hand side in Eq. (2.9) can be treated as a perturbation. Evaluating to second order and integrating Eq. (2.5) and Eq. (2.8), we obtain

$$F_{\text{vis}} = F_0(\frac{1}{4} + 8\frac{\omega_0^2}{\omega^2}), F_{\text{el}} = F_0\frac{2\omega_0}{\omega}, (\omega \gg \omega_0). \tag{2.15}$$

In this limiting case, the surface stress $\nabla\Pi = k_{\mathrm{B}}T\nabla c$ is of less importance, and for $\omega/\omega_0 \to \infty$, we recover the hydrodynamic drag force for full slip boundary condition, $F_{\mathrm{vis}}/F_0 = 1/4$. Meanwhile, the elastic component F_{el}/F_0 varies linearly with ω_0/ω.

2.2.3 Analytical Calculations using analogy with the disc bubble interaction

The hydrodynamic squeezing force between a disc and flat substrate is equivalent to the squeezing force between a sphere and flat substrate, provided that the disc radius R_{disc} is replaced by the hydrodynamic radius $\sqrt{2Rd}$, where R is the sphere radius and d is the distance between the sphere and the substrate:

$$F_{\mathrm{D}} = -\frac{3\pi}{2}\eta\frac{R_{\mathrm{disc}}^4}{d^3}V \overset{R_{\mathrm{disc}}=\sqrt{2Rd}}{\longleftrightarrow} F_{\mathrm{S}} = -6\pi\eta\frac{R^2}{d}V, \tag{2.16}$$

where F_{D} is the drag force between disc and flat substrate, F_{s} is the drag force between sphere and substrate. To get the expression of the drag force between the sphere and the bubble in the presence of the surfactants, we will take advantage of this analogy. We calculate first the drag force for disc geometry and then replace in the obtained expression the disc radius R_{disc} by the hydrodynamic radius $\sqrt{2R_{\mathrm{eff}}d}$[1].

Eq. (2.5) and Eq. (2.7) that describe the hydrodynamic pressure and the surfactant concentration for the sphere-bubble interaction are still valid for the disc-bubble interaction provided the gap h is taken constant and independent of the radial coordinate, $h(r) = d$. Eq. (2.5) reads

$$\frac{\partial p}{\partial r} = \frac{3\eta V r}{2d^3} - \frac{3}{2d}\frac{\partial\Pi}{\partial r}, \tag{2.17}$$

and Eq. (2.7) reads

$$\frac{\partial c}{\partial t} - \frac{c_0 k_{\mathrm{B}}T d}{4\eta}\frac{\partial}{r\partial r}(r\frac{\partial c)}{\partial r} = c_0\frac{3V}{2d}, \tag{2.18}$$

here, V is denoted as the velocity of the disc instead of the sphere.

Solving Eq. (2.18) and imposing the condition for the surfactant concentration $c(r \geq R_{\mathrm{disc}}) = 0$, we get

$$c(r) = -\frac{3jc_0V}{\omega}\left[1 - \frac{I_0(\sqrt{j}k\frac{r}{R_{\mathrm{disc}}})}{I_0,(\sqrt{j}k)}\right] \tag{2.19}$$

and

$$\Pi(r) = k_{\mathrm{B}}Tc(r) = -\frac{3jk_{\mathrm{B}}Tc_0V}{\omega}\left[1 - \frac{I_0(\sqrt{j}k\frac{r}{R_{\mathrm{disc}}})}{I_0(\sqrt{j}k)}\right], \tag{2.20}$$

[1]We have used the effective radius R_{eff} instead of the sphere radius R in the expression of hydrodynamic radius because we investigate the drag force on spherical bubble surface.

where $k^2 = \frac{4\omega\eta R_{\rm disc}^3}{c_0 k_{\rm B} T d}$, I_0 and I_1 are the modified Bessel function of the first kind with index 0 and 1, respectively. Injecting Eq. (2.20) into Eq. (2.17) and integrating the pressure over the surface of the disc, we get the the hydrodynamic force:

$$F_{\rm hD} = -\frac{3\pi}{2}\eta\frac{R_{\rm disc}}{d^3}V\left\{\frac{1}{4} + \frac{12j}{k^2}\left[\frac{1}{\sqrt{j}k}\frac{I_1(\sqrt{j}k)}{I_0(\sqrt{j}k} - \frac{1}{2}\right]\right\}. \tag{2.21}$$

Using the analogy described above and replace $R_{\rm disc}$ by $\sqrt{2R_{\rm eff}d}$, we get $k^2 = \frac{2\omega\eta R_{\rm disc}^2}{c_0 k_{\rm B} T d} \to \frac{\omega}{\omega_0}$, with $\omega_0 = \frac{c_0 k_{\rm B} T}{8\eta R_{\rm eff}}$ as defined before, and the hydrodynamic force acting on the sphere is equal to

$$F_{\rm hS} = -6\pi\eta\frac{R^2}{d}V\left\{\frac{1}{4} + \frac{12j}{(\frac{\omega}{\omega_0})}\left[\frac{1}{\sqrt{j\frac{\omega}{\omega_0}}}\frac{I_1(\sqrt{j\frac{\omega}{\omega_0}})}{I_0(\sqrt{j\frac{\omega}{\omega_0}})} - \frac{1}{2}\right]\right\}. \tag{2.22}$$

Fig. 2.3a presents the analytically calculated hydrodynamic coefficient $\frac{F_{\rm vis}}{F_0}$ and $\frac{F_{\rm el}}{F_0}$ using the analogy described above. We have also reported the numerical calculation of Sec. 2.2.1. The curves obtained from the analogy have the same profile of the curves obtained from numerical calculation, but they do not coincide each other. In order to superimpose the curves, we have to modify the value of ω_0 in Eq. (2.22) and make it equal to $\omega_0' = 2.72\omega_0$ as shown in Fig. 2.3b.

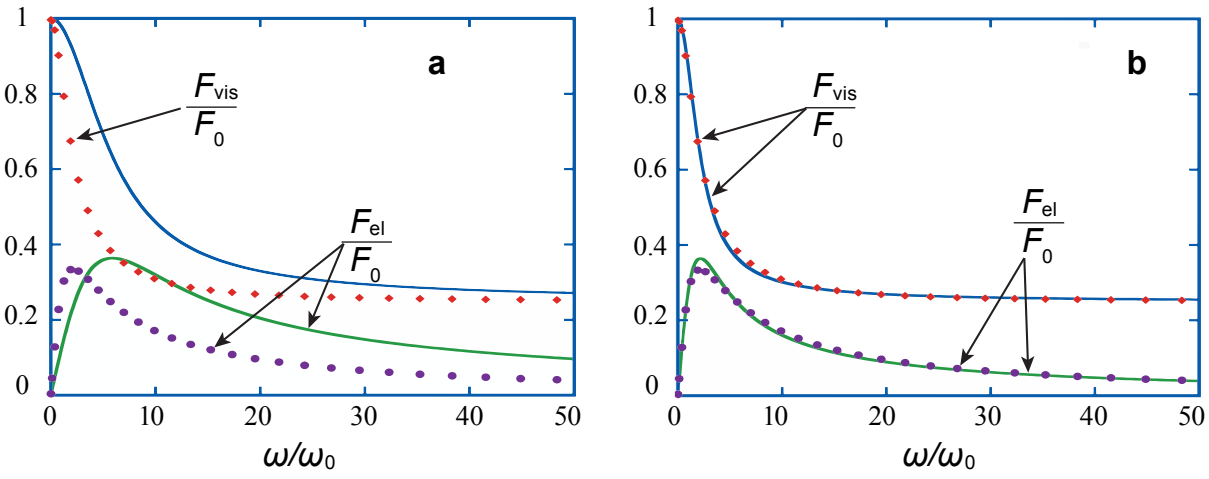

Figure 2.3: ***a)*** *Hydrodynamic force $F_{\rm vis}/F_0$ and $F_{\rm el}/F_0$ calculated analytically using the analogy described in this section (solid lines). We also report on the same figure the numerical calculation of Sec. 2.2.1(dots).* ***b)*** *In order to superimpose the curves, the value ω_0 in Eq. (2.22) was modified to $\omega_0' = 2.72\omega_0$.*

2.3 Experiment

2.3.1 Dynamic AFM method with colloidal probe

In this study, the dynamic AFM method with colloidal probe was addressed to probe the viscoelastic responses of the bubble surface. Figure 2.4 shows the sketch for dynamic atomic force microscope measurement. Basically, a piezoelectric actuator is used to excite the vibration of the cantilever with driving amplitude A_d and driving frequency ω. The gap between the sphere and substrate is controlled by displacing the sample using a piezo stage. The amplitude A and phase φ of the cantilever oscillation versus the piezo displacement are recored. Meanwhile, the DC deflection is also recorded and used to determine the separation distance following the method shown in Sec. 1.1.

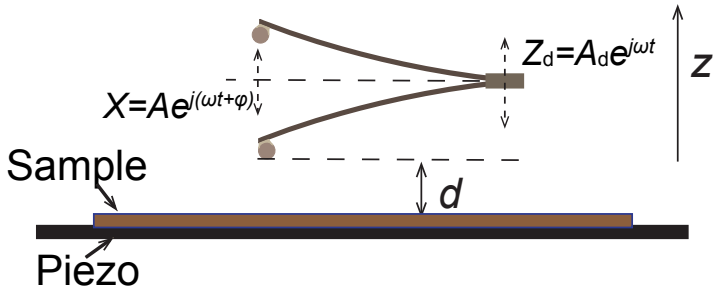

Figure 2.4: *Sketch of the dynamic AFM method. A cantilever is excited by external acoustic excitation with oscillation of* $Z_\mathrm{d} = A_\mathrm{d}e^{j\omega t}$*. A piezo stage is used to control the distance between the probe and the sample surface.*

The instantaneous displacement of the cantilever base can be described by $Z_\mathrm{d} = A_\mathrm{d}e^{j\omega t}$, j is the imaginary unit. The instantaneous deflection of the cantilever is described as $X = Ae^{j(\omega t+\varphi)}$. Therefore, the total oscillation of the cantilever is given by

$$Z = X + Z_\mathrm{d} = Ae^{j(\omega t+\varphi)} + A_\mathrm{d}e^{j\omega t}. \tag{2.23}$$

The motion of the cantilever can be simplified to a point mass model given by

$$m^*\ddot{Z} + \gamma_\mathrm{bulk}\dot{Z} + k_\mathrm{c}X = F_\mathrm{h}, \tag{2.24}$$

where F_h is the interaction force between the colloidal probe and the interface.

For a probe oscillating with a small amplitude compared to the size of probe and the range of the interaction length, the instantaneous interaction force can be linearised and has two contribution: conservation term ($-k_\mathrm{int}Z$) and dissipative term ($-\gamma_\mathrm{int}\dot{Z}$), namely $F_\mathrm{h} = -k_\mathrm{int}Z - \gamma_\mathrm{int}\dot{Z}$, where k_int and γ_int are the interaction stiffness and damping coefficient, respectively. Then, Eq. 2.24 can be rewritten as:

$$m^*\ddot{X} + \gamma_\mathrm{bulk}\dot{X} + k_\mathrm{c}X = F_\mathrm{d} - k_\mathrm{int}Z - \gamma_\mathrm{int}\dot{Z}, \tag{2.25}$$

F_d is driving force induced by the displacement of the cantilever base and can be calculated using Euler-Bernouli beam theory. The analytical expression for F_d is

$$F_\mathrm{d} = (m^*\omega^2 - j\omega\gamma_\mathrm{bulk})\beta_\mathrm{d}A_\mathrm{d}e^{j\omega t}, \tag{2.26}$$

with a coefficient $\beta_\mathrm{d} \approx 1.565$ [78].

However, in a real experiment, the cantilever is excited by two source: the base vibration and an additional force from the surrounding fluid, which is driven by the piezo actuator [78, 79]. Accurate determination of the acoustic wave propagation is difficult because it depends on the cantilever geometry and fixation of the cantilever on the liquid cell. Here the driving force is measured experimentally. Far from the interface, the interaction force can be neglected, assuming a general expression for the driving force in the form

$$F_\mathrm{d} = (F_1 + jF_2)e^{j\omega t}, \tag{2.27}$$

where F_1 is the term that is in phase with base vibration and F_2 is the term that is in phase quadrature. By inserting Eq. (2.23) and Eq. (2.27) into Eq. (2.25), and using $F_\mathrm{h} = 0$, we get the expression for the driving force:

$$F_1 = k_\mathrm{c} \cdot A_\infty \left[\left(1 - \left(\frac{\omega}{\omega_\mathrm{c}}\right)^2\right)\cos(\varphi_\infty) - \left(\frac{\omega}{\omega_\mathrm{c}Q_0}\right)\sin(\varphi_\infty)\right], \tag{2.28a}$$

$$F_2 = k_\mathrm{c} \cdot A_\infty \left[\left(1 - \left(\frac{\omega}{\omega_\mathrm{c}}\right)^2\right)\sin(\varphi_\infty) + \left(\frac{\omega}{\omega_\mathrm{c}Q_0}\right)\cos(\varphi_\infty)\right]. \tag{2.28b}$$

A_∞ and φ_∞ are the amplitude and phase of the cantilever measured far from the interface, ω_c is the angular resonance frequency ($\omega_\mathrm{c} = \sqrt{k_\mathrm{c}/m^*}$), Q_0 is the bulk quality factor of the probe ($Q_0 = m^*\omega_\mathrm{c}/\gamma_\mathrm{bulk}$). Injecting the expression of driving force into Eq. (2.25), we get

$$m^*\ddot{X} + (\gamma_\mathrm{bulk} + \gamma_\mathrm{int})\dot{X} + (k_\mathrm{c} + k_\mathrm{int})X = (F_1 + jF_2)e^{j\omega t} - (k_\mathrm{int} + j\omega\gamma_\mathrm{int})A_\mathrm{d}e^{j\omega t}.$$

With the notation of $X = Ae^{j(\omega t+\varphi)}$, we get

$$\begin{aligned} k_\mathrm{int} + j\omega\gamma_\mathrm{int} &= \frac{F_1 + jF_2 + (m^*\omega^2 - j\omega\gamma_\mathrm{bulk} - k_\mathrm{c})Ae^{j\varphi}}{Ae^{j\varphi} + A_\mathrm{d}} \\ &= \frac{F_1 + jF_2 + \left[\left(\frac{\omega}{\omega_\mathrm{c}}\right)^2 - j\frac{\omega}{\omega_\mathrm{c}Q_0} - 1\right]k_\mathrm{c}Ae^{j\varphi}}{Ae^{j\varphi} + A_\mathrm{d}}. \end{aligned} \tag{2.29}$$

By separating the real and the imaginary part of Eq. (2.29), we get the desired expressions for

the damping and stiffness of the probe-sample interaction in the forms of

$$\frac{\omega\gamma_{\rm int}}{k_{\rm c}} = \frac{\frac{A}{A_{\rm d}}\frac{F_1}{k_{\rm c}A_{\rm d}}\sin\varphi + \frac{F_2}{k_{\rm c}A_{\rm d}}\left(1+\frac{A}{A_{\rm d}}\cos\varphi\right) - \frac{A}{A_{\rm d}}\sin\varphi\left(1-\frac{\omega^2}{\omega_{\rm c}^2}\right) - \frac{A}{A_{\rm d}}\frac{\omega}{\omega_{\rm c}Q_0}\left(\frac{A}{A_{\rm d}}+\cos\varphi\right)}{1+\left(\frac{A}{A_{\rm d}}\right)^2+2\frac{A}{A_{\rm d}}\cos\varphi}, \tag{2.30a}$$

$$\frac{k_{\rm int}}{k_{\rm c}} = -1+\frac{\omega^2}{\omega_{\rm c}^2} + \frac{\frac{A}{A_{\rm d}}\frac{F_1}{k_{\rm c}A_{\rm d}}\cos\varphi + \frac{A}{A_{\rm d}}\frac{F_2}{k_{\rm c}A_{\rm d}}\sin\varphi + \left(1+\frac{A}{A_{\rm d}}\cos\varphi\right)\left(1-\frac{\omega^2}{\omega_{\rm c}^2}\right) + \frac{F_1}{k_{\rm c}A_{\rm d}} + \frac{A}{A_{\rm d}}\frac{\omega}{\omega_{\rm c}Q_0}\sin\varphi}{1+\left(\frac{A}{A_{\rm d}}\right)^2+2\frac{A}{A_{\rm d}}\cos\varphi}. \tag{2.30b}$$

The experimental setup is shown in Fig. 2.5. The signal access module (Nanoscope III, Bruker) has the advantage to control the input and the output signals of the AFM (driving excitation of the cantilever, vertical and lateral deflections of cantilever, etc). The lock-in amplifier (The Signal Recovery 7280 Lock-in Amplifier) output signal excites the cantilever vibration. The DC component of deflection is recorded, and the AC component is used as input to the lock in amplifier to measure the amplitude and phase of the cantilever oscillation.

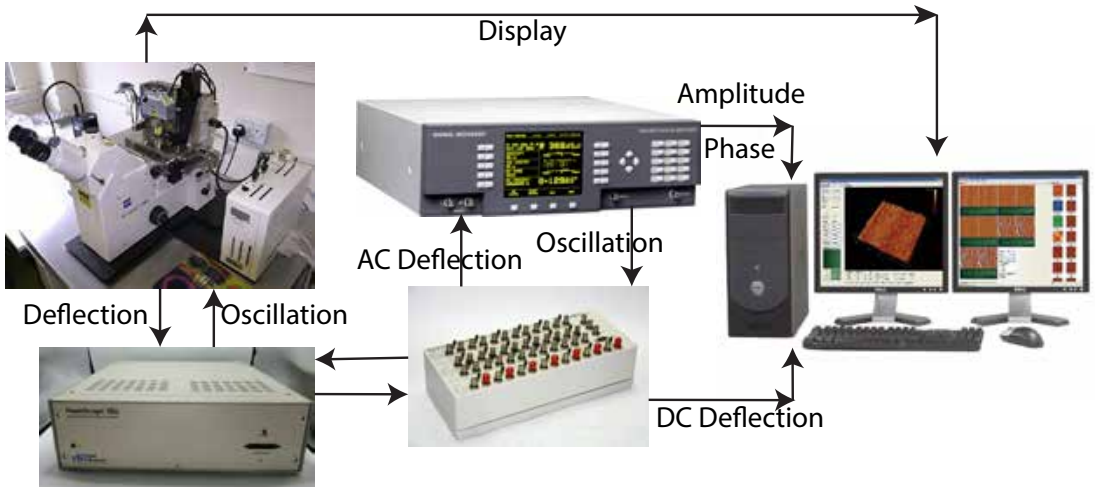

Figure 2.5: *The experimental setup for dynamic AFM method.*

We used a spherical borosilicate particle(MO-Sci Corporation) with a radius of $R = 53.1 \pm 1\ \mu$m to make the colloidal probe. The sphere was glued at the end of a silicon nitride rectangular cantilever (ORC8, Bruker) by epoxy (Araldite, Bostik, Coubert). The colloidal probe was fixed on the liquid cell (DTFML-DD-HE). The assembly of the probe and liquid cell were then rinsed several times with ultra-pure water (MilliQ-Millipore). The samples were fixed on

a multi-axis piezo system(NanoT series, Mad City Labs) that allows a large displacement (up to 50 μm) with a high accuracy under close loop control. Using the drainage method shown in Sec.1.3.3, the stiffness of the cantilever with an attached sphere, $k_c = 0.25 \pm 0.005$ N/m, was determined from the drainage data at large distance ($200 - 10000$ nm). The bubbles' radii R_b were measured with an optical microscope. The cantilever quality factor and resonance frequency are respectively $Q_0 = 3.9$, $\omega_c/2\pi = 1340$ Hz, which were obtained from the fitting of the spectrum of thermal noise by Eq. (1.28) for the first mode of the cantilever vibration. We took mica surface as the reference sample to check the validity of the this method. The experiments were perform in ultra-pure water at room temperature ($21°C$).

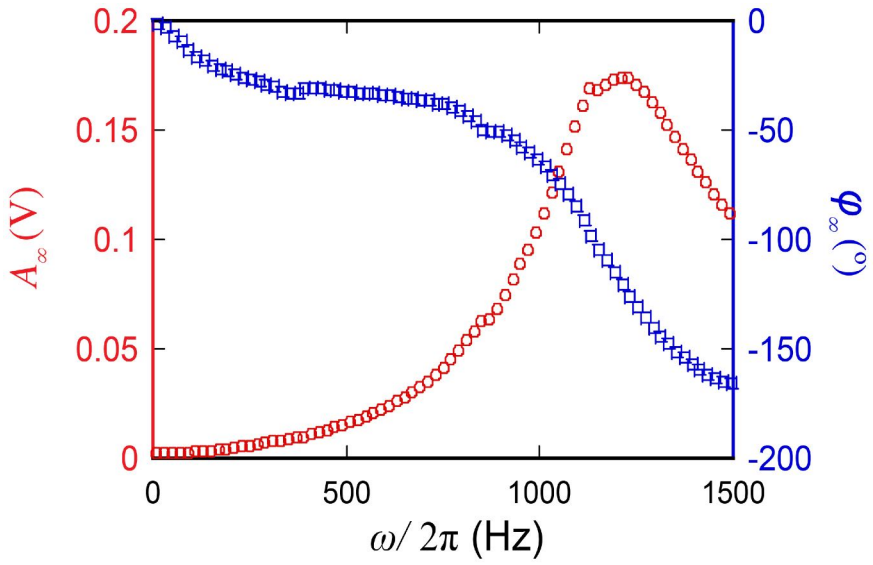

Figure 2.6: *The amplitude (red circle) and phase (blue square) measured far from mica surface in pure water.*

Figure 2.6 shows the amplitude A_∞ and phase φ_∞ far from the surface versus the driving frequency. Figure 2.7 shows the driving forces F_1, F_2 versus the frequencies calculated from the data shown in Fig. 2.6 by Eqs. (2.28a) and (2.28b).

Figure 2.8 shows the measured DC component of deflection, amplitude and phase versus the piezo displacement on mica surface (the driving frequency is $\omega/2\pi = 200$ Hz). Close to the contact position ($d = 0$), the damping is infinity, and thus the measured cantilever deflection amplitude is equal to the driving vibration amplitude (*i.e.* $A = A_d$ when $d = 0$) and the phase is equal to $-180°$ at contact position. In this measurement, we obtain the driving amplitude $A_d = 32$ mV. Note here, the value of the driving amplitude measured on mica surface will also be used to calculate the hydrodynamic drag force on bubble surface.

Figure 2.9 shows the calculated damping and stiffness of the probe-sample interaction versus distance using the data shown in Fig. 2.8. The damping increases when the distance decreases and the stiffness is equal to zero as expected (no elastic interaction).

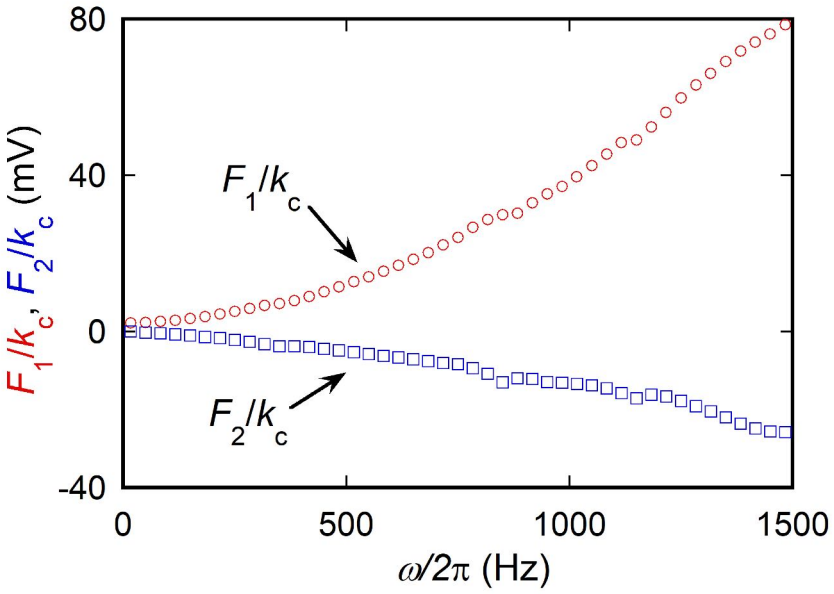

Figure 2.7: *The real F_1 and imaginary F_2 components of the driving force calculated from the amplitude and phase in Fig. 2.6 using Eqs. (2.28).*

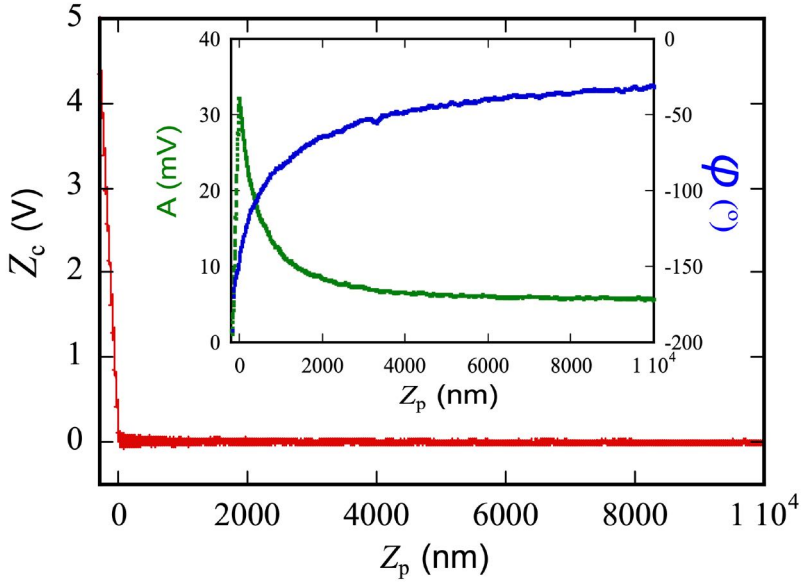

Figure 2.8: *The DC component of cantilever deflection Z_c as a function of the piezo displacement Z_p at 200 Hz. The insect shows the coresponding amplitude A and phase φ measured from the AC component of the cantilever deflection versus piezo displacement Z_p.*

In order to check the validity of this method, we compare the measured interaction force with hydrodynamic drag force that acts on a sphere moving perpendicular to a flat substrate such as

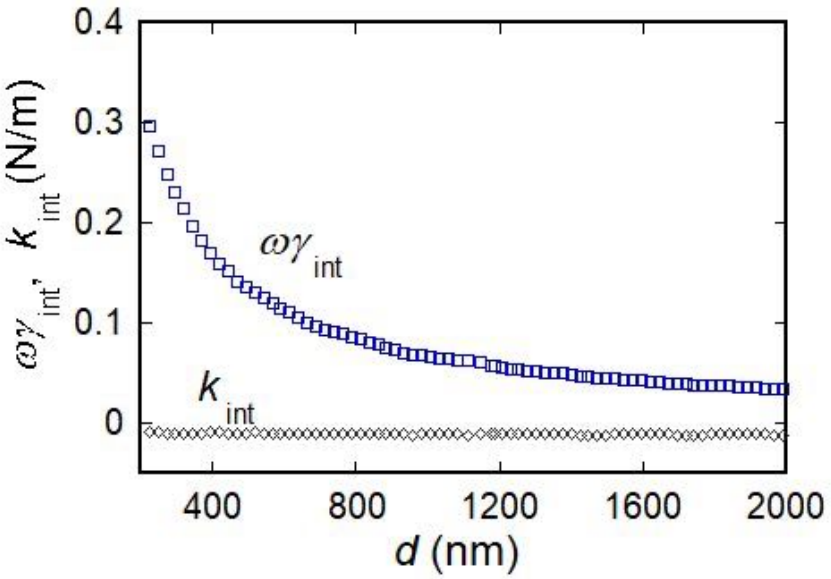

Figure 2.9: *The calculated damping $\omega\gamma_{int}$ and stiffness k_{int} of probe-sample interaction at* 200 Hz *on mica surface.*

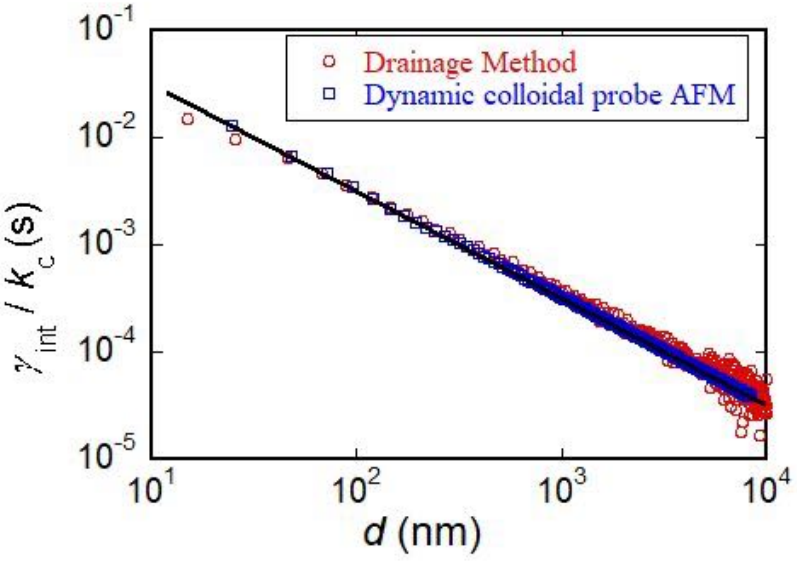

Figure 2.10: *The damping measured in both drainage method and dynamic colloidal probe AFM method and the black line the theoretical calculation with γ_0/k_c.*

the drainage force in Sec. 1.3.3. In the drainage method, the hydrodynamic drag coefficient $\gamma_{\rm int}$ that we measure: $\gamma_{\rm int}/k_{\rm c} = Z_{\rm c}/V$ should be equal to the interaction damping $\gamma_{\rm int}/k_{\rm c}$ in Eq. 2.30a. As shown in Fig. 2.10, the damping coefficients measured by both drainage method and

dynamic AFM method collapse to $\gamma_0 = \frac{6\pi\eta R^2}{d}$ calculated with non-slip boundary condition, as expected.

2.3.2 Results & Discussion

In order to make it convenient to compare, we introduce a complex hydrodynamic drag coefficient $\Gamma_{\rm h}(\omega) = \Gamma_{\rm vis} - j\Gamma_{\rm el}$ to describe the hydrodynamic drag force. The hydrodynamic drag coefficient is defined by $\Gamma_{\rm h} = -F_{\rm h}/V$, which is related to the damping $\gamma_{\rm int}$ and stiffness $k_{\rm int}$ coefficients by $\Gamma_{\rm vis} = \gamma_{\rm int}$, $\Gamma_{\rm el} = k_{\rm int}/\omega$.

Figure 2.11 presents the viscous $\Gamma_{\rm el}$ and the elastic $\Gamma_{\rm vis}$ coefficients of the hydrodynamic drag force versus distance for the sphere vibrating at frquency of 200 Hz close to a mica surface. As expected, the hydrodynamic interaction with the mica surface is purely viscous, and the elastic coefficient $\Gamma_{\rm el}$ is zero for all the distances.

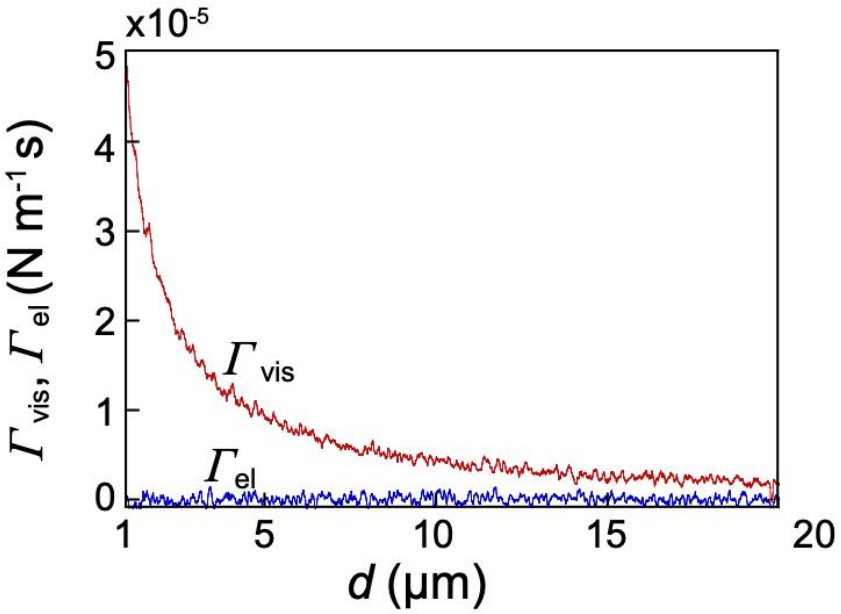

Figure 2.11: *Viscous* $\Gamma_{\rm vis}$ *and elastic* $\Gamma_{\rm el}$ *components for the sphere vibrating at frequency* 200Hz *in pure water on mica surface.*

Figure 2.12 shows the viscous coefficient $\Gamma_{\rm vis}$ of the hydrodynamic force versus the distance d for different vibrating frequencies. Note that, the viscous part of the hydrodynamic drag coefficients extracted for different vibration frequencies coincide with each other, and with the theoretical hydrodynamic drag coefficient given by $6\pi\eta R^2/d$ for non slip boundary conditions.

Figure 2.13 shows the viscous $\Gamma_{\rm vis}$ and elastic $\Gamma_{\rm el}$ drag coefficients measured on the bubble at the vibration frequency of 100 Hz. Unlike the measurement on the mica surface, the results

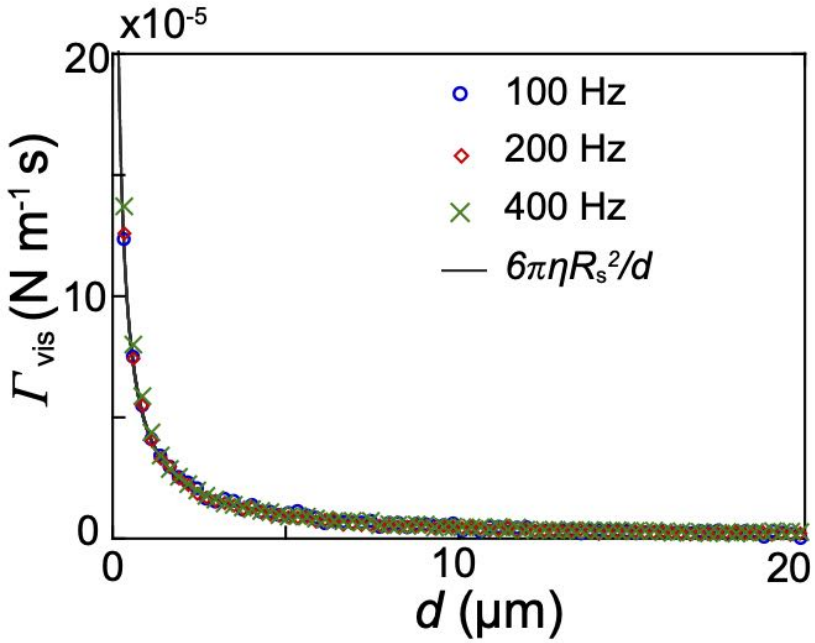

Figure 2.12: *The hydrodynamic drag coefficient versus the distance for different vibration frequencies in pure wanter with mica surface. The solid dark line is the theoretical drag coefficient* $\Gamma_0 = 6\pi\eta R^2/d$ *for no slip boundary condition on mica surface.*

show that the interaction is not purely viscous, and the elastic coefficient $\Gamma_{\rm el}$ is not zero any more.

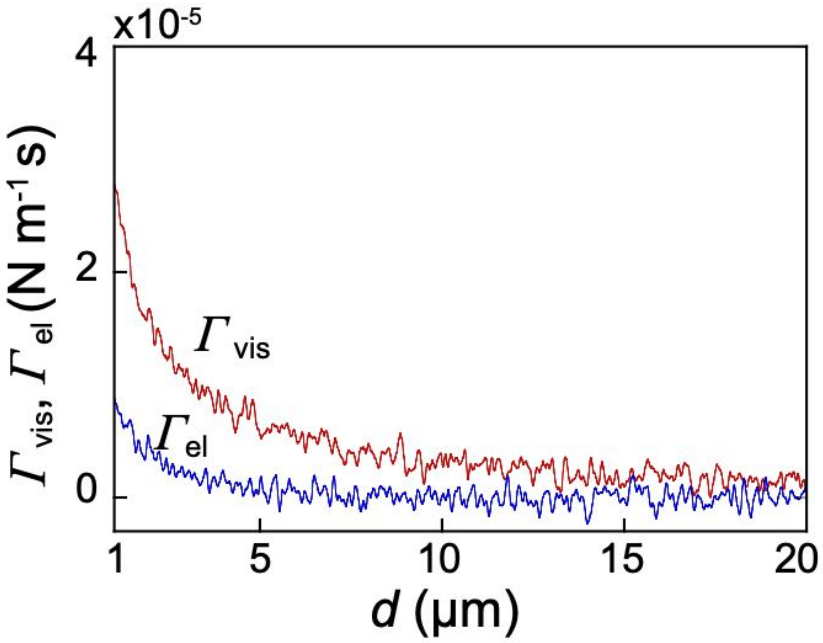

Figure 2.13: *Viscous* $\Gamma_{\rm vis}$ *and elastic* $\Gamma_{\rm el}$ *components of the hydrodynamic drag force measured on bubble surface in pure water. The cantilever sphere vibrates at a frequency of* 100 Hz.

Furthermore, as shown in Fig. 2.14, the viscous coefficient for different frequencies of the vibration do not coincide with each other as for mica surface. The drag coefficients corresponding to full slip $3\pi\eta R_{\rm eff}^2/2d$ and no slip $6\pi\eta R_{\rm eff}^2/d$ boundary condition on the bubble are also presented in Fig. 2.14. While for low frequencies, the viscous drag force is close to the no slip case, with increasing frequency, the drag force decreases and finally approaches the full slip boundary condition on the bubble surface. In our experiments, the frequency could not be increased further since vibrations in bubble shape are excited at higher frequencies. For example, for a bubble with radius of $R_{\rm b} = 400\ \mu$m, the first resonance occurs around 600 Hz.

We have performed two independent experiments under similar conditions, at a temporal distance of one month. In Fig. 2.15, we present the measured viscous drag force $F_{\rm vis}$ and elastic drag force $F_{\rm el}$ divided by the reference force F_0, and we compare with numerical calculations (solid line). The only adjustable parameter is the impurity concentration c_0 that defines the surface pressure $\Pi_0 = c_0 k_{\rm B} T$. The fitted values are $\Pi_0 = (0.25 \pm 0.05)$ mN/m for the first experiment (see Fig. 2.15a) and $\Pi_0 = (0.35 \pm 0.05)$ mN/m for the second one (see Fig. 2.15b), corresponding to $c_0 = (63 \pm 13) \times 10^{15}$ m^{-2} and $c_0 = (87 \pm 13) \times 10^{15}$ m^{-2}, or to an area per molecule of 16 nm^{2}and 12 nm^2, thus justifying the ideal-gas picture adopted for the surface pressure. The impurities may originate from the polystyrene substrate, from the surrounding air (our experiments were performed at ambient conditions), or from other unknown sources, despite the care taken in cleaning up all the equipment carefully and despite our use of ultra-pure water for the experiments.

In order to confirm the role of impurities, we have done a control experiment in a 60 μM

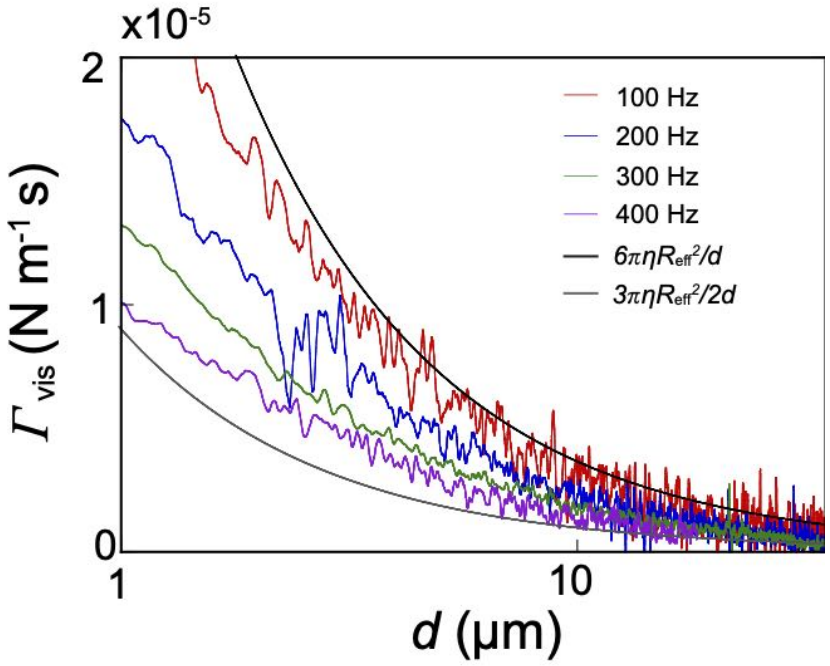

Figure 2.14: *The viscous component* $\Gamma_{\rm vis}$ *of the hydrodynamic drag force for different oscillation frequencies measured on bubble surface. The calculated viscous component of drag coefficient corresponding to full slip and non slip boundary conditions on the bubble surface which are represented by the grey and dark line, respectively.*

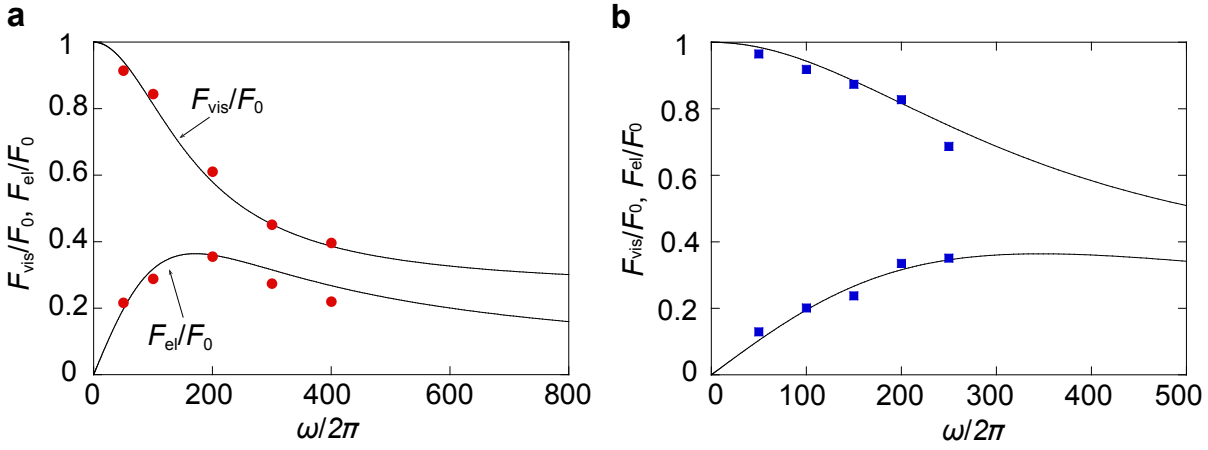

Figure 2.15: ***a****) The experimental results of hydrodynamic force* $F_{\rm vis}/F_0$ *and* $F_{\rm el}/F_0$ *as a function of vibrating frequency with ultra-pure water.* ***b****) The results for the second experiment performed one month later under similar conditions. The solid lines represent the numerical calculation in 2.2.1 with a fitting parameter of* Π_0*. The fitted values of* Π_0 *are* (0.25 ± 0.05) mN/m *and* (0.35 ± 0.05) mN/m *for experimental results in* ***a*** *and* ***b****, respectively.*

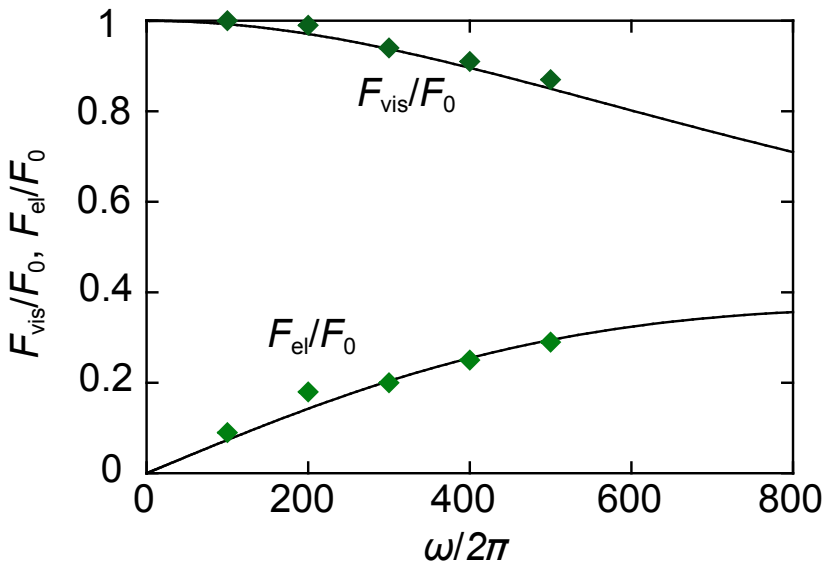

Figure 2.16: *The experimental results of hydrodynamic force* $F_{\rm vis}/F_0$ *and* $F_{\rm el}/F_0$ *as a function of vibrating frequency with* $60\ \mu$M *SDS solution. The solid lines represent the numerical calculation in 2.2.1 with a fitting parameter of* Π_0*, whose value is* $\Pi_0 = (1.0 \pm 0.1)\ {\rm mN/m}$.

SDS solution. The visco-elastic forces are shown in Fig. 2.16, and fitted with a surface pressure $\Pi_0 = (1.0 \pm 0.1)\ {\rm mN/m}$. The surface tension measurement using a Wilhelmy plate method, gives a surface tension reduction of $\Delta\sigma = (1.2 \pm 0.1)\ {\rm mN/m}$, which is close to the fitted value of Π_0. We conclude that this control experiment provides a quantitative confirmation of the above analysis.

In Fig. 2.17, we present the measured drag forces as a function of the reduced frequency ω/ω_0. The data from the two independent experiment in ultra-pure water and the control experiment in $60\ \mu$M SDS solution, collapse on a single master curve. The dashed lines are from the numerical calculations in Sec. 2.2.1 and the continuous lines are the analytical results given in Eq. (2.14) and Eq. (2.15). The viscous drag force shows a smooth crossover from the non slip value at zero frequency to the full slip value at large frequency, as expected for a free surface. The elastic component increases linearly, passes through a maximum at $\omega \approx 2\omega_0$. The analytical calculations describe the asymptotic behavior rather well.

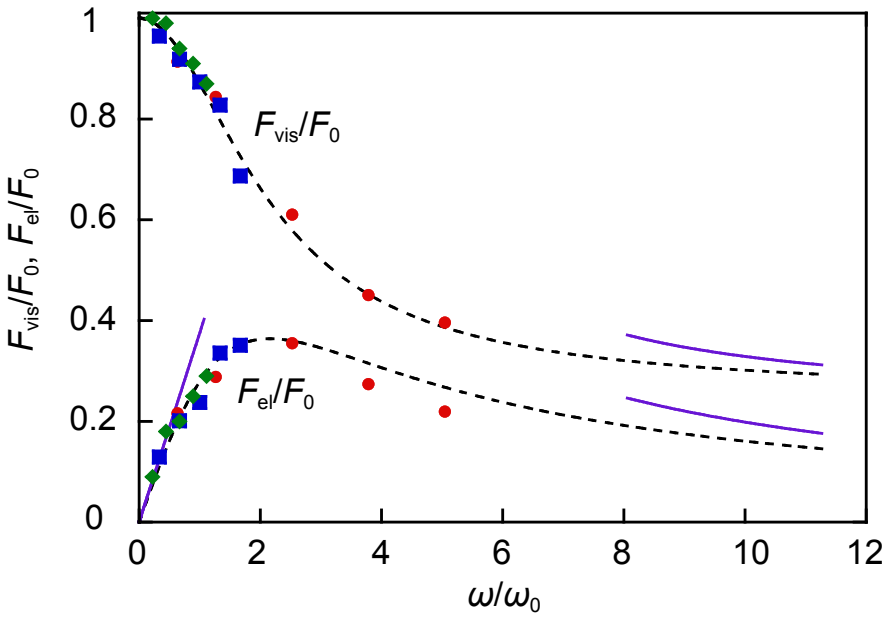

Figure 2.17: *The master curve of viscous force $F_{\rm vis}/F_0$ and elastic force $F_{\rm el}/F_0$ for these three experimental measurements. The dashed lines are from the numerical calculations in Sec. 2.2.1 and the continuous lines are the analytical results given in Eq. (2.14) and Eq. (2.15).*

2.4 Conclusion

In this chapter, we have studied the viscoelastic effect due to the presence of the surfactant contamination. The measurements demonstrate that very low concentrations of surface impurities drastically modify boundary conditions for flows near the interfaces. Both viscous and elastic forces are exerted by the air-water interface on the vibrating sphere. Our measurements give clear evidence for a strong elastic drag force besides the viscous drag force. When varying the frequency from low frequency to high frequency, a crossover from no-slip to full slip boundary conditions occurs in the viscous drag force. Besides the reduction of the viscous force, the elastic drag force shows a nontrivial variation as the vibration frequency changes. The value of the elastic force is comparable to the viscous force in the intermediate range. Furthermore, our experiment methods allow to detect the impurity concentration at an air-water interface through its viscoelastic response to a vibrating AFM probe.

Chapter 3

Visco-Elastic Effects at Air-Water Interface: Capillary Effect

Contents

3.1 Context **49**

3.2 Analytical Model for Visco-Capillary Effect: Simplified Model **50**

3.3 Experimental Results **52**

3.3.1 Visco-capillary effect studied by thermal noise excitation of the AFM probe 52

3.3.2 Visco-capillary effect studied by acoustic excitation of the AFM probe 56

3.4 Numerical Model for Visco-Capillary Effect **59**

3.5 Conclusion **62**

3.1 Context

While the structure and physicochemistry of the confining surfaces are important when considering the flow of confined liquids, their elastic behavior is usually not taken into account [20]. At small gap, the hydrodynamic pressure between the confining surfaces can be very large, that it may induce elastic deformation of the surfaces. Based on this elastohydrodynamic coupling, new tools were developed to probe the mechanical properties of soft interfaces without contact. Using dynamic SFA, Charlaix's team has measured the mechanical properties of several surfaces ranging from soft surface like PDMS to hard surface like glass [20, 21, 22]. Guan et al. have used vibrating nano-needle glued to the AFM cantilever to probe the viscoelastic properties of PDMS surfaces [23] and living cells [24].

Indeed, a sphere vibrating vertically close to bubble is a good candidate to investigate the elastohydrodynamic interaction. At small distance the hydrodynamic pressure induced by the

sphere vibration is so large that the bubble surface will be deformed which leads to elastohydrodynamic coupling.

In this chapter, we investigate the visco-capillary interaction by colloidal probe which is driven by two methods: thermal excitation and external acoustic excitation. As we have presented in chapter 2, the bubble surface may contain contamination which induce viscoelastic responses due to the advection of the surfactant by the liquid flow. In order to measure accurately the visco-capillary response, the contribution due to advection of impurities should be eliminated. For the thermal excitation experiment, a cantilever with a large resonance frequency ω_c is chosen (such that $\omega_c \gg \omega_0$, where ω_0 is defined in Eq. (2.10)) in order to satisfy the full slip boundary condition on the bubble surface. For the external acoustic excitation experiment, the cantilever was driven at low frequencies and SDS solutions was introduced in order to satisfy no-slip boundary condition at the air-water interface.

3.2 Analytical Model for Visco-Capillary Effect: Simplified Model

At small distance, the bubble deformation can not be neglected, the capillary effect will contribute to the interaction between sphere and bubble. The deformation $\xi(r)$ of bubble is related to the hydrodynamic pressure $p(r)$ by Young-Laplace equation:

$$p(r) = \sigma \Delta \xi(r) = \frac{\sigma}{r} \frac{\partial}{\partial r} \left(r \frac{\partial \xi(r)}{\partial r} \right), \tag{3.1}$$

where Δ is the Laplace operator and σ is the surface tension of bubble.

As reported in previous chapter, for large vibration frequency, a full slip boundary condition should be satisfied on the bubble surface (*i.e.* $(\partial v_r/\partial z)|_{z=0} = 0$. Therefore, the pressure in Eq. (2.5) becomes to:

$$p(r) = -\frac{3j\omega Z \eta R_{\text{eff}}}{4h^2} \tag{3.2}$$

and thus the hydrodynamic interaction force

$$F_{\text{h}} = 2\pi \int_0^\infty r p(r) \mathrm{d}r = -\frac{3\pi j\omega Z \eta R_{\text{eff}}^2}{2d}. \tag{3.3}$$

By substituting Eq. (3.2) into Eq. (3.1) and integrating Eq. (3.1), we obtain

$$\frac{\mathrm{d}\xi}{\mathrm{d}r} = -\frac{3j\omega Z \eta r R_{\text{eff}}}{8\sigma d h}. \tag{3.4}$$

Assuming $\xi(r = R_\mathrm{b}) = 0$, and integrating Eq. (3.4), we get the expression of the bubble deformation,

$$\xi_0 = \xi(r=0) = -\int_0^{R_\mathrm{b}} \frac{\mathrm{d}\xi(r)}{\mathrm{d}r} dr = \frac{3j\omega Z\eta R_\mathrm{eff}^2}{8\sigma d} \ln\left(1 + \frac{R_\mathrm{b}^2}{2R_\mathrm{eff} d}\right) \approx \frac{3j\omega Z\eta R_\mathrm{eff}^2}{8\sigma d} \ln\left(\frac{R_\mathrm{b}^2}{2R_\mathrm{eff} d}\right). \tag{3.5}$$

The bubble stiffness k_b can be defined as $F_\mathrm{h} = k_\mathrm{b}\xi_0$, and then from Eq. (3.3) and Eq. (3.5), we obtain:

$$k_\mathrm{b} = \frac{F_\mathrm{h}}{\xi_0} = \frac{4\pi\sigma}{\ln\left(\frac{R_\mathrm{b}^2}{2R_\mathrm{eff} d}\right)}. \tag{3.6}$$

Note here that in the derivation of the bubble stiffness we have assumed a flat bubble. This assumption is thought to be valid because in our case the radius of the bubble is much larger than the radius of the colloidal sphere.

Furthermore, by comparing Eq. (3.3) to the viscous hydrodynamic force defined by $F_\mathrm{h} = -\gamma_\mathrm{h}\dot{Z} = -j\omega\gamma_\mathrm{h} Z$, we obtain the expression of the hydrodynamic damping for a full slip surface:

$$\omega\gamma_\mathrm{h} = \frac{3\pi\omega\eta R_\mathrm{eff}^2}{2d}. \tag{3.7}$$

The viscoelastic responses of bubbles can be modeled using the Maxwell model: spring and dashpot (damping) in series(see Fig. 3.1). In this simplified model, the mechanical impedance

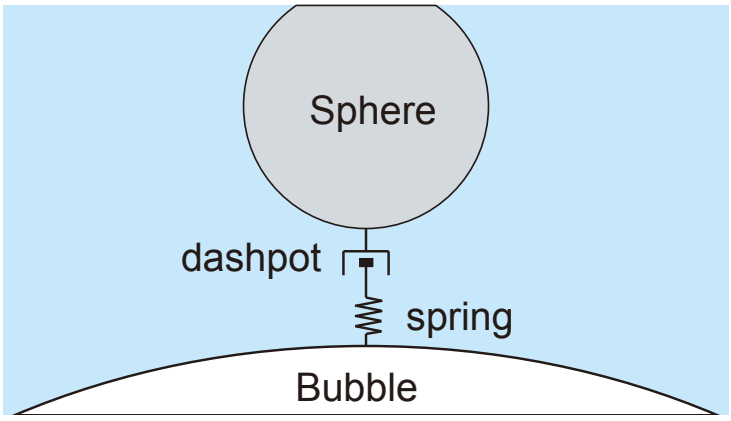

Figure 3.1: *Equivalent model of the viscoelastic response of the microsized bubble: spring and dashpot in series.*

are expressed as:

$$G' + jG'' = \frac{1}{\frac{1}{k_\mathrm{b}} + \frac{1}{j\omega\gamma_\mathrm{h}}} = \frac{k_\mathrm{b}(\omega\gamma_\mathrm{h})^2}{k_\mathrm{b}^2 + (\omega\gamma_\mathrm{h})^2} + j\frac{k_\mathrm{b}^2\omega\gamma_\mathrm{h}}{k_\mathrm{b}^2 + (\omega\gamma_\mathrm{h})^2}. \tag{3.8}$$

By substituting Eq. (3.6) and Eq. (3.7) into Eq. (3.8), the impendance of the elastic component G' and the dissipative component G'' of the interaction can be given as

$$G' = \frac{3\pi\eta\omega R_{\text{eff}}^2}{2d} \frac{\frac{3\eta\omega R_{\text{eff}}^2}{8\sigma d} \ln\left(\frac{R_{\text{b}}^2}{2R_{\text{eff}}d}\right)}{1+\left[\frac{3\eta\omega R_{\text{eff}}^2}{8\sigma d} \ln\left(\frac{R_{\text{b}}^2}{2R_{\text{eff}}d}\right)\right]^2}, \tag{3.9a}$$

$$G'' = \frac{3\pi\eta\omega R_{\text{eff}}^2}{2d} \frac{1}{1+\left[\frac{3\pi\eta\omega R_{\text{eff}}^2}{8\sigma d} \ln\left(\frac{R_{\text{b}}^2}{2R_{\text{eff}}d}\right)\right]^2}. \tag{3.9b}$$

From Eq. (3.9), one can expect that there should be two asymptotic behaviors,

- Far from the bubble surface: $d \gg \frac{3\pi\eta\omega R_{\text{eff}}^2}{8\sigma}$, $k_{\text{b}} \gg \omega\gamma_{\text{int}}$(viscous regime) with

$$G'' \approx \frac{3\pi\eta\omega R_{\text{eff}}^2}{2d} \text{ and } G' \approx \frac{9\pi(\eta\omega R_{\text{eff}}^2)^2}{16\sigma d^2} \ln\left(\frac{R_{\text{b}}^2}{2R_{\text{eff}}d}\right).$$

- Close to the bubble surface: $d \ll \frac{3\pi\eta\omega R_{\text{eff}}^2}{8\sigma}$, $k_{\text{b}} \ll \omega\gamma_{\text{int}}$ (elastic regime) with

$$G'' \approx \frac{32\pi\sigma^2 d}{3\pi\eta\omega R_{\text{eff}}^2 \left[\ln\left(\frac{R_{\text{b}}^2}{2R_{\text{eff}}d}\right)\right]^2} \text{ and } G' \approx \frac{4\pi\sigma}{\ln\left(\frac{R_{\text{b}}^2}{2R_{\text{eff}}d}\right)}.$$

Similar calculation can be performed for no slip boundary condition, which leads to hydrodynamic damping:

$$\omega\gamma_{\text{h}} = \frac{6\pi\omega\eta R_{\text{eff}}^2}{d}, \tag{3.10}$$

and a new expression of the mechanical impedance:

$$G' = \frac{6\pi\eta\omega R_{\text{eff}}^2}{d} \frac{\frac{3\pi\eta\omega R_{\text{eff}}^2}{2\sigma d} \ln\left(\frac{R_{\text{b}}^2}{2R_{\text{eff}}d}\right)}{1+\left[\frac{3\pi\eta\omega R_{\text{eff}}^2}{2\sigma d} \ln\left(\frac{R_{\text{b}}^2}{2R_{\text{eff}}d}\right)\right]^2}, \tag{3.11a}$$

$$G'' = \frac{6\pi\eta\omega R_{\text{eff}}^2}{d} \frac{1}{1+\left[\frac{3\pi\eta\omega R_{\text{eff}}^2}{2\sigma d} \ln\left(\frac{R_{\text{b}}^2}{2R_{\text{eff}}d}\right)\right]^2}. \tag{3.11b}$$

3.3 Experimental Results

3.3.1 Visco-capillary effect studied by thermal noise excitation of the AFM probe

To probe the visco-capillary interaction with the bubble, we choose a cantilever whose resonance is large enough (Eq. (2.15)), to neglect the elastic response form the impurity contamination. In this case, the flow satisfies full slip boundary condition at the bubble interface and

Eqs. (3.9) can be use to describe the visco-capillary interaction between the oscillating sphere and the bubble.

The liquid-gas interface was prepared by placing a spherical air bubble with a radius $R_{\mathrm{b}} = 220.0 \pm 4.0\ \mu\mathrm{m}$ on PS surface using a micro-syringe in the similar way of Sec. 2.3.2. The experiment was performed using an AFM (Resolve, Bruker, USA). A spherical borosilicate particle (MO-Sci Corporation) with a radius $R = 44.0 \pm 0.8\ \mu\mathrm{m}$ was used. The sphere was glued to the end of a silicon cantilever (NP, Bruker) using epoxy (Araldite, Bostik, Coubert). The cantilever stiffness $k_{\mathrm{c}} = (0.35 \pm 0.02)\ \mathrm{N/m}$ was calibrated by fitting the power spectral density far from the surface using Eq. (1.28) with resonance frequency, quality factor and bulk damping coefficient are $f_{\mathrm{c}} = 3.48 \pm 0.05\ \mathrm{kHz}$, $Q_0 = (4.7 \pm 0.1)$ and $\gamma_{\mathrm{bulk}} = k_{\mathrm{c}}/(2\pi f_{\mathrm{c}} Q_0) = (3.4 \pm 0.3) \times 10^{-6}\ \mathrm{N \cdot s \cdot m^{-1}}$, respectively.

The external excitation of the AFM was switched off. The cantilever was only driven by thermal noise. The maximum thermal oscillation amplitude was less than $1.0\ \mathrm{nm}$. Therefore, the influence of cantilever oscillation on the separation distance can be neglected. The distance between the sphere and the bubble was controlled by the integrated stage step motor. Each separation distance was adjusted by displacing the cantilever vertically using the step motor with reproducibility less than $1.0\ \mu\mathrm{m}$. The position at which the cantilever deflection signal changed was taken as contact point, namely, the zero separation distance. The thermal noise signal of the cantilever deflection was acquired using an analog to digital (A/D) acquisition board (PCI-4462, National Instrument, USA) with a sampling rate of $80\ \mathrm{kHz}$. From the acquired data, the spectral density of the thermal noise was calculated.

For a vibrating colloidal probe interacts with a bubble interface, the motion equation of the tip Eq. (1.22) becomes to

$$m^* \ddot{a}(t) + \gamma_{\mathrm{bulk}} \dot{a}(t) + k_{\mathrm{c}} a(t) = F_{\mathrm{Thermal}} - (G' + jG'')a(t). \tag{3.12}$$

And then we get

$$-m^*\omega + k_c + G' + j\omega \left(\gamma_{\mathrm{bulk}} + \frac{G''}{\omega} \right) = F_{\mathrm{Thermal}}. \tag{3.13}$$

Thus the power spectral density can be fitted by equation:

$$\mathrm{PSD}(X, f) = \frac{c_1}{[(f_{\mathrm{c}}'^2 - f^2)^2 + (f_{\mathrm{c}}' f/Q')^2]}, \tag{3.14}$$

through which the quality factor and the resonance frequency can be obtained, and c_1 is a fitting parameter. Using Eqs. (3.9), the resonance frequency f_{c}' and quality factor Q' are given by:

$$f_{\mathrm{c}}' \approx f_{\mathrm{c}} + \frac{\pi \eta f_{\mathrm{c}} (3\eta\omega_c R_{\mathrm{eff}}^2)^2}{32 k_{\mathrm{c}} \sigma d^2} \frac{\ln\left(\frac{R_{\mathrm{b}}^2}{2R_{\mathrm{eff}} d}\right)}{1 + \left[\frac{3\eta\omega_c R_{\mathrm{eff}}^2}{8\sigma d} \ln\left(\frac{R_{\mathrm{b}}^2}{2R_{\mathrm{eff}} d}\right)\right]^2}, \tag{3.15}$$

$$Q' \approx \frac{Q_0}{1 + \frac{3\pi\eta R_{\mathrm{eff}}^2}{2\gamma_{\mathrm{bulk}} d} \frac{1}{1 + \left[\frac{3\eta\omega_c R_{\mathrm{eff}}^2}{8\sigma d} \ln\left(\frac{R_{\mathrm{b}}^2}{2R_{\mathrm{eff}} d}\right)\right]^2}}. \tag{3.16}$$

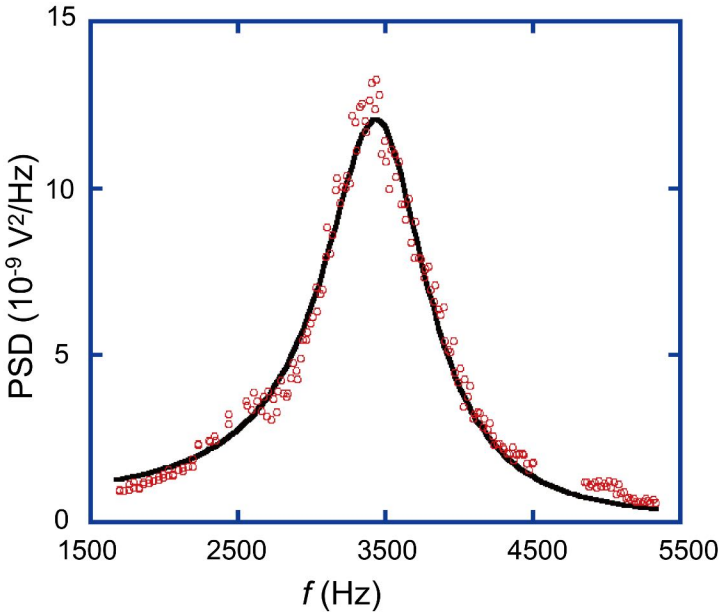

Figure 3.2: *The power spectral density (PSD) obtained for the sphere at a distance of* $14\ \mu\mathrm{m}$ *from the bubble surface. The solid line is the fitting curve by Eq.* (3.14).

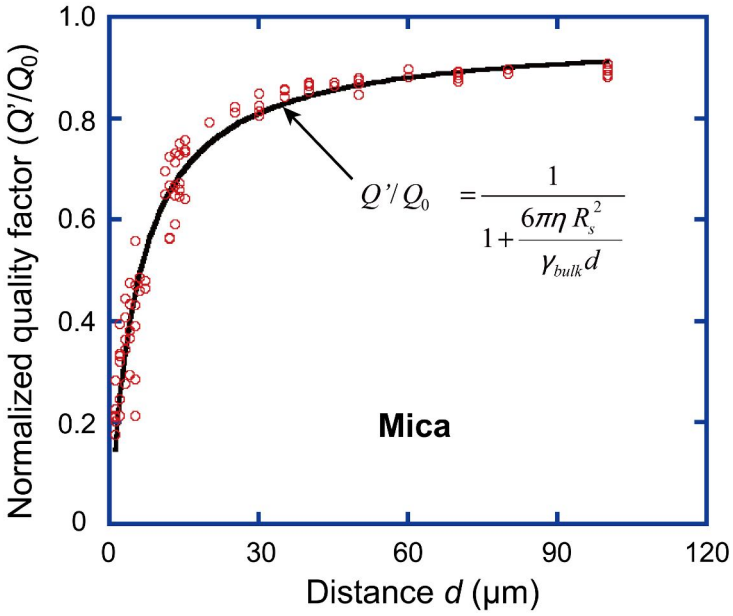

Figure 3.3: *The normalized quality factor versus distance measured on mica surface in pure water. The solid line represents the fitting curve with non-slip boundary condition:* $Q'/Q_0 = 1/\left(1+\frac{6\pi\eta R^2}{\gamma_{\mathrm{bulk}}d}\right)$.

An example of power spectral density obtained at a distance of $14\ \mu\mathrm{m}$ from bubble surface is shown in Fig. 3.2. The solid line is the fitting curve by Eq. (3.14).

Besides air-water interfaces, here a mica surface was used to provide hydrophilic solid-liquid interface for comparison. The normalized quality factor (with respect to bulk values) versus the distance for the colloidal probe on mica is shown in Fig. 3.3. The damping on mica surface is given by $\gamma_0 = 6\pi\eta R^2/d$ calculated using a non slip boundary condition. The quality factor on mica can then be fitted using the expression: $Q_{\mathrm{NS}}(d) = Q_0/\left(1+\frac{6\pi\eta R^2}{\gamma_{\mathrm{bulk}}d}\right)$ (see Fig. 3.3).

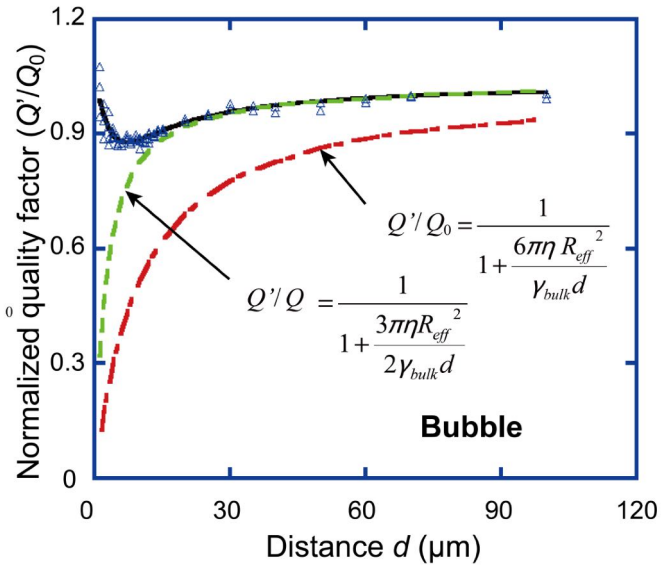

Figure 3.4: *The quality factor versus distance which was measured on bubble surface in pure water. The solid black line is the fitting curve by Eq. (3.16) and the green dotted line and the red dashed-dotted line are the theoretical simulating curves for quality factor of the full slip boundary condition* $Q'/Q_0 = 1/\left(1+\frac{3\pi\eta R_{\mathrm{eff}}^2}{2\gamma_{\mathrm{bulk}}d}\right)$ *and non-slip boundary condition* $Q'/Q_0 = 1/\left(1+\frac{6\pi\eta R_{\mathrm{eff}}^2}{\gamma_{\mathrm{bulk}}d}\right)$*, respectively, neglecting capillary response.*

The quality factor measured on the bubble is presented in Fig. 3.4, which is different from the results obtained on mica surface. The quality factor starts from the bulk value Q_0 and decreases with the decreasing of separation distance between the bubble and the sphere. After the quality factor reaches a minimum value, it begins to increase with decreasing of separation distance. At large separation the data coincide with the theoretical curve calculated assuming full slip boundary conditions on the bubble surface. Indeed the cantilever resonance frequency is very large compared with the frequency that characterize the contribution of impurities to the flow $\omega_0/2\pi = \Pi_0/16\pi\eta R_{\mathrm{eff}}$ presented in chapter 2 and the value is around 135 Hz. At small separation distance, the bubble elastic deformation accommodates the motion of the sphere.

This cancels the viscous flow of the liquid, leading to the increase of the quality factor Q'.

Moreover, as expected by Eq. (3.15), the elastohydrodynamic coupling would induce a shift of the resonance frequency of the cantilever. The change of resonance frequency of the colloidal probe with changing separation distance is shown in Fig. 3.5, which fits well with Eq. (3.15). The resonance frequency increases sharply as the sphere is very close to the bubble surface.

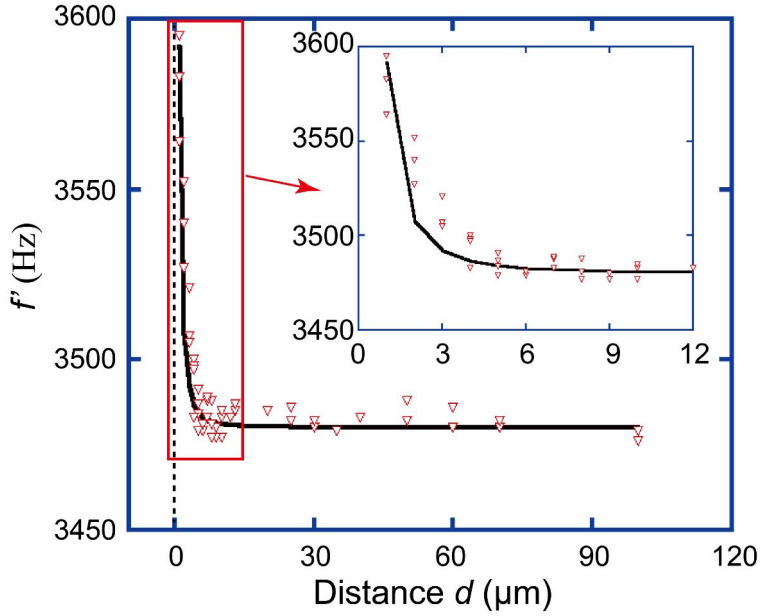

Figure 3.5: *The resonance frequency of the cantilever versus the separation distance between the sphere and the bubble interface. The solid line is the fitting curve by Eq.* (3.15)*.The inset figure is the zoomed one for the area selected by the rectangular box.*

3.3.2 Visco-capillary effect studied by acoustic excitation of the AFM probe

In this part, the cantilever is driven at the frequency much lower than the bubble vibration resonance to avoid the bubble shape oscillation that complicate the modeling of the sphere-bubble interaction. The experiment was performed using an AFM (Bruker, Bioscopy II) equipped with a liquid cell (DTFML-DD-HE). The cantilever with stiffness of $k_c = 0.250 \pm 0.005$ N/m and the sphere with radius $R = 53.1 \pm 1$ μm were used to probe the visco-capillary effect of the bubble surface. The devices used in this experiment is same to the experiment presented in chapter 2. The bubble was deposited on PS surface in 2 mM SDS solution. The experiment was performed at room temperature (21 °C).

Due to presence of the surfactant, the characteristic frequency is $\omega_0 \sim 4$ kHz for 2 mM SDS solution (the driving frequencies are 50 Hz, 100 Hz and 200 Hz), in which cases the bubble surface could be considered as no slip boundary. and the elastic force due to the contamination can also be neglected.

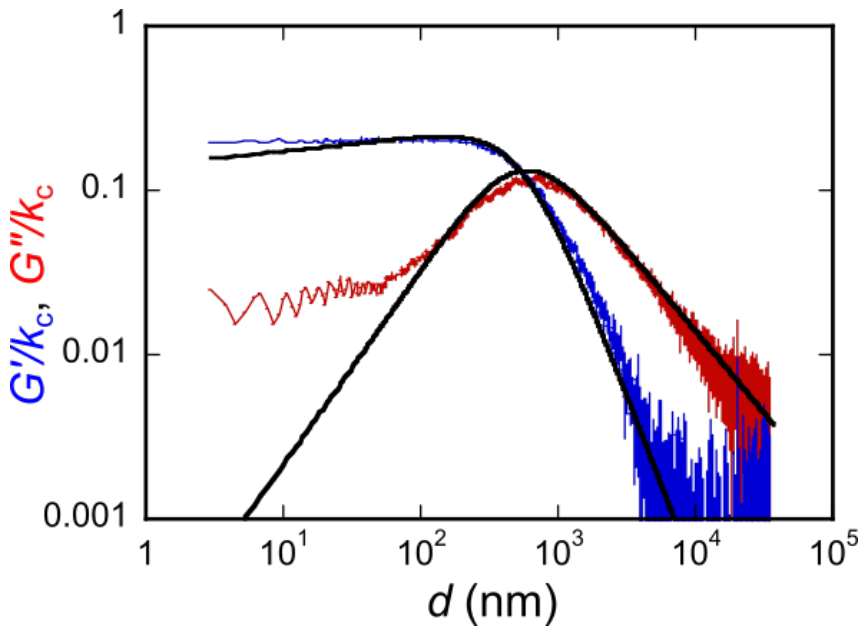

Figure 3.6: *The measured mechanical impedance* G'/k_c, G''/k_c *versus gap distance* d *at* 200 Hz *with the bubble radius of* $R_b = 321 \pm 3$ μm *in* 2 mM *SDS solution. The solid lines are the fitting curves using Eqs.* (3.11)*. The only adjusting parameter is the surface tension* σ*, which gives a value of* $\sigma = 53 \pm 2$ *mN/m.*

The viscous G'' and elastic G' component of the impendance are extracted[1] from the measurement of the amplitude and phase of the cantilever. Figure 3.6 shows the elastic component G'/k_c and viscous component G''/k_c versus the gap distance d between the probe and the bubble. The radius of the bubble is $R_b = 321 \pm 3$ μm which was deposited in 2 mM SDS solution, and the oscillation frequency is 200 Hz. The solid lines are the fitting curves by Eqs. (3.11). The only adjusting parameter is the surface tension σ of air-water interface, which gives us a value of $\sigma = 53 \pm 2$ mN/m. The surface tension was also measured by Wilhelmy plate method, which gives the value of $\sigma = 50 \pm 2$ mN/m. The surface tension values obtained by the both methods are close to each other.

The intersection between viscous component and elastic component (*i.e.* $G' = G''$), leads to relation of

$$\frac{6\pi\eta\omega R_{\text{eff}}^2}{d_0} = \frac{4\sigma}{\ln\left(\frac{R_b^2}{2R_{\text{eff}}d_0}\right)}. \tag{3.17}$$

Figure 3.7 shows the intersection distance d_0 for different oscillation frequencies. The open squared dots represent the measurement results, while the solid line represents the calculation using Eq. (3.17). The intersection distances versus the frequency are in good agreement with the calculated distance using Eq. (3.17).

[1]Note here, the viscous G'' and elastic G' components are related to the calculation in Sec. 2.3.1 by $G'' = \gamma_{\text{int}}\omega$, $G' = k_{\text{int}}$.

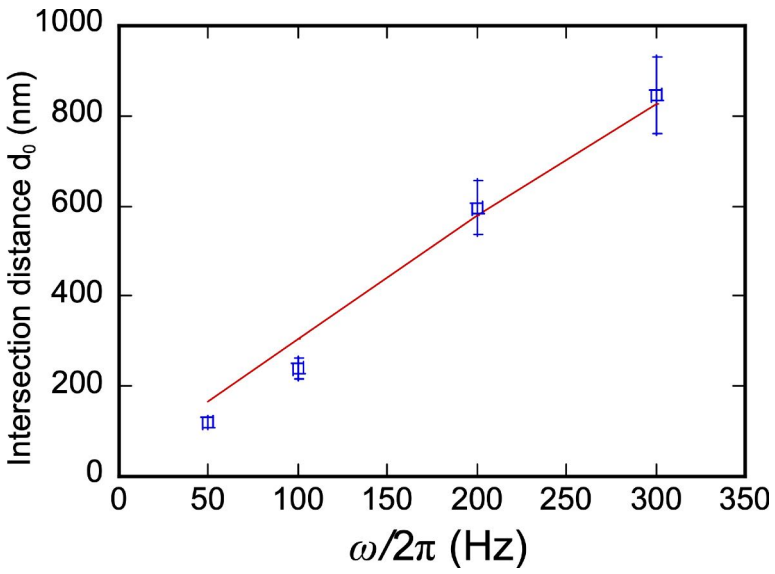

Figure 3.7: *The intersection distance d_0 versus the working frequency $\omega/2\pi$. The open squared dots represent the experimental results measured in* $2\ \mathrm{mM}$ *SDS solution, and the bubble radius is* $R_\mathrm{b} = 321 \pm 3\ \mu\mathrm{m}$. *The solid line shows the results calculated by Eq.* (3.17).

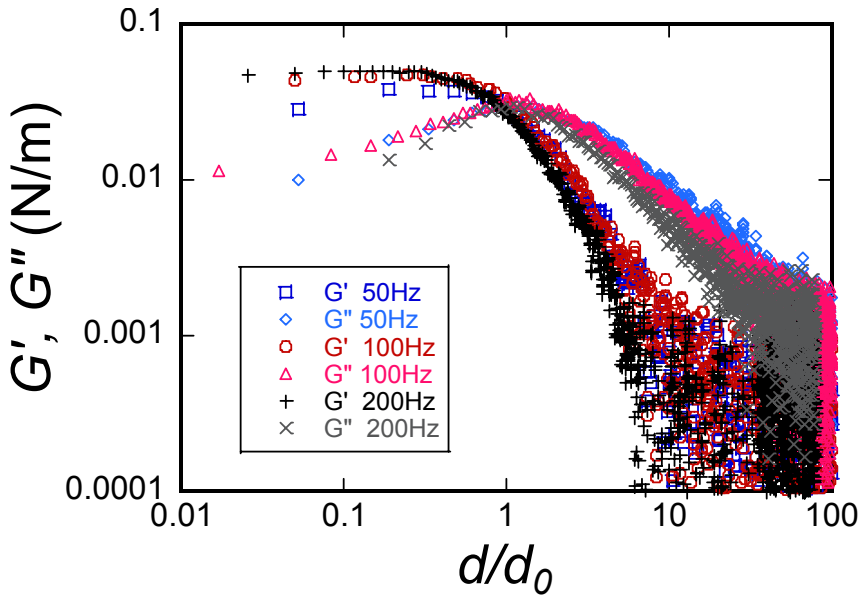

Figure 3.8: *The measured mechanical impedance versus the normalized distance d/d_0 for three different driving frequencies (* $50\ \mathrm{Hz}$, $100\ \mathrm{Hz}$ *and* $200\ \mathrm{Hz}$*).*

In Fig. 3.8, the mechanical impedance versus the normalized distance (d/d_0) are plotted for different oscillation frequencies (50 Hz, 100 Hz and 200 Hz). All the curves for these three oscillation frequencies collapse together. The simplified model is in a good agreement with the experimental results. However, in Fig. 3.6, a discrepancy is observed in both viscous and elastic

components between the experimental results and the simplified model given by Eqs. (3.11) at small distance. Both viscous and elastic components saturate to constant values.

3.4 Numerical Model for Visco-Capillary Effect

Considering the bubble deformation $\xi(r,t)$ due to the hydrodynamic pressure, the confined thickness $h(r,t)$ is expressed by:

$$h(r,t) = d + \frac{r^2}{2R_{\text{eff}}} + \xi(r,t) + Z(t). \tag{3.18}$$

where $Z = Z_0 e^{j\omega t}$ is the instantaneous position of the sphere as defined before, $\xi(r,t)$ is the deformation of the bubble in vertical direction. Using non-slip boundary condition on both sphere and bubble surfaces, from the lubrication theory, we have

$$\frac{\partial h(r,t)}{\partial t} = \frac{1}{12\eta r}\frac{\partial}{\partial r}\left[rh^3(r,t)\frac{\partial}{\partial r}p(r,t)\right]. \tag{3.19}$$

Using an harmonic decomposition $\xi(r,t) = \xi(r)e^{j\omega t}$ and $p(r,t) = p(r)e^{j\omega t}$, and injecting Eq. (3.18) into Eq. (3.19), we obtain

$$j\omega\left(Z_0 + \xi(r)\right) = \frac{1}{12\eta r}\frac{\partial}{\partial r}\left(rh^3 p(r)\right). \tag{3.20}$$

The deformation field of the bubble $\xi(r)$ is related to the pressure field $p(r)$ by Young-Laplace equation $p(r) = \sigma\Delta\xi(r)$ presented in Eq. (3.1). Such a visco-capillary problem is sensitive to the total size of the system: the central deformation diverges logarithmically with the system size [68, 80]. Therefore, it is necessary to introduce a cut-off radius b in the model. The excess pressure and the deformation fields are set to zero at radial distances larger than the cut-off radius, *i.e.*:

$$p(r) = 0,\ \xi(r) = 0, \qquad r > b. \tag{3.21}$$

Therefore the mechanical impedance G is calculated by

$$G = -\frac{F_{\text{h}}}{Z_0} = -\frac{2\pi\int_0^b rp(r)\mathrm{d}r}{Z_0}.$$

By introducing the typical visco-capillary length $d_{\text{c}} = 16\eta\omega R_{\text{eff}}^2/\sigma$, the mechanical impedance can be expressed in the form of:

$$G = \frac{6\pi\eta R_{\text{eff}}^2\omega}{d_{\text{c}}}g\left(\frac{d}{d_{\text{c}}}\right). \tag{3.22}$$

where g is a complex function of d/d_{c}. Using the discrete Hankel transforms to solve theses equations, g can be obtained numerically.

Figure 3.9 shows the dimensionless viscous and elastic components versus the normalized distance d/d_c for the bubble in 1 mM SDS solution. The bubble radius is $R_b = 346$ μm, the contact angle is $\theta_c = 81.5$ ° and the sphere is vibrated at the frequency of 200 Hz, which is small enough to satisfy $\omega \ll \omega_0$. The open circles represent the experimental results extracted from the measurements of amplitude and phase of the sphere oscillation. The solid lines are the numerical results calculated using Eq. (3.22). The fitted value of the surface tension is $\sigma = 58$ mN/m, which is very close to the value $\sigma = 57.5$ mN/m measured by Wilhelmy plate method presented in Sec. 1.2.4. Note here, in the numerical calculation, half of the contour length of the bubble $b = R_b(\pi - \theta_c)$ is taken as the cut-off length.

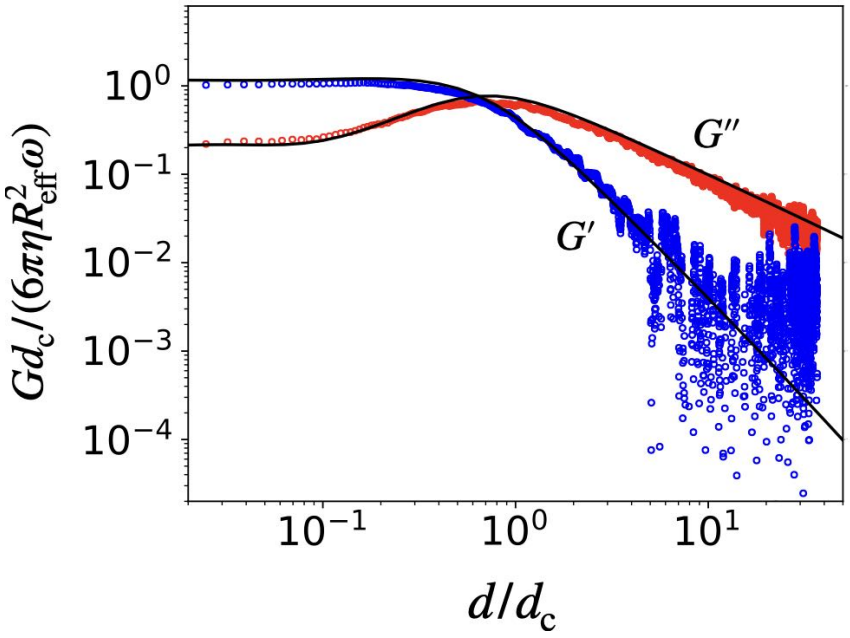

Figure 3.9: *The dimensionless mechanical impedance versus the normalized distance by typical distance d_c measured in 1 mM SDS solution. The blue and red open circle represent the elastic and viscous parts of the experimental results respectively, and the solid lines represent the numerical solution of Eq. (3.22). The only fitting parameter is the surface tension σ, which gives the value of $\sigma = 58$ mN/m.*

We have performed a series of experiments with SDS concentrations ranging from 0.2 mM to 40 mM. The sphere was driven at 200 Hz for all experiments. The fitted values of surface tension as a function of SDS concentration are presented in Fig. 3.10. We observe that the surface tension globally decreases with increasing surfactant concentration, as expected. At small concentrations, the (< 8 mM), the values of fitted surface tension are in a good agreement with the results measured using Wilhelmy plate method. However, at large SDS concentrations, the fitted values of surface tension are lower than the results measured by Wilhelmy plate method. It may result from two sources: first, the surface elasticity may need to be taken into account; second, the oscillation of the sphere may excite bubble shape oscillation (the presence of the

surfactant at the bubble surface may results in a shift of resonance frequency of bubble oscillation).

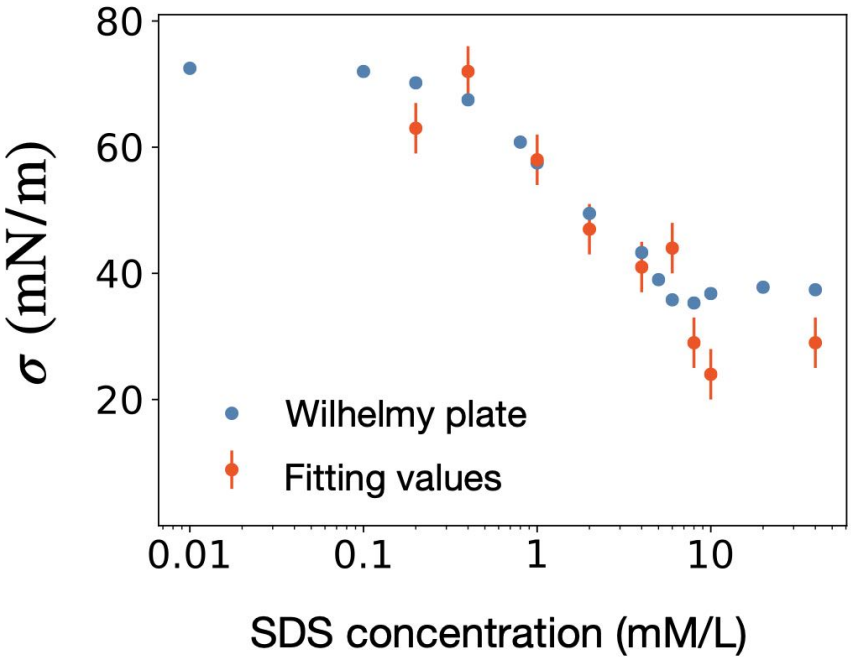

Figure 3.10: *The air-water surface tension as a function of SDS concentration as obtained from the fits of the mechanical impedance (red dots) and measurements using Wilhelmy plate method (blue dots).*

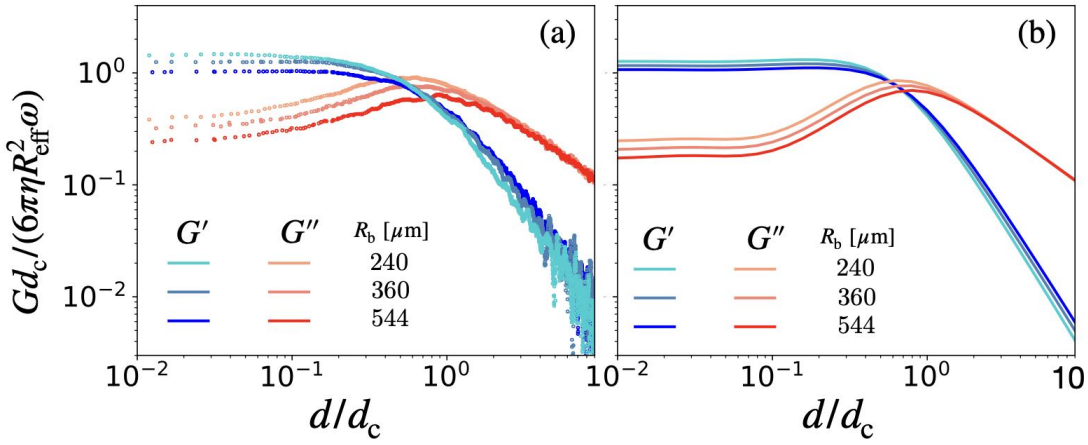

Figure 3.11: *The dimensionless mechanical impedance versus the normalized distance by characteristic distance* d_c *for three different bubbles.* ***a)*** *shows the experimental results and* ***b)*** *shows the theoretical model calculated form Eq.* (3.22).

In order to test the influence of bubble size, *i.e.* the cut-off length b, we performed an experiment with three different sizes of bubble in $1\ \mathrm{mM}$ SDS solution with a driving frequency of $200\ \mathrm{Hz}$. In Fig. 3.11, the dimensionless mechanical impedance as a function of normalized distance are plotted for theses three bubbles. The radii of the bubbles are $240\ \mu\mathrm{m}$, $360\ \mu\mathrm{m}$ and $544\ \mu\mathrm{m}$, respectively. The experimental curves are shown in Fig. 3.11a, while the theoretical ones are shown in Fig. 3.11b where the cut-off length is set to half of the contour length of the undeformed bubble surface as before. The dimensionless mechanical impedance is generally found to depend on the bubble size which is correctly reproduced by the theoretical model. At small distance, the dependence on the bubble size is more important and both viscous and elastic components of the dimensionless impendance decrease as the bubble size increases. This observation highlights the importance of finite size effect in visco-capillary system.

3.5 Conclusion

In this chapter, we have studied the elastohydrodynamic coupling between the pressure of the confined flow and the capillary deformation of the bubble. We found that at large distance, the viscous component of the coupling dominates the interaction. For a distance equal to $d_{\mathrm{c}} = 16\eta\omega R_{\mathrm{eff}}^2/\sigma$ (visco-capillary length), both components of the mechanical impedance are in the same order of magnitude. At small separation distance, the bubble elastic capillary deformation accommodates the motion of the sphere. This cancels the viscous flow of the liquid, leading to the decrease of the damping component of the interaction.

To probe the visco-capillary interaction, two methods – thermal excitation and external acoustic excitation– have been used to excite the cantilever. To analyze our measurements, a simplified model based the spring-dashpot in series was developed. The experimental results obtained from both methods of cantilever excitation are in a qualitative agreement with the simplified model. At very small distance, a discrepancy is observed between the experimental results and the simplified model. To investigate the interaction at very small distance, we have performed numerical calculation to solve the combined Navier-Stokes and Young-Laplace equations in the frame of lubrication approximation. The numerical calculations are in good agreement with the experimental results and allow us to measure the surface tension of bubble interface without contact.

Once the experimental setup is improved, it can be a powerful tool for tensiometry of air-water interfaces. Beside the fact that the measurement can be done in no-contact (no-invasive) between the tip and the interface, the volume of the liquid required can be as small as tens microliters.

Chapter 4

Thermal Capillary Wave on Hemispherical Bubble Probed by AFM

Contents

4.1 Context **63**
4.2 Modeling of Bubble Shape Vibration **64**
4.3 Method and Experimental Results **72**
4.3.1 Experimental setup and method 72
4.3.2 Results 75
4.4 Conclusion **79**

4.1 Context

Molecules that lie at the interface between two phases are subject to forces that are different from those that are in the bulk. These forces act so as to minimize the surface energy and give rise to the surface tension of interfaces [81, 82]: the energy cost to maintain the phase separation of the fluids. These interfaces are host to thermal fluctuations, which are at the origin of the roughness of the interfaces: the fluctuations of the local positions of molecules distort the shape of the interfaces. This phenomenon described using the notion of thermal capillary waves has been the subject of theoretical studies for several decades [83, 84, 85, 86, 87, 88, 89, 90, 91, 92]. When such interfaces are confined by imposing a vanishing velocity at the ends of the interface as in the presence of walls, the spectrum of the fluctuations will present sharp resonance peaks for specific frequencies for which the motion of the interface is much stronger than that for other frequencies.

Experimental studies of thermal capillary waves are mainly performed using techniques such as X-ray reflectivity [93], surface quasi-elastic light scattering (SQELS) [94, 95], optical

interferometry [96, 97] and high speed video imaging [91, 98]. Such techniques can also shed light on the viscoelastic properties of surfaces and interfaces when decorated by surfactants. These additives, even in minute quantities can alter not only the surface tension of surfaces but render these surfaces rheologically non trivial: such surfaces may acquire a surface elasticity and a surface viscosity [99, 100, 101, 102, 103, 104, 17, 105, 106, 107, 108].

In this chapter, an AFM measurement of the thermal capillary fluctuation on the surface of a bubble deposited on a solid substrate is presented. A model for bubble shape oscillation is addressed to explain the measured bubble resonance frequencies, effective mass and the damping coefficient. The surface viscosity due to the contamination is extracted from the measurement of the additional damping.

4.2 Modeling of Bubble Shape Vibration

We consider a hemispherical bubble which is deposited on a solid surface in water and the radius of the undisturbed bubble is R_{b}. The quality factor of the resonance of the bubble oscillation studied in this chapter is larger than 10 which means that viscous damping of the liquid flow is rather weak. We may assume that the flow is derived from a potential ψ satisfying Laplace's equation, $\nabla^2\psi = 0$ [109]. The spherical coordinates (r, θ, ϕ) centered at the center of the undisturbed bubble is adopted (see Fig. 4.1). For azimuthally symmetry, the solution of this equation is given in the form of [109, 110]:

$$\psi(r,\theta,t) = \sum_{n=0}^{\infty} \frac{b_n(t)}{r^{n+1}} P_n(\cos\theta), \tag{4.1}$$

where P_n is the Legendre function, $b_n(t)$ is a coefficient which is the function of time, and n is the order number. Legendre function satisfies the relations of:

$$\int_0^1 P_{2k}\left(\cos\theta\right) P_{2l}\left(\cos\theta\right) \mathrm{d}\left(\cos\theta\right) = \frac{\delta_{l,k}}{(4k+1)}, \tag{4.2}$$

and

$$\int_0^1 \frac{\partial P_{2k}\left(\cos\left(\theta\right)\right)}{\partial\theta} \frac{\partial P_{2l}\left(\cos\left(\theta\right)\right)}{\partial\theta} \mathrm{d}(\cos\left(\theta\right)) = \frac{2k\left(2k+1\right)}{(4k+1)} \delta_{k,l}, \tag{4.3}$$

where $\delta_{l,k} = 0$ if $k \neq l$, $\delta_{l,k} = 1$ if $k = l$ and k, l are integer numbers.

The flow velocities are given by:

$$v_r\left(r,\theta\right) = \frac{\partial\psi}{\partial r}, \tag{4.4a}$$

$$v_\theta\left(r,\theta\right) = \frac{1}{r}\frac{\partial\psi}{\partial\theta}. \tag{4.4b}$$

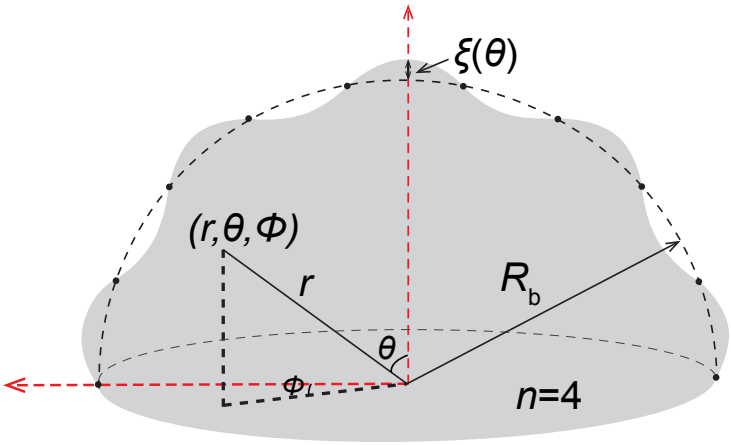

Figure 4.1: *A hemispherical bubble is deposited on a solid surface.*

The impermeability of the substrate requires that the perpendicular velocity of the fluids must vanish on the substrate: $v_\theta\left(r,\theta=\frac{\pi}{2}\right)=-\frac{1}{r}\frac{\partial\psi}{\partial\theta}\left(r,\theta=\frac{\pi}{2}\right)=0$. To satisfy this equality, the value of n should be even number, *i.e.* $n=2k$, which means that only even modes of the bubble shape oscillation can appear for a hemispherical bubble. And then, we have:

$$\psi\left(r,\theta,t\right)=\sum_{k=0}^{\infty}\frac{b_{2k}\left(t\right)}{r^{(2k+1)}}P_{2k}\left(\cos\theta\right). \tag{4.5}$$

The deformation of the hemispherical bubble shape is given by:

$$\xi\left(\theta,t\right)=\sum_{k=0}^{\infty}c_{2k}\left(t\right)P_{2k}\left(\cos\theta\right), \tag{4.6}$$

where the amplitude $c_{2k}\left(t\right)$ is a function of time. The radial velocity of the flow must satisfy the boundary conditions on the surfaces of the bubble: $v_r\left(r=R_\mathrm{b}\right)=\frac{\partial\psi}{\partial r}\left(r=R_\mathrm{b}\right)=\dot{\xi}\left(t,\theta\right)$. And thus we can express $b_{2k}\left(t\right)$ as function of $c_{2k}\left(t\right)$ by

$$\dot{c}_{2k}=-\frac{(2k+1)b_{2k}}{R_\mathrm{b}^{2k+2}}. \tag{4.7}$$

Injecting Eq. (4.7) into the potential expression of Eq. (4.5), we get:

$$\psi\left(r,\theta,t\right)=-\sum_{k=0}^{\infty}\frac{R_\mathrm{b}^{(2k+2)}\dot{c_{2k}}\left(t\right)}{(2k+1)\,r^{(2k+1)}}P_{2k}\left(\cos\theta\right). \tag{4.8}$$

Volume Conservation

Neglecting the dissolution of air molecules into water, the volume of the bubble should be constant, *i.e.*

$$\begin{aligned}\Delta V &= \frac{1}{3}\int_0^{\pi/2}\int_0^{2\pi}\left[(R_\mathrm{b}+\xi)^3 - R_\mathrm{b}^3\right]\sin(\theta)\mathrm{d}\theta\mathrm{d}\phi \\ &= \int_0^{\pi/2}\int_0^{2\pi}\left[(\xi R_\mathrm{b}^2 + R_\mathrm{b}\xi^2)^3 - R_\mathrm{b}^3\right]\sin(\theta)\mathrm{d}\theta\mathrm{d}\phi \\ &= 2\pi {R_\mathrm{b}}^2 c_0\left(t\right) + 2\pi R_\mathrm{b}\sum_{k=1}^{\infty}\frac{c_{2k}^2\left(t\right)}{4k+1} = 0\end{aligned} \tag{4.9}$$

Potential Energy

The potential energy E_p of the bubble surface is given by $E_\mathrm{p} = \sigma\Delta S$, here σ is the surface tension of the bubble surface, S is the surface area of the bubble surface. The change of the bubble surface is given by

$$\begin{aligned}\mathrm{d}\left(\Delta S\right) &= \left(2R_\mathrm{b}\xi + \xi^2 + \frac{1}{2}\left(\frac{\partial\xi}{\partial\theta}\right)^2\right)\sin\left(\theta\right)\mathrm{d}\theta\ \mathrm{d}\phi \\ &= 2\pi\left(2R_\mathrm{b}\xi + \xi^2 + \frac{1}{2}\left(\frac{\partial\xi}{\partial\theta}\right)^2\right)\sin\left(\theta\right)\mathrm{d}\theta.\end{aligned} \tag{4.10}$$

Using the bubble deformation expression of Eq. (4.6), the potential energy is expressed as:

$$\begin{aligned}E_\mathrm{p} &= \sigma\int \mathrm{d}(\Delta S) \\ &= 2\pi\sigma\left(2R_\mathrm{b}c_0 + \sum_{k,l}^{\infty} c_{2k}c_{2l}\int_0^1\left[P_{2k}\left(\cos\left(\theta\right)\right)P_{2l}\left(\cos\left(\theta\right)\right) + \frac{1}{2}\frac{\partial P_{2k}\left(\cos\left(\theta\right)\right)}{\partial\theta}\frac{\partial P_{2l}\left(\cos\left(\theta\right)\right)}{\partial\theta}\right]\mathrm{d}(\cos\left(\theta\right))\right) \\ &= 2\pi\sigma\left(2R_\mathrm{b}c_0 + \sum_{k,l}^{\infty} c_{2k}c_{2l}\left[\frac{1}{4k+1}\delta_{l,k} + \frac{1}{2}\frac{2k\left(2k+1\right)}{4k+1}\delta_{l,k}\right]\right).\end{aligned} \tag{4.11}$$

Using Eq. (4.2) and Eq. (4.9), the expression of potential energy becomes:

$$\begin{aligned}E_\mathrm{p} &= 2\pi\sigma\left(2R_\mathrm{b}c_0 + \sum_{k=1}^{\infty}\frac{2k\left(2k+2\right)+2}{2\left(4k+1\right)}c_{2k}^2\right) \\ &= \frac{2\sigma\Delta V}{R_\mathrm{b}} + \pi\sigma\sum_{k=1}^{\infty}\frac{(2k+2)(2k-1)}{4k+1}c_{2k}^2 \\ &= \pi\sigma\sum_{k=1}^{\infty}\frac{(2k+2)(2k-1)}{4k+1}c_{2k}^2.\end{aligned} \tag{4.12}$$

Kinetic Energy

Using the expression for the velocity of the fluid, we can calculate the kinetic energy E_{k} by [111]:

$$E_{\mathrm{k}} = \frac{1}{2}\rho \iiint (\nabla\psi)^2 \,\mathrm{d}V = \frac{\rho}{2}\int (\psi\nabla\psi)\cdot\vec{n}\mathrm{dS} = \frac{\rho}{2}\int \left(\psi\frac{\partial\psi}{\partial r}\right)_{r=R_{\mathrm{b}}} R_{\mathrm{b}}^2 2\pi\sin(\theta)\,\mathrm{d}\theta, \quad (4.13)$$

here ρ is the density of the fluid surrounding the bubble. Injecting the velocity potential Eq. (4.5) into Eq. (4.13) and using Eq. (4.2), we get the expression for the kinetic energy E_{k}:

$$\begin{aligned} E_{\mathrm{k}} &= R_{\mathrm{b}}^2\pi\rho\int\left(\psi\frac{\partial\psi}{\partial r}\right)_{r=R_{\mathrm{b}}}\sin(\theta)\mathrm{d}\theta \\ &= -\pi\rho R_{\mathrm{b}}^3\sum_{k,l}^{\infty}\frac{\dot{c}_{2k}\dot{c}_{2l}}{(2k+1)}\int_0^1 P_{2k}(\cos(\theta))\,P_{2l}(\cos(\theta))\,\mathrm{d}(\cos(\theta)) \\ &= \pi\rho R_{\mathrm{b}}^3\sum_{k=1}^{\infty}\frac{\dot{c_{2k}}^2}{(2k+1)(4k+1)} \end{aligned} \quad (4.14)$$

Viscous Damping of the Bubble Shape Oscillation

To calculate the viscous damping $\dot{D_{\mathrm{vis}}}$, we use the expression [111]:

$$\dot{D_{\mathrm{vis}}} = \eta\iint\left(\nabla\vec{v}^2\right)\cdot\vec{n}\mathrm{d}S = \eta\iint\frac{\partial\vec{v}^2}{\partial r}\mathrm{d}S = 2\pi\eta R_{\mathrm{b}}^2\int\frac{\partial\vec{v}^2}{\partial r}\sin(\theta)\mathrm{d}\theta. \quad (4.15)$$

here η is the viscosity of the fluid surrounding the bubble. Using Eq. (4.4), we obtain

$$\begin{aligned} \frac{\partial\vec{v}^2}{\partial r} &= 2v_r\frac{\partial v_r}{\partial r} + 2v_\theta\frac{\partial v_\theta}{\partial r} \\ &= -\frac{2}{R_{\mathrm{b}}}\sum_{k,l}^{\infty}(2k+2)\,\dot{c}_{2k}\dot{c}_{2l}\left[P_{2k}(\cos(\theta))\,P_{2l}(\cos(\theta)) + \frac{\frac{\partial P_{2k}(\cos(\theta))}{\partial\theta}\frac{\partial P_{2l}(\cos(\theta))}{\partial\theta}}{(2k+1)(2l+1)}\right]. \end{aligned} \quad (4.16)$$

Injecting Eq. (4.16) in Eq. (4.15), and using Eq. (4.2), Eq. (4.3), we obtain:

$$\begin{aligned} \dot{D_{\mathrm{vis}}} &= 4\pi\eta R_{\mathrm{b}}\sum_{k,l}^{\infty}(2k+2)\,\dot{c}_{2k}\dot{c}_{2l}\int_0^1\left[P_{2k}(\cos(\theta))\,P_{2l}(\cos(\theta)) + \frac{\frac{\partial P_{2k}(\cos(\theta))}{\partial\theta}\frac{\partial P_{2l}(\cos(\theta))}{\partial\theta}}{(2k+1)(2l+1)}\right]\mathrm{d}(\cos(\theta)) \\ &= 4\pi\eta R_{\mathrm{b}}\sum_{k=1}^{\infty}\frac{(2k+2)}{(2k+1)}\dot{c}_{2k}^2. \end{aligned} \quad (4.17)$$

Boundary damping on Solid Wall

To calculate the boundary damping $\dot{D}_\mathrm{b}$ on the substrate wall, we use the expression [111]:

$$\dot{D}_\mathrm{b} = \frac{1}{2}\sqrt{\frac{\omega\rho\eta}{2}}\int_R^\infty \vec{v}^2 2\pi r \mathrm{d}r. \tag{4.18}$$

where $\vec{v}$ is the velocity along the solid wall, *i.e.*

$$\vec{v}^2\left(\theta=\frac{\pi}{2}\right) = v_r^2\left(\theta=\frac{\pi}{2}\right) = \sum_{k,l}^{\infty}\frac{R_\mathrm{b}^{(2k+2l+4)}}{r^{(2k+2n+4)}}\dot{c_{2k}}\dot{c_{2l}}P_{2k}\left(0\right)P_{2l}(0). \tag{4.19}$$

Injecting Eq. (4.19) into Eq. (4.18), we have

$$\begin{aligned}\dot{D}_\mathrm{b} &= \frac{\pi\eta}{\delta}\sum_{k,l}\int_{R_\mathrm{b}}^\infty \frac{R^{(2k+2l+4)}}{r^{(2k+2l+3)}}\dot{c_{2k}}\dot{c_{2l}}P_{2k}\left(0\right)P_{2l}\left(0\right)\mathrm{d}r \\ &= \frac{\pi\eta R_\mathrm{b}^2}{\delta}\sum_{k,l}\frac{\dot{c_{2k}}\dot{c_{2l}}P_{2k}\left(0\right)P_{2l}\left(0\right)}{2k+2l+2} \\ &= \frac{\pi\eta R_\mathrm{b}^2}{\delta}\sum_{k}\frac{\dot{c}_{2k}^2P_{2k}^2\left(0\right)}{4n+2} + \sum_{k,l,l\neq k}\frac{\dot{c_{2k}}\dot{c_{2l}}P_{2k}\left(0\right)P_{2l}\left(0\right)}{2k+2n+2}.\end{aligned} \tag{4.20}$$

where $\delta = \sqrt{2\eta/\rho\omega}$ is the penetrate depth. For vibration frequency close to the resonance ω_{2k}, the amplitude c_{2k} is much larger than the amplitude c_{2l} and thus we can neglect the second term of the right hand side of the previous equation. Therefore, the boundary damping is expressed as:

$$\dot{D}_\mathrm{b} \approx \frac{\pi\eta R_\mathrm{b}^2}{\delta}\sum_{k=1}^{\infty}\frac{\dot{c}_{2k}^2P_{2k}^2\left(0\right)}{4k+2}. \tag{4.21}$$

Lagrange equation: resonance frequency and damping coefficient

For the bubble oscillation, we have

$$\frac{\mathrm{d}}{\mathrm{d}t}\left(\frac{\partial E_\mathrm{k}}{\partial\dot{c}_n}\right) - \frac{\partial E_\mathrm{k}}{\partial c_n} + \frac{\partial E_\mathrm{p}}{\partial c_n} = -\frac{1}{2}\frac{\partial\dot{D}}{\partial\dot{c}_n}. \tag{4.22}$$

The damping $\dot{D}$ is the sum of the bulk viscous damping $\dot{D}_\mathrm{vis}$ and the boundary damping $\dot{D}_\mathrm{b}$ on the substrate: $\dot{D} = \dot{D}_\mathrm{vis} + \dot{D}_\mathrm{b}$. Note here, $n = 2k$ is the even integer numbers. Each term in

Eq (4.22) is obtained from:

$$\frac{\mathrm{d}}{\mathrm{d}t}\left(\frac{\partial E_{\mathrm{k}}}{\partial \dot{c}_n}\right) = \frac{2\pi\rho R_{\mathrm{b}}^3 \ddot{c}_n}{(n+1)(2n+1)}, \tag{4.23}$$

$$\frac{\partial E_{\mathrm{k}}}{\partial c_n} = 0, \tag{4.24}$$

$$\frac{\partial E_{\mathrm{p}}}{\partial c_n} = 2\pi\sigma\frac{(n-1)(n+2)}{(2n+1)}c_n, \tag{4.25}$$

$$\frac{1}{2}\frac{\partial \dot{D}}{\partial \dot{c}_n} = 4\pi\eta R_{\mathrm{b}}\frac{(n+2)}{(n+1)}\dot{c}_n + \frac{\pi\eta R_{\mathrm{b}}^2}{\delta}\frac{\dot{c}_n P_n^2(0)}{2(n+1)}. \tag{4.26}$$

Substituting Eq. (4.23), Eq. (4.24), Eq. (4.25) and Eq. (4.26) into Eq. (4.22), we get

$$\frac{2\rho\pi R_{\mathrm{b}}^3\ddot{c}_n}{(n+1)(2n+1)} + 2\pi\sigma\frac{(n-1)(n-2)}{(2n+1)}c_n = \pi\eta R_{\mathrm{b}}\frac{(n+2)}{(n+1)}\dot{c}_n + \frac{\pi\eta R_{\mathrm{b}}^2}{\delta}\frac{\dot{c}_n P_n^2(0)}{2(n+1)}. \tag{4.27}$$

Eq. (4.27) can be written as

$$\ddot{c}_n + 2\left[\frac{\eta}{\rho R_{\mathrm{b}}^2}(n+2)(2n+1) + \frac{\eta}{8\rho\delta R_{\mathrm{b}}}(2n+1)P_n^2(0)\right]\dot{c}_n + \left[\frac{\sigma}{\rho R_{\mathrm{b}}^3}(n-1)(n+1)(n+2)\right]c_n = 0. \tag{4.28}$$

This equation is in the form of: $\ddot{c}_n + 2\beta_n\dot{c}_n + \hat{\omega}_n^2 c_n = 0$. And the resonance $\hat{\omega}_n$ is given by [110, 109, 112]

$$\hat{\omega}_n = \hat{\alpha}\omega_{\mathrm{ref}}, \tag{4.29}$$

where $\hat{\alpha} = \sqrt{(n-1)(n+1)(n+2)}$ and

$$\omega_{\mathrm{ref}} = \sqrt{\sigma/\rho R_{\mathrm{b}}^3}. \tag{4.30}$$

The damping coefficient β_n is the sum of the viscous damping and the boundary damping coefficients, *i.e.* $\beta_n = \beta_n^{\mathrm{vis}} + \beta_n^{\mathrm{b}}$, where viscous damping coefficient β_n^{vis} is given by [109]

$$\beta_n^{\mathrm{vis}} = \frac{\eta}{\rho R_{\mathrm{b}}^2}(n+2)(2n+1), \tag{4.31}$$

and the boundary damping coefficient β_n^{b} is given by

$$\beta_n^{\mathrm{b}} = \frac{\eta}{8\rho\delta R_{\mathrm{b}}}(2n+1)P_n^2(0). \tag{4.32}$$

Pinned contact line constraint

Assuming that $c_n(t)$ depends on time as $c_n(t) = c_n^0 e^{j\omega t}$ with oscillation amplitude of c_n^0, and the pining of the contact line imposes that the velocity of bubble oscillation on substrate is equal to zero, therefore, we have

$$\dot{\xi}\left(t, \theta = \frac{\pi}{2}\right) = \sum_{k=0}^{\infty}\dot{c}_n P_n\left(\cos\left(\frac{\pi}{2}\right)\right) = j\omega\sum_{n=0}^{\infty}c_n P_n(0) = 0. \tag{4.33}$$

To take into account the pining of the contact line on resonance frequency, we introduce the Lagrange multiplier λ and the function:

$$g\left(c_n\right) = \sum_{n=0}^{\infty} c_n P_n\left(0\right) = 0. \tag{4.34}$$

The Lagrange equation Eq. (4.22) becomes:

$$\frac{\mathrm{d}}{\mathrm{d}t}\left(\frac{\partial E_{\mathrm{k}}}{\partial \dot{c}_n}\right) - \frac{\partial E_{\mathrm{k}}}{\partial c_n} + \frac{\partial E_{\mathrm{p}}}{\partial c_n} = -\frac{1}{2}\frac{\partial \dot{D}}{\partial \dot{c}_n} + \lambda \frac{\partial g}{\partial c_n}. \tag{4.35}$$

Then we have

$$\begin{aligned} &\ddot{c}_n + 2\left[\frac{\eta}{\rho R_{\mathrm{b}}^2}\left(n+2\right)\left(2n+1\right) + \frac{\eta}{8\rho\delta R_{\mathrm{b}}}\left(2n+1\right)P_n^2\left(0\right)\right]\dot{c}_n + \left[\frac{\sigma}{\rho R_{\mathrm{b}}^3}\left(n-1\right)\left(n+1\right)\left(n+2\right)\right]c_n \\ &= \frac{\lambda}{2\rho\pi R_{\mathrm{b}}^3}\left(n+1\right)\left(2n+1\right)P_n\left(0\right), \end{aligned} \tag{4.36}$$

which can be written in the form of

$$\ddot{c}_n + 2\beta_n\dot{c}_n + \Omega_{\mathrm{n}}^2 c_n = \frac{\lambda}{2\rho\pi R_{\mathrm{b}}^3}\left(n+1\right)\left(2n+1\right)P_n\left(0\right). \tag{4.37}$$

where $\Omega_{\mathrm{n}}^2 = \frac{\sigma}{\rho R_{\mathrm{b}}^3}\left(n-1\right)\left(n+1\right)\left(n+2\right)$. And thus, we have

$$c_n = \frac{\frac{\lambda}{2\rho\pi R_{\mathrm{b}}^3}\left(n+1\right)\left(2n+1\right)P_n\left(0\right)}{\Omega_n^2 - \omega^2 + 2j\beta_n\omega}. \tag{4.38}$$

Substituting Eq. (4.38) into Eq. (4.33), we get

$$\sum_{n=0}^{\infty} \frac{\left(n+1\right)\left(2n+1\right)P_n^2(0)}{\Omega_{\mathrm{n}}^2 - \omega^2 + 2j\beta_n\omega} = 0. \tag{4.39}$$

If we neglect the damping term in Eq. (4.39) and using $n = 2k$, we get equation for the resonance frequency given by [111, 109]

$$\sum_{k=1}^{\infty} \frac{\left(2k+1\right)\left(4k+1\right)}{(2k-1)(2k+1)(2k+1) - \alpha_n^2} P_{2k}\left(0\right)^2 = 0. \tag{4.40}$$

The solutions of Eq. (4.40) correspond to the resonances for each mode of the bubble with fixed contact line, *i.e.*

$$\omega_n = \alpha_n \omega_{\mathrm{ref}}. \tag{4.41}$$

The calculated values for the first six resonance modes of α_n are given in Tab. 4.1.

n	2	4	6	8	10	12
$\hat{\alpha}_n$	3.46	9.49	16.73	25.10	34.47	44.74
α_n	5.37	11.86	19.53	28.28	37.99	48.69

Table 4.1: Vibration resonance coefficient for a hemispherical bubble. $\hat{\alpha}_n$ is for a freely moving contact line, with $\hat{\omega}_n = \hat{\alpha}_n \omega_{\text{ref}}$, and α_n is for a pinned contact line, with $\omega_n = \alpha_n \omega_{\text{ref}}$.

It can be easily verified that Eq. (4.39) has complex valued solutions, where $\text{Im}(\omega) = \beta_n$ is the damping coefficient. In the Fig. 4.2, we show the calculated damping β_n for a bubble with radius $R_\text{b} = 500\ \mu m$ (that includes viscous Eq. (4.31) and boundary contributions Eq. (4.32) versus the frequency for two cases, free contact line ($\beta_n^{\text{vis}} + \beta_n^b$) and fixed contact line ($\text{Im}(\omega)$). We can conclude that with a good approximation, the damping of the capillary wave on the bubble in the case of fixed contact line can be safely described by the analytical equations: Eq. (4.31) for the viscous part and Eq. (4.32) for the boundary part.

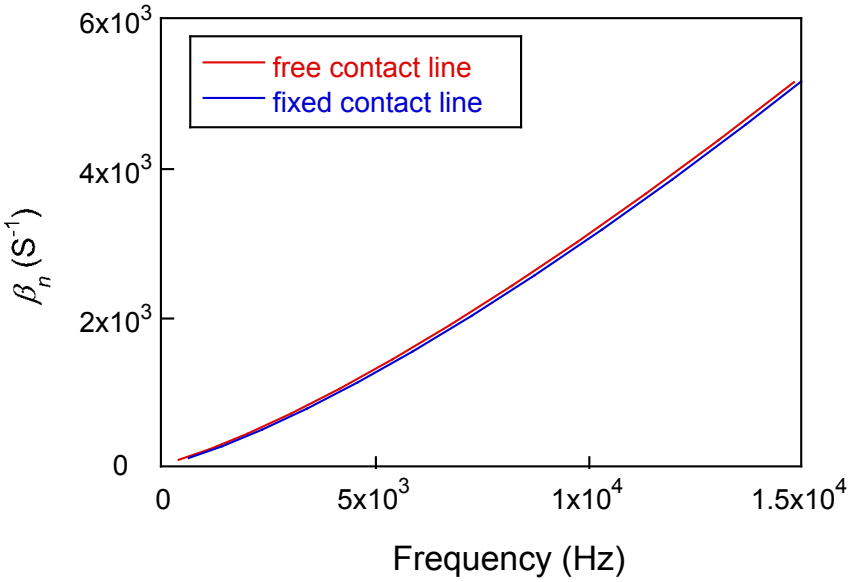

Figure 4.2: *Calculated damping coefficient β_n that includes viscous term β_n^{vis} and boundary term β_n^b versus frequency for the free contact line and the damping extracted from Eq. (4.39) for the fixed contact line (bubble radius $R_b = 500\ \mu m$).*

Note here with an excellent approximation (error of the order of 1%), Eq. (4.31) can be simplified to [111]

$$\beta_n^{\text{vis}} \approx \frac{\eta}{\rho R_\text{b}^2} {\alpha_n}^{4/3} = \frac{2\eta}{\rho^{1/3}\sigma^{2/3}} {\omega_n}^{4/3}. \tag{4.42}$$

Then, taking into account that $(2n+1)P_n^2(0) \approx 1.2$, Eq. (4.32) can be simplified to

$$\beta_n^{\text{b}} \approx \frac{1.2\eta}{8\rho\delta R_\text{b}} = \frac{3\sqrt{2}\eta^{1/2}}{40\rho^{1/2}R_\text{b}} {\omega_n}^{1/2}. \tag{4.43}$$

Damping with impurities

For the general case where the flat interface is partially cover by contaminant, the damping versus the wave number k_n was calculated by by Miles [99] and Rajan *et al.*[108]. For lower solubility of the surfactant, using the capillary equation of $\omega_n^2 = \frac{\sigma}{\rho}k_n^3$, we can express the damping coefficient due to contaminants as:

$$\beta_n^{\mathrm{s}} = \frac{\sqrt{2}\eta^{1/2}{\omega_n}^{7/6}}{4\rho^{1/6}\sigma^{1/3}} \frac{\varepsilon^2 + \varsigma(\varsigma+2)}{(\varepsilon-1)^2 + 1 + \varsigma(\varsigma+2)}, \tag{4.44}$$

with the dimensionless elasticity parameter ε and dimensionless surface viscosity parameter ς , which are respectively given by

$$\varepsilon = \frac{\sqrt{2}\rho^{1/6}}{\eta^{1/2}\sigma^{2/3}}{\omega_n}^{-1/6}\, e_{\mathrm{s}}, \tag{4.45a}$$

$$\varsigma = \frac{\sqrt{2}\rho^{1/6}}{\eta^{1/2}\sigma^{2/3}}{\omega_n}^{5/6}\, \eta_{\mathrm{s}}, \tag{4.45b}$$

where η_s is the surface viscosity, which includes both dilatation and shear viscosities and $e_s = c(\frac{\partial\sigma}{\partial c})_0$ is the surface elasticity. As defined in chapter 2, c is the surfactant surface concentration, and the subscript 0 denotes the quantities at equilibrium.

4.3 Method and Experimental Results

4.3.1 Experimental setup and method

Figure 4.3.a shows the experimental setup used in this experiment. A micro syringe is used to deposit an air bubble on a glass surface spin coated with a polystyrene layer, whose thickness is $100\ \mathrm{nm}$. This air bubble is stable for several hours. We bring a AFM cantilever in contact with the air bubble interface and measure its time-dependent motion, from which we determine the power spectral density of the capillary fluctuations of the interface. The radius of the contact line R_{c} is measured from the optical top-view image (see Fig. 4.3.b), and the contact angle from the side view (see Fig. 4.3.c). Experiments were performed using an AFM (Dimension 3100, Bruker) equipped with a liquid cell (DMFT-DD-HD). Two cantilevers were used in the experiments. One cantilever (CSG01, NT-MDT) with a stiffness of $k_{\mathrm{c}} = 0.12 \pm 0.02\ \mathrm{N/m}$ is denoted as cantilever1 and the other one (MLCT, type B, Bruker) with a stiffness of $k_{\mathrm{c}} = 0.024 \pm 0.002\ \mathrm{N/m}$ is denoted as cantilever2. Both cantilevers were calibrated by thermal noise method.

The position of the cantilever was controlled by the AFM stepping motor stage allowing to bring the tip in contact with the bubble. Once this contact was established, the cantilever was driven solely by the vibrations of the bubble. The maximum amplitude of these vibrations was $< 1\ \mathrm{nm}$. The vertical deflection of the cantilever, due to these oscillations, was acquired

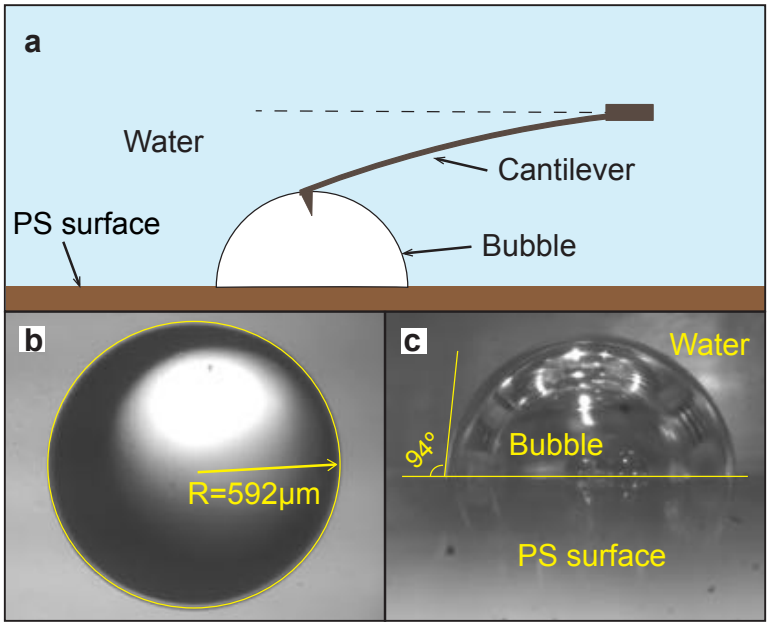

Figure 4.3: ***a**) Experimental setup. The bubble was deposited on polystyrene (PS) surface, and the cantilever tip was used to probe the vibration of the bubble. **b**) Top view and **c**) side view images, from which we obtain the radius of the contact line $R_c = 592 \pm 5\mu m$ and the contact angle of $\theta_c = 94 \pm 2°$.*

by an A/D acquisition board (PCI-4462, National Instrument, USA). From this time series of cantilever deflections, the power spectral density (PSD) was calculated.

Typical PSD curves probed by cantilever1 are shown in Fig. 4.4. The blue curve is measured for the cantilever in bulk water, far from the bubble, and shows clearly the vibrational mode of the cantilever with characteristic frequency near 4 kHz. The main driving force for these cantilever fluctuations is the thermal noise [113, 114, 54]. By fitting the PSD of the cantilever in bulk water by Eq. (1.28), the cantilever stiffness was obtained. The red curve displays the PSD of the cantilever deflection when in contact with the bubble. There are at least five well-defined peaks.

For such bubble, each vibrational mode can be described as an oscillating spring of amplitude $\xi_n(t)$ satisfying the equation of motion

$$m_n \left(\ddot{\xi}_n(t) + 2\beta_n \dot{\xi}_n(t) + \omega_n^2 \xi_n(t) \right) = F_n(t), \tag{4.46}$$

with the effective mass m_n, the damping coefficient β_n, the resonance frequency and the mode number n. We use the shorthand notation $\dot{\xi}_n = \mathrm{d}\xi/\mathrm{d}t$. As we postulated above, the driving force $F_n(t)$ is due to the thermal noise, which is assumed uncorrelated in time and independent for each mode. Taking the Fourier transform of Eq. 4.46, and using $|F_n(\omega)|^2 = 2\beta_n m_n k_B T$,

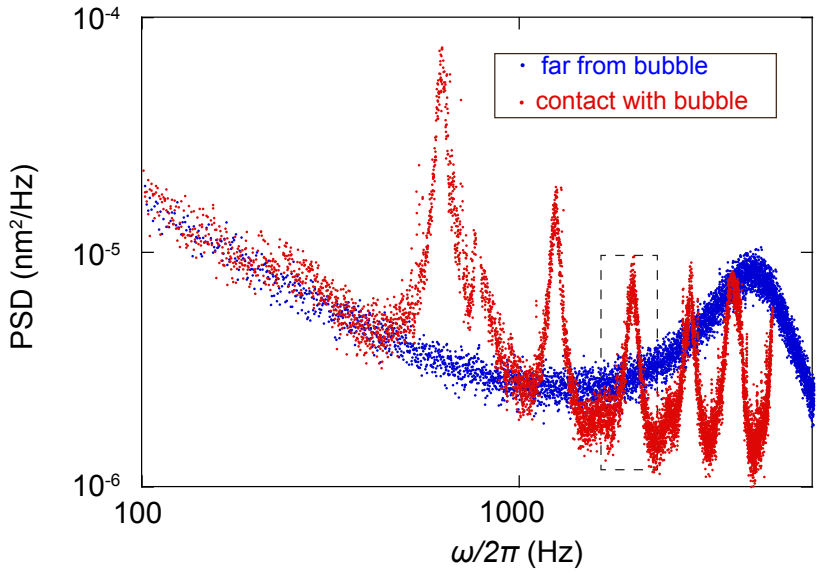

Figure 4.4: *Example of the measured PSD Curves using a cantilever with stiffness* $k_c = 0.12\ \mathrm{N/m}$. *The thermal spectra of the cantilever far from the bubble (blue circles) and in contact with the bubble (red circles) deposited on PS surface.*

we obtain the one sided power spectral density $\mathrm{PSD}\,(\xi,\omega) = \sum_n^\infty \mathrm{PSD}\,(\xi_n,\omega)$ in the form of

$$\mathrm{PSD}\,(\xi,\omega) = \sum_{n=1}^{\infty} \frac{4\beta_n}{\left(\omega^2-\omega_n^2\right)^2 + 4\beta_n^2\omega^2}\frac{k_BT}{\pi m_n}. \tag{4.47}$$

Because in our experiment, the size of the bubble is orders of magnitudes larger than that of cantilever, the cantilever follows the motion of the bubble, *i.e.* $\mathrm{PSD}(Z,\omega) = \mathrm{PSD}(\xi,\omega)$.

Figure 4.5 shows a fit to the third peak of the PSDs shown in Fig. 4.4 using Eq. (4.47). Such fits, which account quantitatively for the shape of the peaks, allow to determine the resonance frequency ω_n as well as the effective mass m_n and the damping coefficient β_n for the different mode numbers n.

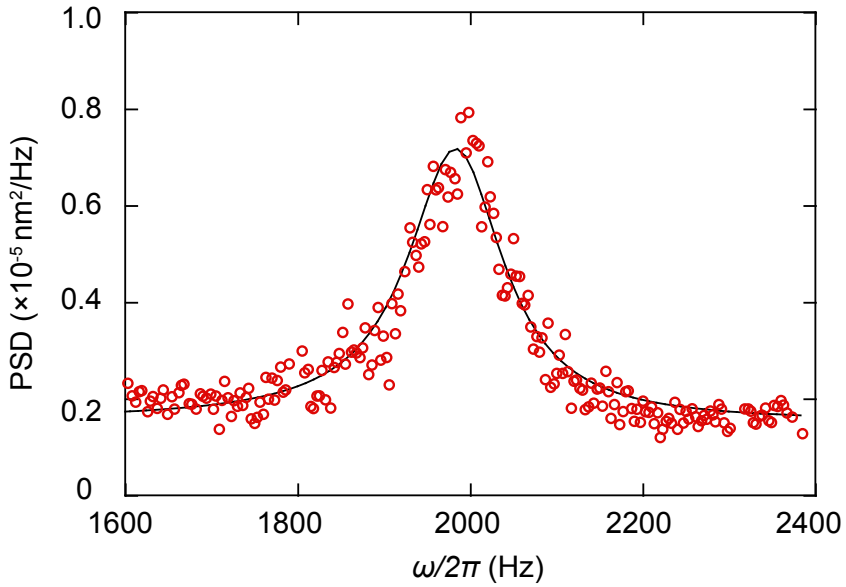

Figure 4.5: *The spectrum (circles) and the fitting curve using Eq.* (4.47) *(solid line) for the third peak of Fig. 4.4.*

4.3.2 Results

The values for the first five resonance frequencies of the power spectral density in Fig. 4.4, are plotted in Fig. 4.6. The theoretical values for both free contact line case (Eq. (4.29)) and pinned contact line case (Eq. (4.41)) are displayed along with the experimental values. The results are well accounted for using non slip boundary condition which leads to the conclusion that the contact line of the bubble on PS surface does not move on the surface but is pinned on the surface, and contact line pinning stiffens the vibrations and enhances the frequencies with respect to those obtained for free contact line, *i.e.* $a_n > \hat{a}_n$.

In order to confirm the validity of conclusion of the pinned contact line on PS surface, we have performed several measurements with different bubble sizes (the radius ranges from $424\ \mu\mathrm{m}$ to $644\ \mu\mathrm{m}$) and two cantilevers. Figure 4.7 shows the normalized resonance frequencies $\omega_n/\omega_{\mathrm{ref}}$ versus the mode number n. All the results for different cases collapse together with the values of α_n (pinned contact line). we safely conclude that the contact line of bubble on PS surface is pinned.

Figure 4.8 displays the effective mass m_n versus mode number n. These masses are extracted from the fits of the PSD using Eq. (4.47). Here data from different bubble radii are displayed. If we express the kinetic energy of bubble in the form of $E_{\mathrm{k}} = \sum_n^\infty \frac{1}{2} m_n \dot{c_n}^2$, Eq. (4.14) becomes to:

$$E_{\mathrm{k}} = \sum_n^\infty \frac{1}{2} \frac{2\pi\rho R_{\mathrm{b}}^3}{(n+1)(2n+1)} \dot{c}_n^2. \tag{4.48}$$

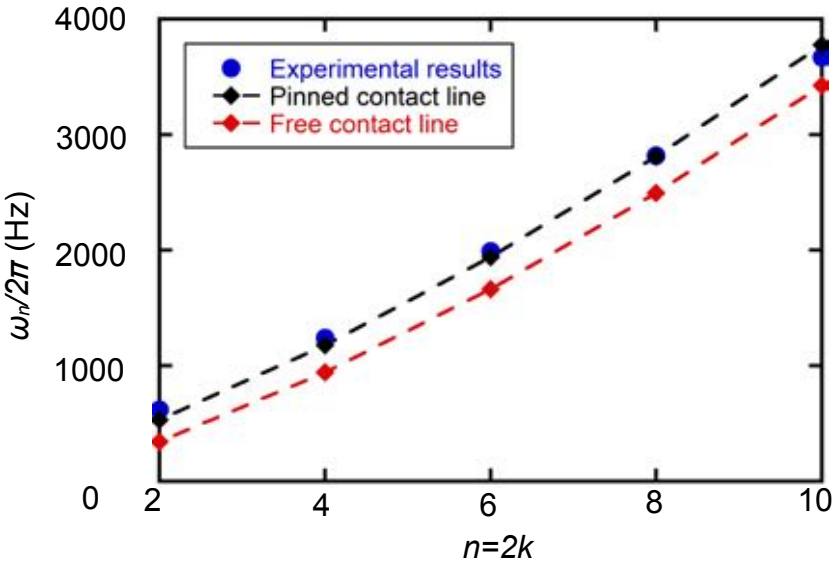

Figure 4.6: *The results of the bubble resonance frequencies $\omega_n/2\pi$ versus the mode numbers n. The black solid line connects the resonance frequency for pinned contact lines, and the red solid line for a freely moving contact line.*

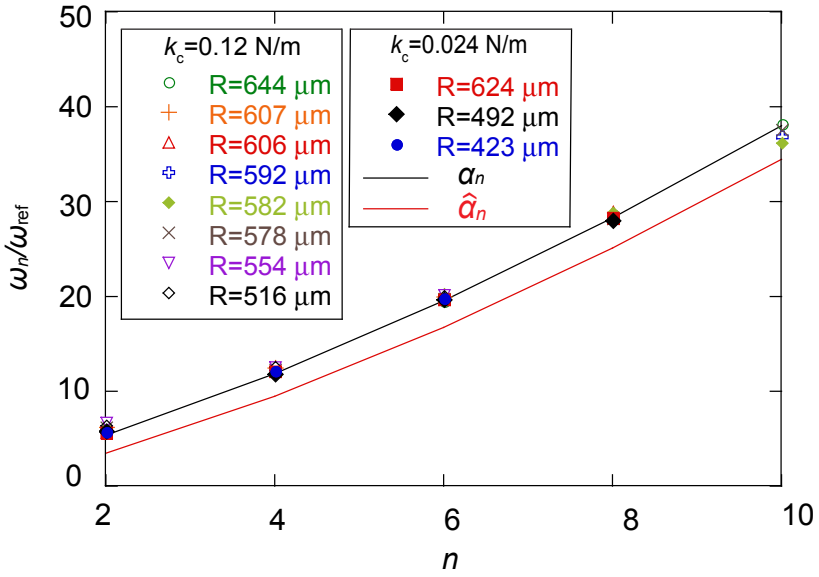

Figure 4.7: *The normalized resonance frequencies ω_n/ω_{ref} versus the mode number n for different bubble sizes and two cantilevers. The red solid and black solid lines represent the normalized resonance frequencies for free contact line $\hat{\alpha}_n$ and fixed contact line α_n, respectively.*

So the effective mass of the bubble oscillation is given by:

$$m_n = \frac{2\pi\rho R_b^3}{(n+1)(2n+1)}. \tag{4.49}$$

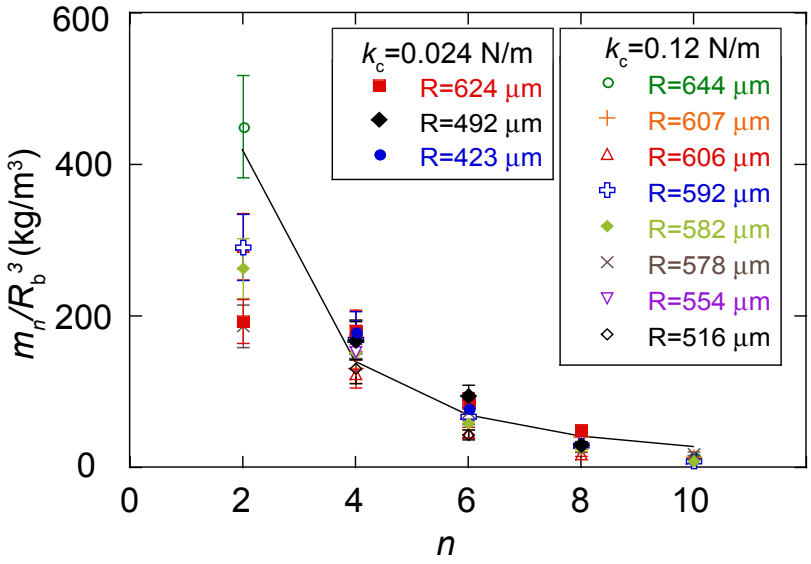

Figure 4.8: *The results of the effective mass normalized by the cubic power of the radius of the bubble versus the mode number for different bubbles. The dots with different colors and shapes represent the different measurements for different bubbles. The black line represents the theoretical results which was given by Eq.* (4.49).

Comparison of the measured effective mass m_n with Eq. (4.49) is shown in Fig. 4.8. Apart from the mode at $n = 2$, the data from different realizations collapse on a single curve.The effective mass has been normalized by the radius of the bubble R_b. Further, the decrease of this effective mass with the mode number n as anticipated by expression Eq. (4.49) is accounted for quantitatively. While our assumption of independent modes seems plausible for higher modes, it is not for the first mode mainly because its frequency is intermediate between the first and second free modes contrary to the higher modes whose frequencies are rather close to the corresponding free mode (see Tab. 4.1).

So far, the bubble vibrations have been treated in the framework of potential flow in an inviscid fluid. Now we turn to the damping coefficient β_n, which gives the width of the resonances in Fig. 4.4. Figure 4.9 shows the damping coefficient β_n obtained with different bubble radii as a function of resonance frequencies $\omega_n/2\pi$. At clean interfaces, viscous damping of β_n^v is the dominant source of dissipation [115] which is the green curve in Fig. 4.9. Although it captures the overall trend of increasing β_n versus ω_n, it is about a factor 2 smaller than experimental values. Thus, viscous damping is not sufficient to explain the measurements. Further, additional damping due to the presence of the solid boundary does not contribute significantly. The blue and red lines take into account both viscous damping and boundary damping and are calculated using two different radii spanning the range of explored values in our experiments. The experimental values remain higher than expected from viscous and boundary damping indicating that additional damping is needed. The black solid line in Fig. 4.9 depicts the total damping

coefficient β_n^{tot}, including viscous damping (Eq. (4.42)), boundary damping (Eq. (4.43)) and the damping due to the surfactants (Eq. (4.44)):

$$\beta_n^{\mathrm{tot}} = \beta_n^{\mathrm{vis}} + \beta_n^{\mathrm{b}} + \beta_n^{\mathrm{s}}. \tag{4.50}$$

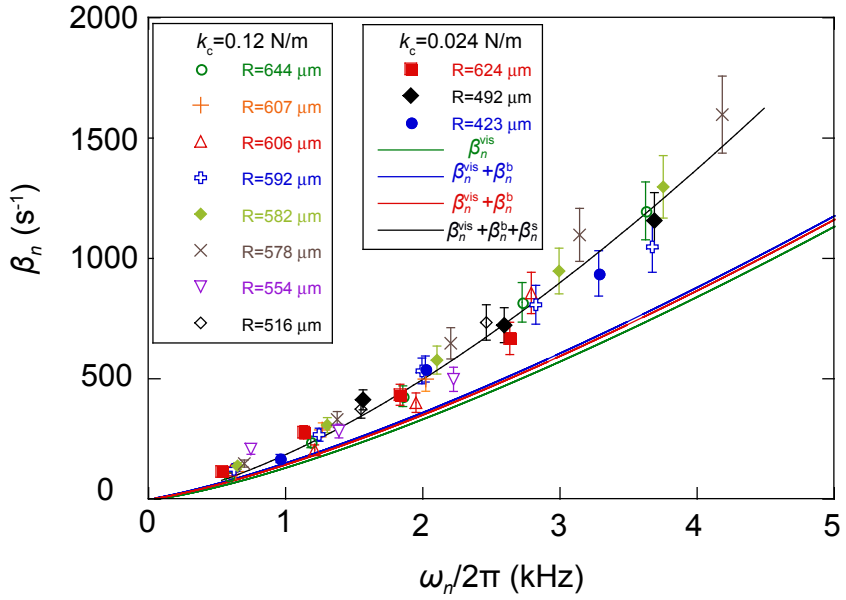

Figure 4.9: *Damping coefficient versus the frequency for different bubbles. The green solid line corresponds to the viscous damping β_n^{vis} as in Eq. (4.42). The red and blue solid lines correspond to the viscous damping plus boundary damping ($\beta_n^{vis}+\beta_n^{b}$), where β_n^{b} was calculated for $R_b = 644\ \mu$m and $423\ \mu$m, respectively by Eq. (4.43). The black solid line is calculated from Eq. (4.50) and accounts for all terms of viscous damping β_n^{vis} (Eq. (4.42)), boundary damping β_n^{b} (Eq. (4.43)) and the effects of surfactants β_n^{s} (Eq. (4.44)), with the surface viscosity is $\eta_s = (1.5 \pm 0.2) \times 10^{-7}$ Pa · s · m.*

For lower surfactant concentration, in Eq. (4.45a) the surface elasticity e_{s} is equal to the surfactant pressure. In chapter 2, the contamination was characterized on bubble surfaces prepared in the similar way and we found that $e_{\mathrm{s}} = \Pi_0 \approx 0.35\ \mathrm{mN/m}$, which leads to a very small value of dimensionless elasticity parameter ε compared to the dimensionless surface viscosity parameter ς. Therefore, the surface elasticity can be neglected in this study.

In the above equation, the surface viscosity η_{s} is the only adjustable parameter, taken as $\eta_s = 1.5 \pm 0.2 \times 10^{-7}$ Pa · s · m. Each of the three contributions to Eq. (4.50) is necessary for a satisfactory fit of the data from different experiments but the contribution of the surface viscosity is crucial for a better agreement with experimental values. Note here the surface viscosity η_s includes both dilatation and shear viscosity, which cannot be distinguished independently in our experiments. Because of the sight difference of the boundary damping β_n^{b} for different bubble sizes (the blue and red lines in Fig. 4.9), in the fitting by Eq. (4.50), we take an intermediate value of $R_{\mathrm{b}} = 500\ \mu$m to calculate the boundary damping coefficient using Eq. (4.43).

The fitted value of η_s is about ten times larger than those reported by Earnshaw [16] for a pure water interface and Zell *et al.* [107] for soluble surfactant covered interfaces. The discrepancy could be due to the fact that in the present work, the surface viscosity measured accounts both for surface dilatational viscosity as well as surface shear viscosity. Further, we believe that our measurements are not devoid of surface contamination. In fact, in one of our previous studies [77] despite the fact that a careful protocol was applied to minimize surface impurities, the air-water surface was found to be prone to contamination rather quickly with drastic effects on the properties of the air-water interface even for minute quantities of contaminants. We believe that there are similar effects here. Remarkably, our experimental technique is capable of probing the surface viscosity with a high precision. This is shown by Fig. 4.9 where the bulk effects are well below the measured damping coefficient. We hypothesize that coupling such a technique with precise techniques for measuring surface shear viscosities (such as that of Zell *et al.* [107]) provides a reliable technique to pin down the surface rheology of interfaces with various surface active agents and disentangle dilatational from shear viscosities.

4.4 Conclusion

In this chapter, we have presented the measurements of the thermal capillary fluctuation of bubbles deposited on solid substrates. The experimental data demonstrate that the soft AFM cantilevers are a powerful tool to probe the thermal motion of bubble. The cantilever deflection signal reflects the thermal fluctuation of the bubble surface directly. The spectrum of the fluctuations presents sharp resonance peaks for specific frequencies for which the motion of the interface is much more prominent than that for other frequencies. The analysis of these peaks allows to measure the resonance frequencies, effective mass and the damping coefficient for each mode of oscillation.

To explain the experimental results, we have presented a model for the bubble shape oscillation. Our measurements are in a good agreement with the model. The model allows us to measure the additional damping due to the presence of minute amounts of contaminants. The experimental results show that the contact line of a hemispherical bubble resting on a solid surface is fixed on the substrate. Moreover, our experimental method provides a useful new tool to probe the surface rheology.

In future experiments, we plan to study the variation of the surface viscosity versus the surfactant concentration. For low range of surfactant concentration, the contribution of the dilatation elasticity is very small, and any variation of the damping versus the concentration would be attributed to a variation of the shear viscosity. For higher range of concentration, the contribution of the dilatation elasticity should be taken into account.

We also project to work with surfaces that allow boundary slippage of contact line on substrates. The motion of the bubble contact line will affect the shape of the power spectrum. It may induce resonance frequency shift and additional damping that would be measured by our apparatus.

Chapter 5

Nanoscale Measurement of the Elastohydrodynamic Lift Force

Contents

5.1 Context 81
5.2 Methods 84
5.2.1 PDMS samples preparation and characterization 84
5.2.2 Calibration of the piezo 86
5.3 Experiment 88
5.3.1 Experimental Setup 88
5.3.2 Results & Disscussion 90
5.4 Conclusion 95

5.1 Context

Elastohydrodynamic is usually encountered for confined flow between soft interfaces. It deals with the coupling between the local pressure induced by the fluid flow and the deformation of soft samples. Recently, such a coupling was studied for much more compliant solids and smaller length scales, in the context of soft matter in confinement and at interfaces [116]. Such concept has been widely used to measure the response of soft surfaces using SFA [20, 22, 21, 117], AFM [118, 67, 23, 80] and optical particle tracking [119].

Two decades ago a new force was theoretically predicted for an object sliding along a soft object [120]. Their predictions suggest that an object moving along a soft surface in viscous fluid is repelled from the surfaces by a normal force F_N exerted on the object [32, 33, 121, 28, 29, 31, 35, 34]. Figure 5.1 summarizes scaling argument to evaluate the elastohydrodynamic lift

force in the case of linear elasticity, thick soft substrate and low Reynolds number [25, 26, 27]. When a rigid cylinder moves along a rigid substrate in a viscous liquid (Fig. 5.1a), the pressure profile $p(x)$ between the confining surfaces is antisymmetric (Fig. 5.1b). The integrated normal force $F_{\mathrm{N}}/L = \int_{-\infty}^{+\infty} p(x)dx$ per unit length is zero, where L is the cylinder length. However, when the substrate is soft (Fig. 5.1c), due to the deformation $\delta(x)$ of the substrate, the pressure profile $p(x)$ is not antisymmetric any more (Fig. 5.1d), which leads to the nonzero normal force with a scaling law of $\frac{\eta^2 V^2 R^2}{G d^3}$ per unit cylinder length, where η is the viscosity of the liquid, R is the radius of the cylinder, d is the gap distance between the apex of the cylinder and the undeformed substrate and G is the shear modulus of the soft substrate [25, 26]. When the object is spherical particle, the cylinder length L should be replaced by the hydrodynamic radius $\sqrt{2Rd}$ (Fig. 5.1e) which gives the scaling law of

$$F_{\mathrm{N}} \sim \frac{\eta^2 V^2}{G} \left(\frac{R}{d}\right)^{5/2}. \tag{5.1}$$

Note here, R is the radius of the spherical particle. and d is the distance between the apex of the sphere and the undeformed substrate. Theoretical calculations show that, as the gap between the object and the soft substrate reduces, the force increases. Eventually, at very small gap, the competition between symmetry breaking and decreasing pressure leads to a saturation of the lift force [25, 26, 27, 28].

Despite the fact that this lift force was studied theoretically by many researchers for different cases (thin and thick samples, compressible and incompressible materials, different shapes of surfaces), a little work was done experimentally [36, 37]. Measurements of the rising speed and the distance to a vertical wall of a bubble allowed to extract an analogous normal force acting on the bubble [122]. A qualitative observation was reported in the context of smart lubricant and elastic polyelectrolytes [123]. A study, involving the sliding of an immersed macroscopic cylinder along an inclined plane, precoated with a thin layer of gel, showed an effective reduction of friction induced by the lift force [124]. The optical tracking of the driven motion of a microparticle in a microfluidic channel decorated with a polymer brush revealed the potential importance of this force in biological and microscopic settings [125]. From the gravitational sedimentation of a macroscopic object along a vertical membrane under tension, another study observed an important normal drift, showing the amplification of the effect for very compliant boundaries induced by slender geometries [126]. The measurement of the shape deformation of a levitating droplet over a moving wall was also used to probe the effects of the lift force [127]. Their results show that the interaction between the particles and the membranes makes the normal velocity of the particles is quadratic in its sedimentation speed as predicted by calculation using soft lubrication theory. However, while this experimental literature provides confidence in the existence of the elastohydrodynamic lift force, as well as in its importance at small scales and for biology, no direct force measurement was performed to date and the saturation at the nanoscale was not yet observed.

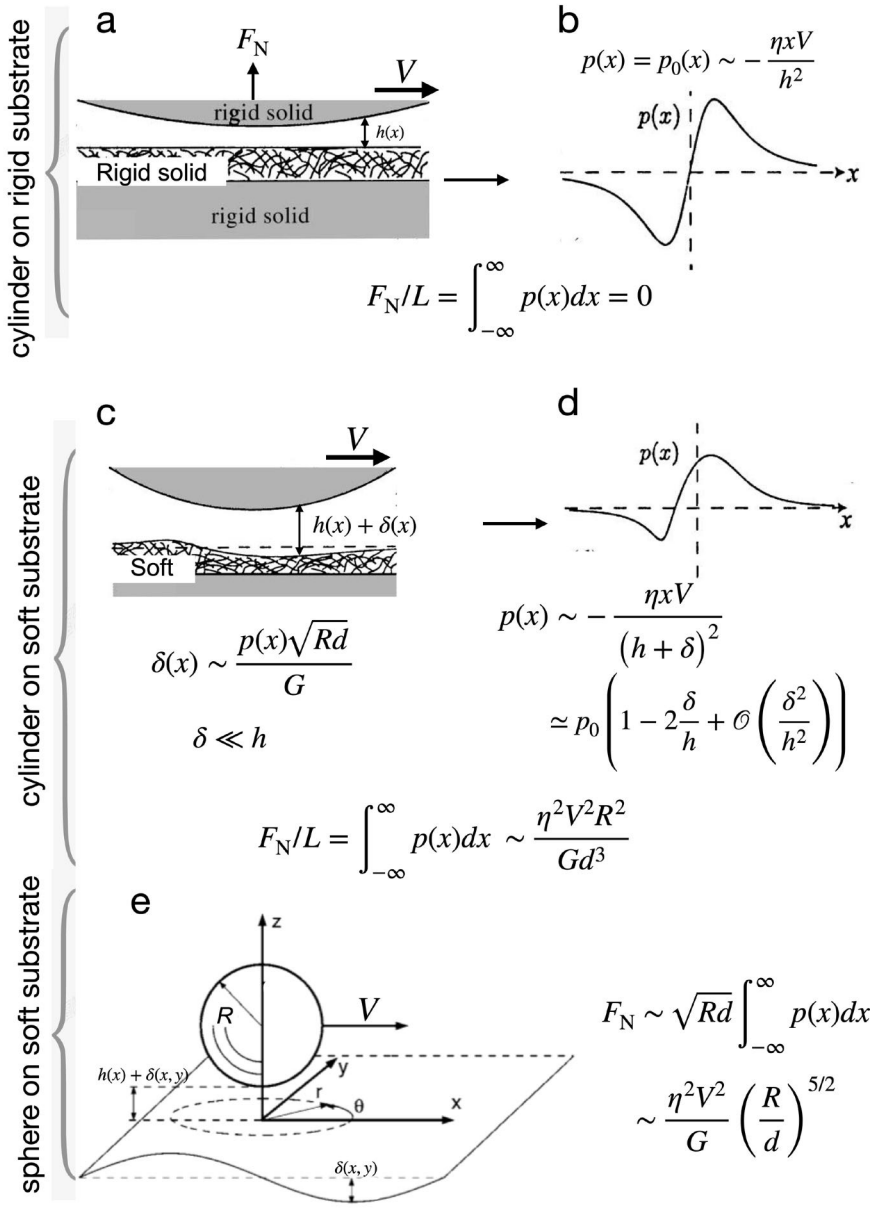

Figure 5.1: *The scaling law for the elastohydrodynamic lift force acting on a spherical particle moving along substrates.* ***a****) A rigid cylinder moves along a rigid substrate laterally at a velocity of* V*.* ***b****) The distribution of the pressure for the cylinder moving along the rigid substrate. The resulting normal force per unit cylinder length is equal to zero.* ***c****) A rigid cylinder moves along a soft substrate laterally at a velocity of* V*. The soft substrate is deformed.* ***d****) The distribution of the pressure for the cylinder moving along a soft substrate. The resulting normal force per unit length is not equal to zero.* ***e****) A rigid spherical particle moves along a soft substrate. The cylinder length is replaced by the hydrodynamic radius, which leads to the expression of the normal force:* $F_N \sim \frac{\eta^2 V^2}{G}\left(\frac{R}{d}\right)^{5/2}$ *[25, 26, 27].*

In this chapter, a direct measurement of the elastohydrodynamic lift force acting on glass spherical particles moving in viscous fluid along soft PDMS samples is presented. Using AFM, the repelling force is probed versus the distance for different velocities, different viscosities and for different Young's moduli of the samples. Our results are in a good agreement with the model developed from the soft lubrication theory.

5.2 Methods

5.2.1 PDMS samples preparation and characterization

Soft substrates were prepared from polydimethylsiloxane (PDMS) (Sylgard 184, Dow Corning). The uncross linked PDMS and the curing agent were thoroughly mixed at mass ratios of $10:1$, $20:1$ and $30:1$ followed by degassing under vacuum. The mixture was spin coated on cover slip of $24\ \mathrm{mm} \times 24\ \mathrm{mm}$, and was cured in the oven at $50\ ^{\circ}\mathrm{C}$ for 24 hours in order to promote an efficient cross-linking. The thickness of the samples was estimated to $25\ \mu\mathrm{m} - 30\ \mu\mathrm{m}$.

For materials characterization, Young's moduli were determined in an additional experiment. Through indentation experiments, the force-indentation data are fitted by Johnson-Kendall-Roberts (JKR) theory [128] to extract the Young's modulus (The JKR theory is suit to the application in the case of large tips and soft samples with large adhesion).

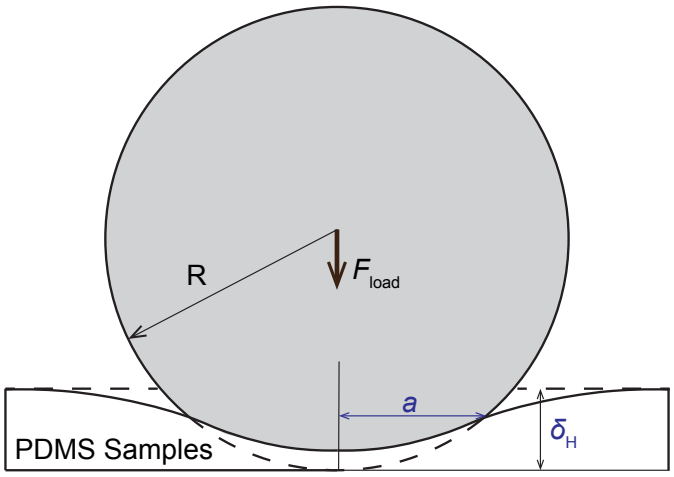

Figure 5.2: *Contact of a sphere with an elastic substrate.*

As shown in Fig. 5.2, the relation between the load force F_{load} and the indentation δ_{H} is modeled by the JKR theory described as:

$$F_{\mathrm{load}} = \frac{a^3}{\pi R} - \sqrt{8\pi a^3 E^* W}, \tag{5.2}$$

$$\delta_{\mathrm{H}} = \frac{a^2}{R} - \sqrt{\frac{2\pi a W}{E^*}}, \tag{5.3}$$

$$a^3 = \frac{3R}{4E^*}\left(F_{\mathrm{load}} + 3\pi W R + \sqrt{6\pi W R F_{\mathrm{load}} + (3\pi W R)^2}\right). \tag{5.4}$$

where F_{load} is the load force acting on the sphere, R is the radius of the spherical probe, δ_{H} is the indentation depth of the sphere in the soft samples, a is the radius of the contact, W is the adhesive work, E^* is the effective modulus with $E^* = E/(1-\nu^2)$, E is the Young's modulus of sample, and ν is the Poisson ratio of the sample. Since cross-linked PDMS samples are incompressible material to a very good approximation, the Poisson ratio is fixed to $\nu = 0.5$[1]. Finally, we obtain

$$\delta_{\mathrm{H}}^3 = \frac{9}{16}\frac{(3\pi W R)^2}{E^{*2} R}\left(1 + \frac{F_{\mathrm{load}}}{3\pi W R} + \sqrt{1 + \frac{2F_{\mathrm{load}}}{3\pi W R}}\right)^2 \left(1 - \frac{2}{3}\sqrt{\frac{2}{1 + \frac{F_{\mathrm{load}}}{3\pi W R} + \sqrt{1 + \frac{2F_{\mathrm{load}}}{3\pi W R}}}}\right)^3. \tag{5.5}$$

In the characterization, a stiff cantilever with a stiffness of $73\ \mathrm{N/m}$ was chosen such that the deflection remains small even at large indentation. A rigid sphere with a diameter of $15\ \mu\mathrm{m}$ was used to characterize the samples. Continuous force-indentation measurements were conducted by AFM in air with approaching velocity equals to $196\ \mathrm{nm/s}$. Figure 5.3 shows an example of the force-indentation measurement which was performed on PDMS (10:1) sample.

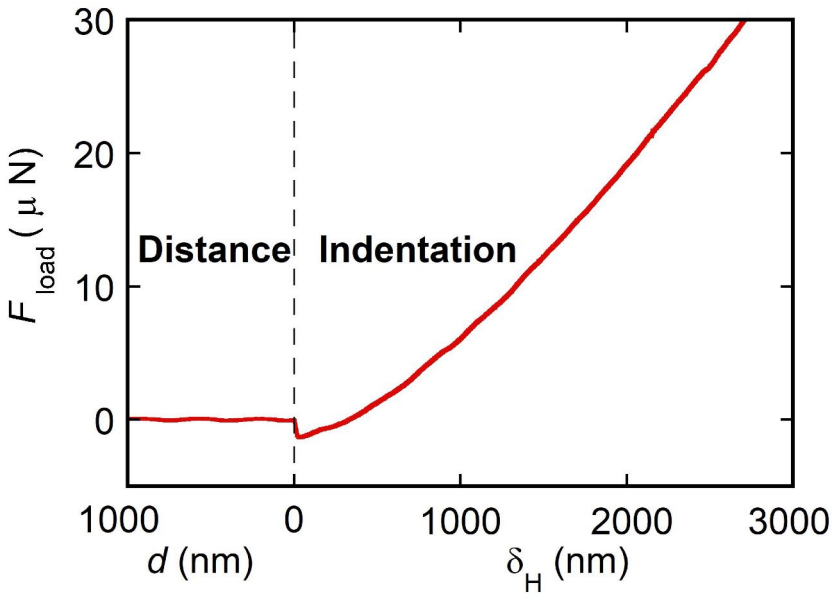

Figure 5.3: *Example of the force-indentation curve obtained by AFM on PDMS* $(10:1)$ *sample.*

[1]The shear modulus G is related to Young's modulus by $G = E/(2(1+\nu))$.

To extract the force-indentation curve from the force-displacement data obtain by AFM, the cantilever deflection sensitivity is first calibrated on a mica surface that is assumed to be infinitely stiff. The indentation is obtained by the relation of $\delta_{\mathrm{H}} = Z_{\mathrm{p}} - Z_{\mathrm{c}}$, where Z_{p} is the sample displacement, and Z_{c} is the cantilever deflection. The contact position between the sphere and the sample is defined as the position where the jump occurs due to the adhesion force.

Figure 5.4 shows the third power of the indentation δ_{H}^3 versus the load force F_{load}. Fitting the curve using Eq. (5.5), and taking E^* and W as two adjustable parameters, the effective moduli E^* of the PDMS samples are extracted as 1940 ± 135 kPa, 800 ± 65 kPa and 390 ± 25 kPa for PDMS (10:1), PDMS (20:1) and PDMS (30:1), respectively. With the relationship of $E^* = E/(1-\nu^2)$, and $\nu = 0.5$, the PDMS samples could be characterized with the Young's moduli of 1455 ± 100 kPa, 600 ± 50 kPa and 293 ± 20 kPa for PDMS (10:1), PDMS (20:1) and PDMS (30:1), respectively.

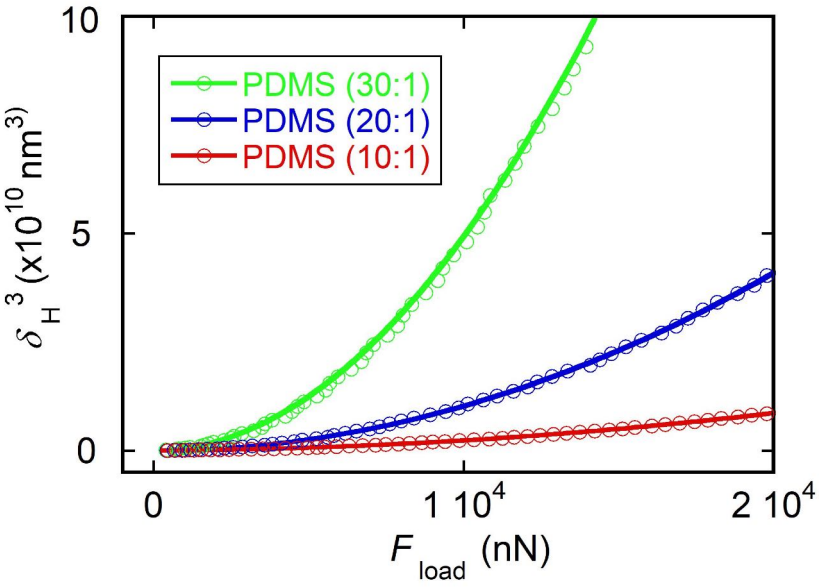

Figure 5.4: *Indentation depth δ_{H} as a function of load force F_{load} for different PDMS samples. The solid lines are the fitting curves by Eq. (5.5), which give us the Young's moduli E of these three PDMS samples of* 1455 ± 100 kPa, 600 ± 50 kPa *and* 293 ± 20 kPa *for PDMS (10:1), PDMS (20:1) and PDMS (30:1), respectively.*

5.2.2 Calibration of the piezo

In this study, the multi-axis piezo-system (NanoT series, Mad City Labs) was used, and this piezo allows to control the gap distance d between the sphere and the sample by displacing the sample vertically and also to vibrate the sample transversally. The former has been calibrated

in Sec. 1.2.3, and the latter calibration will be discussed in this section. With the same driving amplitudes, the larger the driving frequency, the lower oscillation amplitude of the piezo. Since the elastohydrodynamic lift force is scaled with V^2, in order to minimize the error in the measurement, we need to measure the piezo velocity precisely.

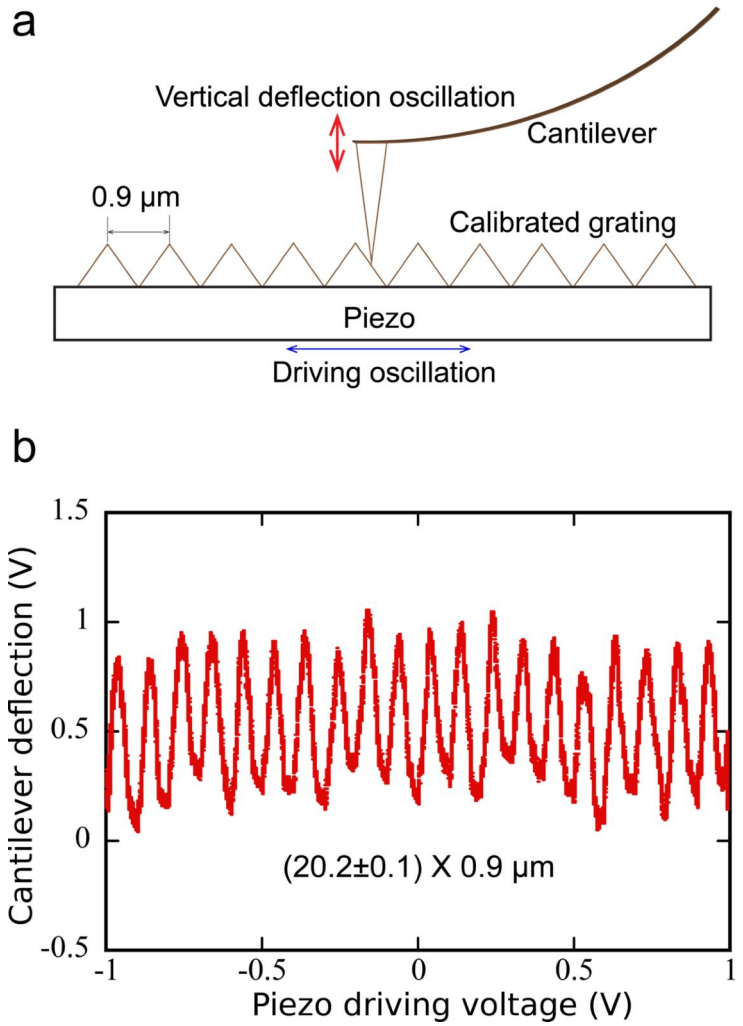

Figure 5.5: ***a****) The schematic of the calibration of the piezo using the grating.* ***b****) The recored cantilever deflection versus driving voltage. The driving frequency of the piezo is* 25 Hz*, and the amplitude is* 1 V.

In this study, we use a calibrated grating to measure the motion of the piezo. As shown in Fig 5.5a, a cantilever with a sharp tip is used to probe the motion of the piezo. A calibrated grating is fixed on the piezo, and the topographic profile of the grating is a triangular pattern, with a periodic length of 0.9 μm. When the cantilever is in contact with the grating, the piezo is driven to oscillate laterally. Both cantilever deflection and driving voltage are recored. Figure 5.5b shows the recorded cantilever deflection as a function of the piezo driving voltage for

the calibration at 25 Hz with an amplitude of 1 V. By counting the the number of peaks in the cantilever deflection signal, the piezo displacement can be obtained by multiplying the peak number with the periodic length. In Fig 5.5b, for the driving voltage of 2 V (peak to peak), we have 20.2 ± 0.1 peaks that corresponding to a piezo displacement of $20.2 \times 0.9\ \mu\text{m} = 18.2\ \mu\text{m}$.

The piezo is calibrated at 25 Hz and 50 Hz with different driving amplitudes. The results are shown in Fig. 5.6. From a linear fitting (the black solid line in Fig. 5.6), we get the displacements per volt of $9.46\ \mu\text{m/V}$ for 25 Hz, and $3.02\ \mu\text{m/V}$ for 50 Hz, respectively.

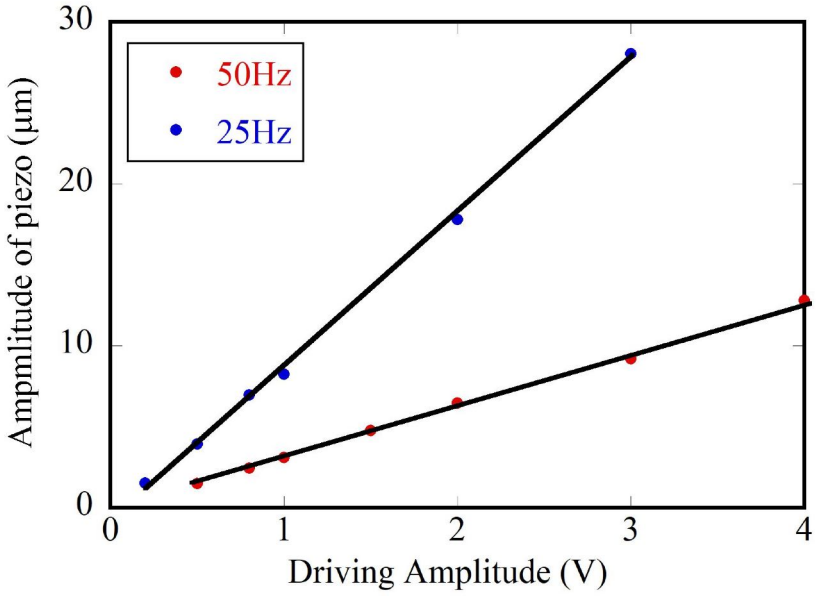

Figure 5.6: *The calibration results at* 25 *Hz and* 50 *Hz. The solid lines are the linear fitting curves for the results. From the fitting, we obtain the displacements per volt of* $9.46\ \mu\text{m/V}$ *for* 25 *Hz, and* $3.02\ \mu\text{m/V}$ *for* 50 *Hz, respectively.*

5.3 Experiment

5.3.1 Experimental Setup

The experimental schematic of the setup is shown in Fig. 5.7. The experiment was performed using an AFM (Bruker, Bioscope) equipped with a liquid cell (DTFML-DD-HE) that allows working in a liquid environment. We used a spherical borosilicate particle (MO-Sci Corporation) with a radius $R = 60\ \mu\text{m}$ and a roughness of 0.9 nm measured over a $1\ \mu\text{m}^2$ surface area. The sphere was glued on the end of a silicon nitride V-shaped cantilever (SNL, Brukerafm-probes) using epoxy glue (Araldite, Bostik, Coubert). The soft samples were fixed on the multi-axis piezo-system (NanoT series, Mad City Labs) to control and scan the gap distance d between the sphere and the sample by displacing the sample vertically, and also to vibrate the sample

transversally at a frequency $f = \omega/2\pi = 25$ Hz or 50 Hz, and with an amplitude A ranging form 3.6 to 36 μm. Note that the vertical displacement speed 20 nm/s being much smaller than the smallest transversal velocity amplitude $A\omega = 0.36$ mm/s, the former can be neglected and a quasi-static description with respect to the normal motion is valid. Using the drainage method shown in Sec. 1.3.3, the stiffness $k_c = 0.21 \pm 0.02$ N/m of the cantilever is determined using a rigid silicon wafer as a substrate and for large enough gap distances ($d = 200 - 20000$ nm). The viscous liquids employed in this study are silicone oil and 1-decanol, with dynamic viscosities $\eta = 96$ mPa $\cdot$ s and 14.1 mPa $\cdot$ s, respectively. In all experiments, the hydrodynamic radius $\sqrt{2Rd}$ being much smaller than the thickness of the soft substrates, *i.e.* $\sqrt{2Rd} \ll 25$ μm, the sample can indeed be considered as semi-infinite.

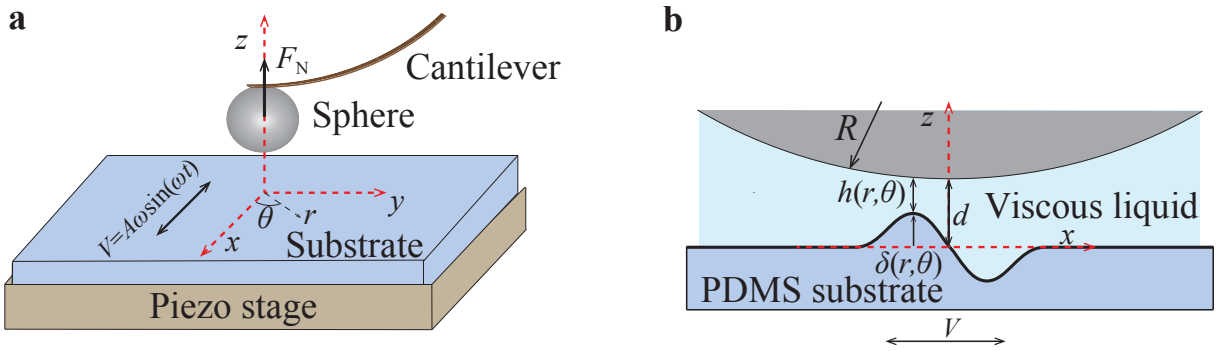

Figure 5.7: *Schematic of the experimental setup. The soft substrate is fixed to a rigid piezo stage that is transversally oscillated along time t, at angular frequency ω, and with amplitude A. A rigid borosilicate sphere is glued to an AFM cantilever and placed near the substrate, with silicone oil or 1-decanol as a viscous liquid lubricant. The normal force F_N exerted on the sphere, at a gap distance d from the surface, is directly measured from the deflection of the cantilever.*

Using scaling arguments, the elastohydrodynamic lift force acting on a sphere immersed in a viscous fluid with a viscosity of η and moving at constant velocity V, near and parallel to a semi-infinite incompressible elastic substrate of shear modulus $G = E/[2(1+\nu)]$, reads [25, 26, 27]

$$F_{\text{lift}} \sim \frac{\eta^2 A^2 \omega^2}{G} \left(\frac{R}{d}\right)^{5/2}. \tag{5.6}$$

in the limit of small dimensionless compliance, $\kappa = \eta V/(Gd^2) \ll 1$. Note that, in this limit, κ corresponds to the ratio between the deformation of substrate and gap distance. To go beyond the scaling analysis, we have developed a model to calculate the missing prefactor in Eq. (5.6). Based on the soft lubrication theory [25, 26], in the case of low Reynolds number[1] and linear

[1]The Reynolds number of the system is equal to $\text{Re} = \rho V\sqrt{2Rd}/\eta$. With the typical values: velocity $V = 2.32$ mm/s, hydrodynamic radius of $\sqrt{2Rd} = 9$ μm and kinetic viscosity $\eta/\rho = 17$ mm^2/s, we get $\text{Re} \approx 10^{-3} \ll 1$

elasticity of the sample, we calculate the elastohydrodynamic lift force as [129]

$$F_{\text{lift}} \simeq 0.416 \frac{\eta^2 A^2 \omega^2}{G} \left(\frac{R}{d}\right)^{5/2}. \tag{5.7}$$

Since the lateral velocity of the samples is sinusoidal and the lift force depends on the squared velocity, Eq. (5.7) can be expressed as two additive components: A time-independent component (DC component) given by

$$0.416 \frac{\eta^2 A^2 \omega^2}{2G} \left(\frac{R}{d}\right)^{5/2}, \tag{5.8}$$

and a component oscillating at double frequency (AC component), given by

$$0.416 \frac{\eta^2 A^2 \omega^2 \cos(2\omega t)}{2G} \left(\frac{R}{d}\right)^{5/2}. \tag{5.9}$$

Focusing only on the DC component, it is measured though a temporal average $F =< F_{\text{N}} >$ of the instantaneous normal force F_{N} recorded by the AFM (see Fig. 5.7a), from which the AC component will disappear in the measurement. Therefore, the temporal average F of F_{lift} over a period $2\pi/\omega$ of oscillation is given by:

$$F \approx 0.416 \frac{\eta^2 A^2 \omega^2}{2G} \left(\frac{R}{d}\right)^{5/2}. \tag{5.10}$$

Introducing parameters of $\kappa = \eta A \omega R/(\sqrt{2} G d^2)$ and $F^* = \eta A \omega R^{3/2}/(2d)^{1/2}$, Eq. (5.10) becomes into the form of

$$\frac{F}{F^*} \approx 0.416 \kappa. \tag{5.11}$$

5.3.2 Results & Disscussion

Figure 5.8 shows the force F as a function of the gap distance d, for rigid (silicon wafer) and soft substrates (PDMS 20:1). The liquid is silicone oil with viscosity of $\eta = 96\ \text{mPa} \cdot \text{s}$. The amplitude of the velocity is $A\omega = 0.57\ \text{mm/s}$.

To determine the gap distance, we take into account the cantilever deflection induced by the normal force. As a remark, in most cases studied here, the typical substrate's deformation, $\sim F/(\pi E^* \sqrt{2Rd})$ [21], remains much smaller than the cantilever's deflection. For the rigid case, no finite force is detected above the current nanoNewton (nN) resolution, at all distances. This is expected, since for such a hard surface (Young's modulus is in the range of 100 GPa), so there is no elastohydrodynamic effect (the deformation of the substrate induced by the flow is negligible). The elastohydrodynamic effects occur at gap distances much smaller than the ones typically probed here [20]. As a remark, the fact that no force -even purely hydrodynamic- is measured in this case is a direct confirmation for the validity of the quasistatic description with

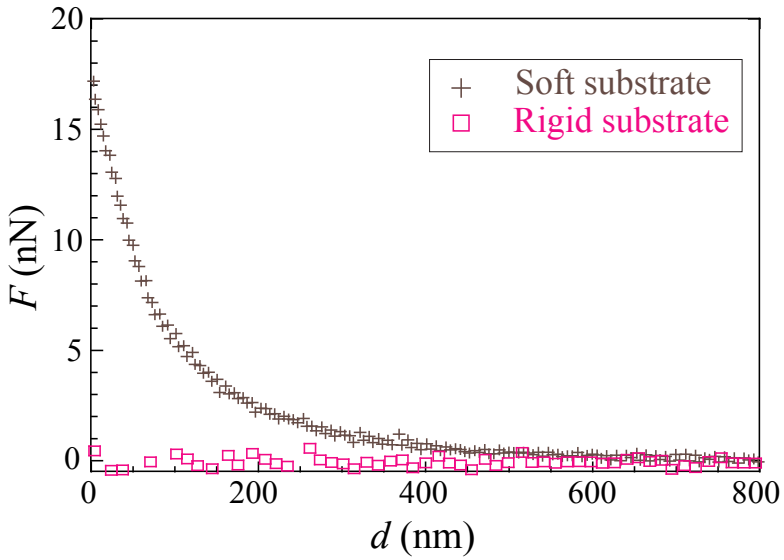

Figure 5.8: *Measured force F averaged from F_{N} (see Fig. 5.7) as a function of the gap distance d to the substrate, for both rigid (silicon wafer) and soft substrates (PDMS 20:1). The liquid is a silicone oil with a viscosity of $\eta = 96\ \mathrm{mPa \cdot s}$. The amplitude of the velocity is $A\omega = 0.57\ \mathrm{mm/s}$.*

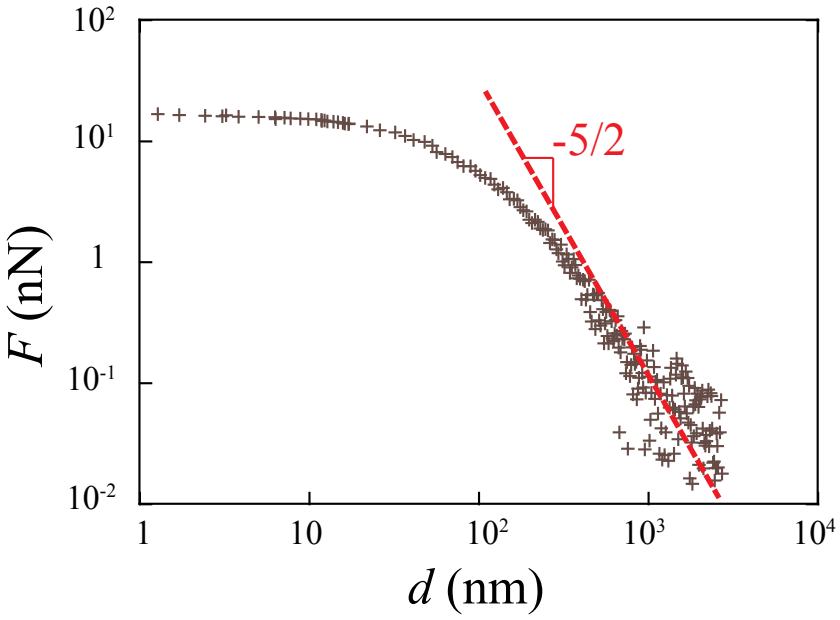

Figure 5.9: *A log-log representation of the data for the soft substrate in Fig. 5.8, and the solid line therein indicates a $-5/2$ power law.*

respect to the imposed vertical displacement of the sphere. In the contrast, for the soft case, a systematic nonzero force is measured, and observed to increase as the gap distance is reduced.

Furthermore, as shown in Fig. 5.9, the measured force F asymptotically scales as $F \sim d^{-5/2}$ at large gap distances, in the agreement with the prediction of Eq. (5.10). Interestingly, at smaller gap distances, a saturation of the lift effect is observed, as reported previously [26, 124].

Having tested the asymptotic dependence of the force with the main geometrical parameter, *i.e.*, the gap distance d, which showed a first evidence of the lift, we now turn to the other key elastohydrodynamic parameters appearing in Eq. (5.10), *i.e.*, the velocity amplitude $A\omega$, viscosity η and shear modulus G. To test the dependences of the force with those three parameters, we use two dimensionless variables as defined above: the dimensionless compliance $\kappa = \eta A\omega R/(\sqrt{2}Gd^2)$ and the dimensionless force F/F^* with $F^* = \eta A\omega R^{3/2}/(2d)^{1/2}$.

Velocity effect

Figure 5.10a shows the force F versus the gap distance d for two different oscillation amplitudes. Figure 5.10b represents the dimensionless force F/F^* as a function of κ for these two oscillation amplitudes. Figure 5.11a shows measured force F for two different oscillation frequencies. Figure 5.11b represents the dimensionless F/F^* as a function of κ for these two oscillation frequencies. Here, the sample is the cross-linked PDMS (10:1), and the liquid is 1-decanol with viscosity of $\eta = 14.1\ \mathrm{mPa \cdot s}$. We can see that the lift force increases as the velocity increases, and the dimensionless forces F/F^* collapse in both figures of 5.10 and 5.11.

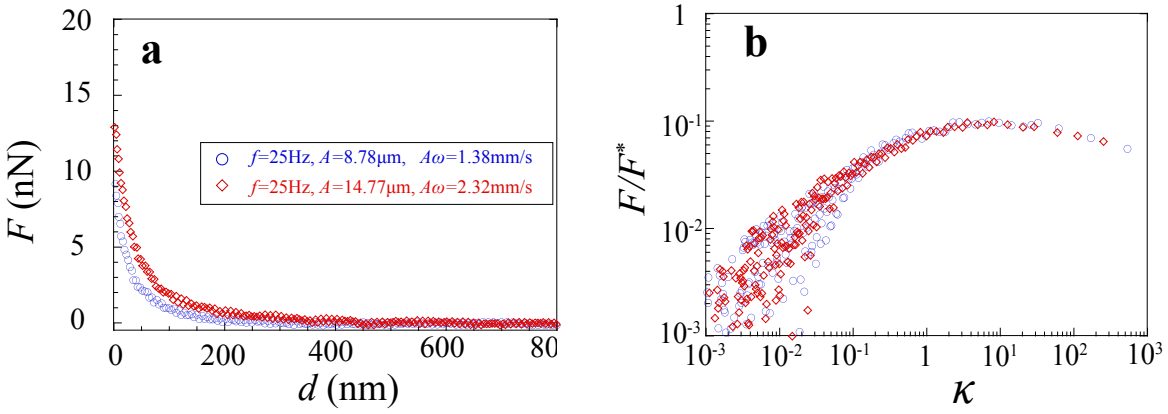

Figure 5.10: ***a)*** *Measured force F versus the gap distance d for two different amplitudes.* ***b)*** *The dimensionless lift force F/F^* as a function of κ for these two amplitudes.*

Viscosity effect

Figure 5.12 shows the results for two different liquids (silicon oil and 1-decanol) with different associated viscosities $\eta = 96\ \mathrm{mPa \cdot s}$ and $\eta = 14.1\ \mathrm{mPa \cdot s}$, respectively. The substrate is the cross-linked PDMS (10:1), and the velocity amplitudes are $A\omega = 0.36\ \mathrm{mm/s}$ for silicone oil and $A\omega = 2.32\ \mathrm{mm/s}$ for 1-decanol. Figure 5.12a shows the measured force F as a function

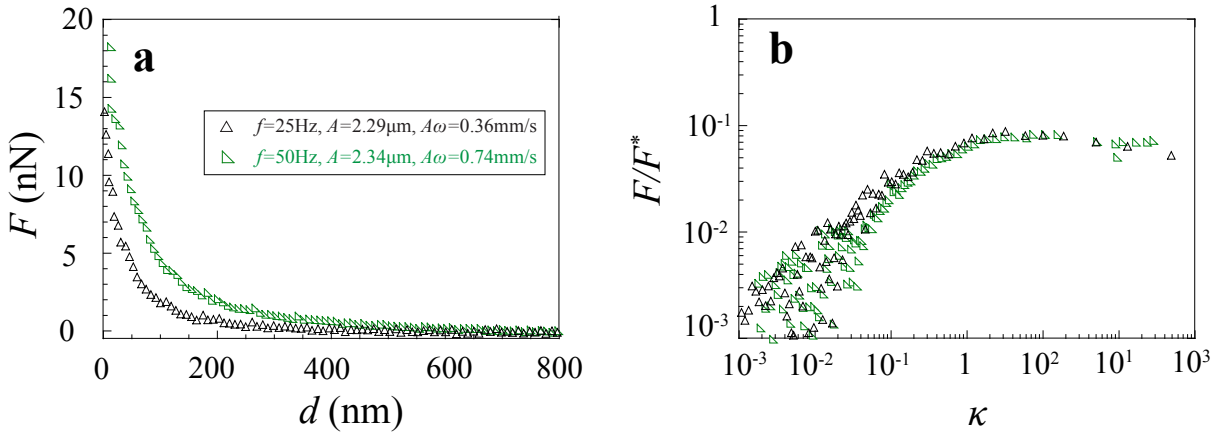

Figure 5.11: ***a)*** *Measured force F versus the gap distance d for two different frequencies.* ***b)*** *The dimensionless lift force F/F^* as a function of κ for these two frequencies.*

of gap distance d, and Figure 5.12b shows the dimensionless force F/F^* as a function of the compliance κ. Note here the values of the velocity multiply with the viscosities in both cases are very close, therefore the measured forces F are quite similar in both cases. In the rescaling presentation (Fig. 5.12b), the results collapse with each other, which means that the lift force has the same dependence on velocity and viscosity.

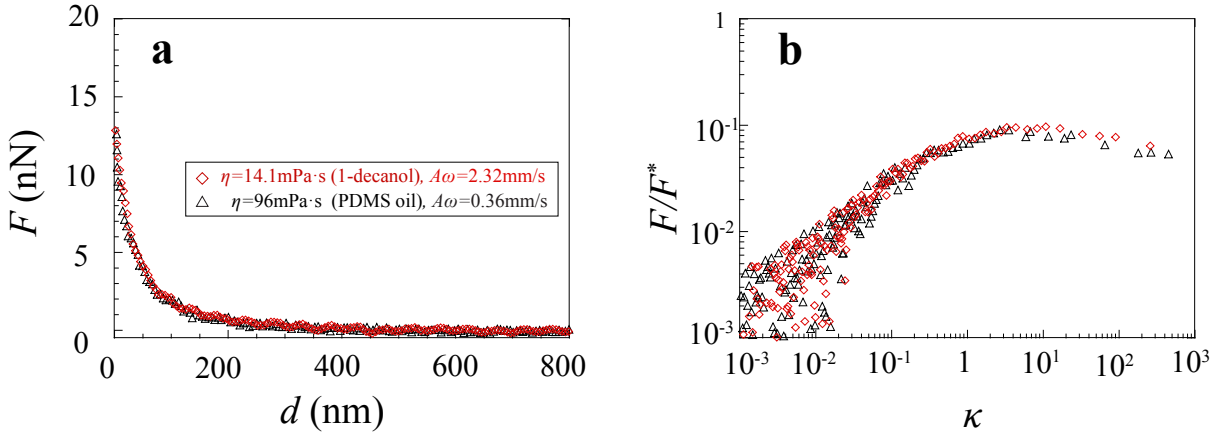

Figure 5.12: ***a)*** *Measured force F versus the gap distance d for two different viscosities.* ***b)*** *The dimensionless lift force F/F^* as a function of κ for these two frequencies.*

Young's modulus effect

Figure 5.13 shows the results for three PDMS samples with shear moduli of $G = 485$ kPa, 200 kPa and 97.5 kPa for the cross-linked PDMS samples (10:1), (20:1) and (30:1), respectively. The liquid is the silicone oil with viscosity $\eta = 96\ \mathrm{mPa \cdot s}$ and the velocity amplitude is

$A\omega = 0.47$ mm/s. As shown in Fig. 5.13a, at large distance, the measured lift force decreases when the hardness of the samples increase, however at small distance, the saturated value of the lift force is large if the hardness of sample is large. In the dimensionless representation of Fig. 5.13b, the dimensionless forces collapse with each other.

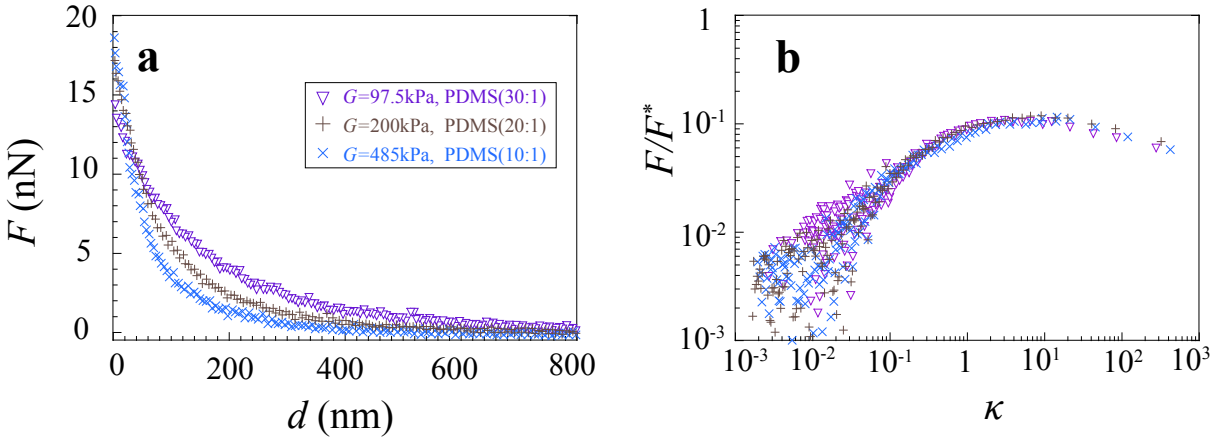

Figure 5.13: ***a)*** *Measured force F versus the gap distance d for three different samples.* ***b)*** *The dimensionless lift force F/F^* as a function of κ for these three samples.*

Discussion

In the dimensionless presentation of lift forces measured for different velocities, different viscosities and different hardness, we first observe at small κ that F/F^* is linear with respect to compliance κ, and that the curves for various values of the varied parameters collapse with one another, which validates further of Eq. (5.11). Moreover, around $\kappa \sim 1$, a deviation from the previous asymptotic behavior is observed leading to a maximum prior to an interesting decay at large κ. In addition, the collapse for various values of the varied parameter is maintained, indicating that even at large dimensionless compliance κ, the dimensionless force F/F^* remains a function of κ only. This suggests that the same physics, coupling lubrication flow and linear elasticity, is at play for all value of compliance κ. In order to test this prediction, we plot F/F^* as a function of κ in Fig. 5.14 for all the experiments performed in this study. First, all the experimental data collapses on a single master curve. Second, Eq. (5.11) is found to be in excellent agreement with the low-κ part of the data, with no adjustable parameter. Finally, the behavior at large κ reveals the possible existence of a power law: $F/F^* \sim \kappa^{-1/4}$. Indeed, at this regime, the deformation of the substrate δ is in the same order of gap distance d, *i.e.* $\delta/d \sim 1$. The other terms in the series expansion of pressure distribution in Fig. 5.1d should be taken into account. For example, the term of $(\delta/h)^2$ should not be neglected in the expression of the lift force, which will reduce the value of life force predicted by Eq. (5.7). Therefore a saturation may occur. The typical deformation $\delta \sim \frac{R\eta V}{Gd}$ leads to the typical distance of $d \sim \sqrt{R\eta V/G}$. By inserting this value to Eq. (5.1), we get $F_{\text{lift}} \sim \eta^{3/4} V^{3/4} G^{1/4} R^{5/4}$, which is equivalent to

$F/F^* \sim \kappa^{-1/4}$. This gap-independent scaling suggests that the lift force saturates at small enough distances (large κ), in agreement with the observation made in Fig. 5.8. Such a result is attributed to a competition between the increase of the elastohydrodynamic symmetry breaking and the decrease of the pressure magnitude due to the substrate's deformation [31].

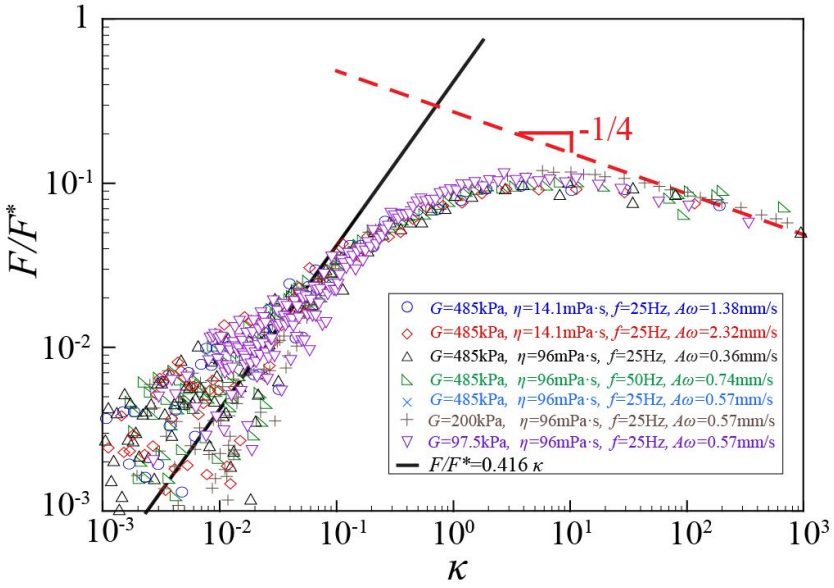

Figure 5.14: *Dimensionless force F/F^* as a function of dimensionless compliance κ in logarithmic scales for all the results measured in this study and the solid line is the model of Eq.*(5.11). *The dashed line indicates the asymptotic behavior of $F/F^* \sim \kappa^{-1/4}$.*

5.4 Conclusion

In this chapter, we have presented an experimental study of the lift force acting on spherical particle moving along thick, soft samples in viscous liquid. As the gap between the sphere and the sample is reduced, a lift force acting on the sphere is observed, and increases with a power law of $-5/2$. Our experiment is the first direct measurement of the elastohydrodynamic lift force at the nanoscale. Moreover, the data for various amplitudes, frequencies, viscosities, and Young's moduli collapse in a master curve. For small compliances, the results are rationalized quantitively based on the classic soft lubrication theory, and for large compliances, or equivalently at small confinement length scales, a saturation of the lift force is observed and a scaling law of $-1/4$ is discussed.

In this chapter, we have presented the measurement of the DC component of lift force on thick samples. For future experiment, we will investigate the behavior of this force versus the thickness of the samples. We will also study the effects of poroelasticity on the lift force, for example, using liquids that swell the samples. Using the Lock-in Amplifier, we will measure

the AC component of the lift force that oscillates at the frequency of 2ω (see Eq. (5.9)). In the latter situation, for high frequencies, the sample deformation is no more pure elastic, but the loss modulus would affect the elastohydrodynamic lift force. A sphere moving along an air bubble is another configuration which is suitable to the study of the lift force that would be induced by the capillary deformation of the air-water interface.

General Conclusion and Perspective

In this thesis, we have used the dynamic colloidal AFM to probe the nano-rheology of the confined flow at soft interfaces made up of air bubbles or PDMS.

The fluid flow between the vertical oscillating sphere and bubble surface generates two effects: the advection of the surfactant impurities and the deformation of the bubble surface. At large distances, where the bubble deformation is negligible, our experimental results demonstrate that very low concentrations of surface impurities drastically modify boundary conditions for water flows near the air-water interfaces. Both viscous and elastic forces are exerted by the interface on the vibrating sphere even when very low doses of contaminants are present. When varying the frequency from low frequencies to high frequencies, a crossover from no-slip to full slip boundary conditions occurs in the viscous drag force. Besides the reduction of the viscous force, the elastic drag force shows a nontrivial variation as the vibration frequency changes. The value of the elastic force is comparable to the viscous force in the intermediate range. Furthermore, our experiment methods allow to detect the impurity concentration at an air-water interface through its viscoelastic response to a vibrating AFM probe.

At intermediate distances ($d \sim 6\pi\eta\omega R^2/\sigma$), the capillary deformation due to the hydrodynamic pressure is at play. To probe the visco-capillary interaction, the cantilever is excited by either thermal excitation or external acoustic excitation. The experimental results obtained with both methods of cantilever excitation are in a qualitative agreement with the simplified model based the spring-dashpot in series. At small distances, a discrepancy is observed between the experimental results and the simplified model. Therefore, the numerical solution of Navier-Stokes equation combined with Young-Laplace equation is calculated. The numerical calculations are in a good agreement with the experimental results and allow us to measure the surface tension of bubble interface without contact.

AFM measurements of the thermal capillary fluctuation of the bubble surfaces are presented in chapter 4. The experimental data demonstrates that the soft AFM cantilevers are a powerful tool to probe the thermal motion of bubble. The cantilever deflection signal reflects the thermal fluctuation of the bubble surface directly. The spectrum of the fluctuations presents sharp resonance peaks for specific frequencies for which the motion of the interface is much more prominent than that for other frequencies. The analysis of these peaks allows to measure the resonance frequencies, effective mass and the damping coefficient for each mode of oscillation. To explain the experimental results, we have presented a model for the bubble shape oscillation. Our measurements are in a good agreement with the model, and allows us to measure the

additional damping due to the presence of minute amounts of contaminants. The experimental results show that the contact line of a hemispherical bubble resting on a solid surface is fixed on the substrate. Moreover, our experimental method provides a useful new tool to probe the surface rheology.

Finally, we have presented an experimental study of the lift force acting on spherical particle moving along thick, soft samples in viscous liquids. As the gap between the sphere and the sample is reduced, a lift force acting on the sphere is observed, and increases with a power law of $-5/2$. Our experiment is the first direct measurement of the elastohydrodynamic lift force at the nanoscale. Moreover, the data for various amplitudes, frequencies, viscosities, and Young's moduli collapse in a master curve. For small compliances, the results are rationalized quantitively based on the soft lubrication theory, and for large compliances, or equivalently at small confinement length scales, a saturation of the lift force is observed and a scaling law of $-1/4$ is discussed.

All these measurements demonstrate that the dynamic colloidal AFM is a well-established and powerful tool to probe the surface properties in a confined geometry.

As a perspective of our investigation of the thermal capillary oscillation of the bubble shape, we can use such method to probe the variation of the surface viscosity versus the concentration of surfactants. In fact, by adding a small amount of the surfactant, the contribution of the dilatation elasticity is very small, and any variation of the damping versus the concentration would be attributed to a variation of the shear viscosity. For higher concentration of the surfactant, the contribution of the dilatation elasticity should be taken into account. We also project to study the dynamic friction of the contact line on the substrate. We expect that adding surfactant to water will modify the boundary conditions of the bubble contact line, i.e. the contact line will not be fixed on the substrate, which may induce additional damping that will be observed from the spectrum of the bubble shape oscillation.

As the outlook for the work concerning the measurements of elastohydrodynamic lift force we project to measure the in-phase and out-of-phase components of the force versus the driving frequency. We will use the Lock-in-Amplifier to measure the amplitude and phase oscillations of the cantilever at 2ω. We expect to answer the following questions:

- How does the lift force behave at high frequencies where both rheological properties, elastic and loss moduli of the PDMS have the same magnitude?

- How does the non-stationary effect contribute to the saturation of the lift force at high frequencies?

We project also to use air bubble as surface to probe the lift force. Indeed, at small distance the hydrodynamic pressure induced by the lateral oscillating sphere is so large that the bubble surface will be deformed which leads to elastohydrodynamic coupling. Beside the study of the lift force versus the frequency and versus the surface tension of the interface, we can also investigate the contribution of the advection of surfactants and surface charges to the lift force.

From applied research perspectives, once the experimental setup used to probe the visco-capillary interaction (vertical oscillations) is improved, it can be a powerful tool for tensiometry of air-water interfaces. This setup allows to measures the surfaces tension of the interfaces without contact (no-invasive) and also it requires a very small volume of probed liquid (tens of microliters).

Bibliography

[1] Lydéric Bocquet and Elisabeth Charlaix. Nanofluidics, from bulk to interfaces. *Chemical Society Reviews*, 39(3):1073–1095, 2010.

[2] Jacob N Israelachvili. *Intermolecular and surface forces*. Academic press, 2011.

[3] Howard A Stone, Abraham D Stroock, and Armand Ajdari. Engineering flows in small devices: microfluidics toward a lab-on-a-chip. *Annu. Rev. Fluid Mech.*, 36:381–411, 2004.

[4] David M Huang, Christian Sendner, Dominik Horinek, Roland R Netz, and Lydéric Bocquet. Water slippage versus contact angle: A quasiuniversal relationship. *Physical review letters*, 101(22):226101, 2008.

[5] Christian Sendner, Dominik Horinek, Lyderic Bocquet, and Roland R Netz. Interfacial water at hydrophobic and hydrophilic surfaces: Slip, viscosity, and diffusion. *Langmuir*, 25(18):10768–10781, 2009.

[6] C Cottin-Bizonne, B Cross, A Steinberger, and E Charlaix. Boundary slip on smooth hydrophobic surfaces: Intrinsic effects and possible artifacts. *Physical review letters*, 94(5):056102, 2005.

[7] Abdelhamid Maali, Touria Cohen-Bouhacina, and Hamid Kellay. Measurement of the slip length of water flow on graphite surface. *Applied Physics Letters*, 92(5):053101, 2008.

[8] Pierre-Gilles de Gennes. On fluid/wall slippage. *Langmuir*, 18(9):3413–3414, 2002.

[9] Yingxi Zhu and Steve Granick. Rate-dependent slip of newtonian liquid at smooth surfaces. *Phys. Rev. Lett.*, 87:096105, 2001.

[10] Christophe Ybert, Catherine Barentin, Cécile Cottin-Bizonne, Pierre Joseph, and Lydéric Bocquet. Achieving large slip with superhydrophobic surfaces: Scaling laws for generic geometries. *Physics of Fluids*, 19(12):123601, 2007.

[11] Derek C Tretheway and Carl D Meinhart. A generating mechanism for apparent fluid slip in hydrophobic microchannels. *Physics of Fluids*, 16(5):1509–1515, 2004.

[12] Ofer Manor, Ivan U. Vakarelski, Xiaosong Tang, Sean J. O'Shea, Geoffrey W. Stevens, Franz Grieser, Raymond R. Dagastine, and Derek Y. C. Chan. Hydrodynamic boundary conditions and dynamic forces between bubbles and surfaces. *Phys. Rev. Lett.*, 101:024501, Jul 2008.

[13] Ofer Manor, Ivan U. Vakarelski, Geoffrey W. Stevens, Franz Grieser, Raymond R. Dagastine, and Derek Y. C. Chan. Dynamic forces between bubbles and surfaces and hydrodynamic boundary conditions. *Langmuir*, 24(20):11533–11543, 2008.

[14] Ofer Manor and Derek Y. C. Chan. Influence of surfactants on the force between two bubbles. *Langmuir*, 26(2):655–662, 2010.

[15] J Lucassen and Robert S Hansen. Damping of waves on monolayer-covered surfaces: I. systems with negligible surface dilational viscosity. *Journal of Colloid and Interface Science*, 22(1):32–44, 1966.

[16] JC Earnshaw. Surface viscosity of water. *Nature*, 292(5819):138–139, 1981.

[17] Jordan T Petkov, Krassimir D Danov, Nikolai D Denkov, Richard Aust, and Franz Durst. Precise method for measuring the shear surface viscosity of surfactant monolayers. *Langmuir*, 12(11):2650–2653, 1996.

[18] C Barentin, P Muller, C Ybert, J-F Joanny, and J-M Di Meglio. Shear viscosity of polymer and surfactant monolayers. *The European Physical Journal E*, 2(2):153–159, 2000.

[19] P Dhar, Th M Fischer, Y Wang, Thomas E Mallouk, WF Paxton, and Ayusman Sen. Autonomously moving nanorods at a viscous interface. *Nano letters*, 6(1):66–72, 2006.

[20] Richard Villey, Emmanuelle Martinot, Cécile Cottin-Bizonne, Magali Phaner-Goutorbe, Liliane Léger, Frédéric Restagno, and Elisabeth Charlaix. Effect of surface elasticity on the rheology of nanometric liquids. *Physical review letters*, 111(21):215701, 2013.

[21] Samuel Leroy and Elisabeth Charlaix. Hydrodynamic interactions for the measurement of thin film elastic properties. *Journal of Fluid Mechanics*, 674:389, 2011.

[22] Samuel Leroy, Audrey Steinberger, Cécile Cottin-Bizonne, Frédéric Restagno, Liliane Léger, and Elisabeth Charlaix. Hydrodynamic interaction between a spherical particle and an elastic surface: a gentle probe for soft thin films. *Physical review letters*, 108(26):264501, 2012.

[23] Dongshi Guan, Chloé Barraud, Elisabeth Charlaix, and Penger Tong. Noncontact viscoelastic measurement of polymer thin films in a liquid medium using long-needle atomic force microscopy. *Langmuir*, 33(6):1385–1390, 2017.

[24] Dongshi Guan, Elisabeth Charlaix, Robert Z Qi, and Penger Tong. Noncontact viscoelastic imaging of living cells using a long-needle atomic force microscope with dual-frequency modulation. *Physical Review Applied*, 8(4):044010, 2017.

[25] JM Skotheim and Laksminarayanan Mahadevan. Soft lubrication. *Physical review letters*, 92(24):245509, 2004.

[26] JM Skotheim and L Mahadevan. Soft lubrication: The elastohydrodynamics of nonconforming and conforming contacts. *Physics of Fluids*, 17(9):092101, 2005.

[27] Javier Urzay, Stefan G Llewellyn Smith, and Beverley J Glover. The elastohydrodynamic force on a sphere near a soft wall. *Physics of Fluids*, 19(10):103106, 2007.

[28] Javier Urzay. Asymptotic theory of the elastohydrodynamic adhesion and gliding motion of a solid particle over soft and sticky substrates at low reynolds numbers. *Journal of fluid mechanics*, 653:391–429, 2010.

[29] Jacobus Hendrikus Snoeijer, J Eggers, and Cornelis H Venner. Similarity theory of lubricated hertzian contacts. *Physics of fluids*, 25(10):101705, 2013.

[30] Thomas Salez and Lakshminarayanan Mahadevan. Elastohydrodynamics of a sliding, spinning and sedimenting cylinder near a soft wall. *Journal of Fluid Mechanics*, 779:181–196, 2015.

[31] Anupam Pandey, Stefan Karpitschka, Cornelis H Venner, and Jacco H Snoeijer. Lubrication of soft viscoelastic solids. *Journal of fluid mechanics*, 799:433–447, 2016.

[32] J Beaucourt, T Biben, and C Misbah. Optimal lift force on vesicles near a compressible substrate. *EPL (Europhysics Letters)*, 67(4):676, 2004.

[33] Manouk Abkarian, Colette Lartigue, and Annie Viallat. Tank treading and unbinding of deformable vesicles in shear flow: determination of the lift force. *Physical review letters*, 88(6):068103, 2002.

[34] Abdallah Daddi-Moussa-Ider, Maciej Lisicki, and Stephan Gekle. Mobility of an axisymmetric particle near an elastic interface. *Journal of Fluid Mechanics*, 811:210–233, 2017.

[35] Abdallah Daddi-Moussa-Ider, Bhargav Rallabandi, Stephan Gekle, and Howard A Stone. Reciprocal theorem for the prediction of the normal force induced on a particle translating parallel to an elastic membrane. *Physical Review Fluids*, 3(8):084101, 2018.

[36] Yumo Wang, Georgia A Pilkington, Charles Dhong, and Joelle Frechette. Elastic deformation during dynamic force measurements in viscous fluids. *Current opinion in colloid & interface science*, 27:43–49, 2017.

[37] Pratyaksh Karan, Jeevanjyoti Chakraborty, and Suman Chakraborty. Small-scale flow with deformable boundaries. *Journal of the Indian Institute of Science*, 98(2):159–183, 2018.

[38] Gerd Binnig, Calvin F Quate, and Ch Gerber. Atomic force microscope. *Physical review letters*, 56(9):930, 1986.

[39] Gerd Binnig, Heinrich Rohrer, Ch Gerber, and Eddie Weibel. Tunneling through a controllable vacuum gap. *Applied Physics Letters*, 40(2):178–180, 1982.

[40] TR Albrecht, Pr Grütter, D Horne, and Do Rugar. Frequency modulation detection using high-q cantilevers for enhanced force microscope sensitivity. *Journal of applied physics*, 69(2):668–673, 1991.

[41] Ricardo García and Rubén Pérez. Dynamic atomic force microscopy methods. *Surface Science Reports*, 47(6):197 – 301, 2002.

[42] JI Kilpatrick, A Gannepalli, JP Cleveland, and SP Jarvis. Frequency modulation atomic force microscopy in ambient environments utilizing robust feedback tuning. *Review of Scientific Instruments*, 80(2):023701, 2009.

[43] William A Ducker, Tim J. Senden, and Richard Mark Pashley. Direct measurement of colloidal forces using an atomic force microscope. *Nature*, 353:239–241, 1991.

[44] William A. Ducker, Tim J. Senden, and Richard M. Pashley. Measurement of forces in liquids using a force microscope. *Langmuir*, 8(7):1831–1836, 1992.

[45] Hans-Jürgen Butt. Measuring electrostatic, van der waals, and hydration forces in electrolyte solutions with an atomic force microscope. *Biophysical journal*, 60(6):1438–1444, 1991.

[46] Michael Kappl and Hans-Jürgen Butt. The colloidal probe technique and its application to adhesion force measurements. *Particle & Particle Systems Characterization*, 19(3):129–143, 2002.

[47] Hans-Jürgen Butt, Brunero Cappella, and Michael Kappl. Force measurements with the atomic force microscope: Technique, interpretation and applications. *Surface Science Reports*, 59(1):1 – 152, 2005.

[48] E Riis, H Simonsen, Torben Worm, U Nielsen, and Flemming Besenbacher. Calibration of the electrical response of piezoelectric elements at low voltage using laser interferometry. *Applied physics letters*, 54(25):2530–2531, 1989.

[49] S Pal and S Banerjee. A simple technique for height calibration for z piezo with angstrom resolution of scanning probe microscopes. *Review of Scientific Instruments*, 71(2):589–590, 2000.

[50] Dario Alliata, Ciro Cecconi, and Claudio Nicolini. A simple method for preparing calibration standards for the three working axes of scanning probe microscope piezo scanners. *Review of scientific instruments*, 67(3):748–751, 1996.

[51] S Vieira. The behavior and calibration of some piezoelectric ceramics used in the stm. *IBM journal of research and development*, 30(5):553–556, 1986.

[52] Andres Castellanos-Gomez, Carlos R Arroyo, Nicolás Agraït, and Gabino Rubio-Bollinger. Calibration of piezoelectric positioning actuators using a reference voltage-to-displacement transducer based on quartz tuning forks. *Microscopy and Microanalysis*, 18(2):353–358, 2012.

[53] H-J Butt and Manfred Jaschke. Calculation of thermal noise in atomic force microscopy. *Nanotechnology*, 6(1):1, 1995.

[54] BD Hauer, C Doolin, KSD Beach, and JP Davis. A general procedure for thermomechanical calibration of nano/micro-mechanical resonators. *Annals of Physics*, 339:181–207, 2013.

[55] U Rabe and W Arnold. Acoustic microscopy by atomic force microscopy. *Applied Physics Letters*, 64(12):1493–1495, 1994.

[56] TR Albrecht, S Akamine, TE Carver, and CF Quate. Microfabrication of cantilever styli for the atomic force microscope. *Journal of Vacuum Science & Technology A: Vacuum, Surfaces, and Films*, 8(4):3386–3396, 1990.

[57] John Elie Sader and Lee White. Theoretical analysis of the static deflection of plates for atomic force microscope applications. *Journal of Applied physics*, 74(1):1–9, 1993.

[58] Jonas M Neumeister and William A Ducker. Lateral, normal, and longitudinal spring constants of atomic force microscopy cantilevers. *Review of Scientific Instruments*, 65(8):2527–2531, 1994.

[59] Jeffrey L. Hutter and John Bechhoefer. Calibration of atomic-force microscope tips. *Rev. Sci. Instrum.*, 64(7):1868–1873, 1993.

[60] Vincent S. J. Craig and Chiara Neto. In situ calibration of colloid probe cantilevers in force microscopy: Hydrodynamic drag on a sphere approaching a wall. *Langmuir*, 17(19):6018–6022, 2001.

[61] Olga I. Vinogradova. Drainage of a thin liquid film confined between hydrophobic surfaces. *Langmuir*, 11(6):2213–2220, 1995.

[62] Christopher DF Honig and William A Ducker. No-slip hydrodynamic boundary condition for hydrophilic particles. *Physical review letters*, 98(2):028305, 2007.

[63] Olga I Vinogradova. Implications of hydrophobic slippage for the dynamic measurements of hydrophobic forces. *Langmuir*, 14(10):2827–2837, 1998.

[64] Eric Lauga, Michael P Brenner, and Howard A Stone. *Microfluidics: the no-slip boundary condition. Springer handbook of experimental fluid mechanics*. Springer, 2007.

[65] Chiara Neto, Drew R Evans, Elmar Bonaccurso, Hans-Jürgen Butt, and Vincent SJ Craig. Boundary slip in newtonian liquids: a review of experimental studies. *Reports on progress in physics*, 68(12):2859, 2005.

[66] Ivan U Vakarelski, Judy Lee, Raymond R Dagastine, Derek YC Chan, Geoffrey W Stevens, and Franz Grieser. Bubble colloidal afm probes formed from ultrasonically generated bubbles. *Langmuir*, 24(3):603–605, 2008.

[67] Ivan U Vakarelski, Rogerio Manica, Xiaosong Tang, Sean J O'Shea, Geoffrey W Stevens, Franz Grieser, Raymond R Dagastine, and Derek YC Chan. Dynamic interactions between microbubbles in water. *Proceedings of the National Academy of Sciences*, 107(25):11177–11182, 2010.

[68] Derek YC Chan, Evert Klaseboer, and Rogerio Manica. Film drainage and coalescence between deformable drops and bubbles. *Soft Matter*, 7(6):2235–2264, 2011.

[69] Rico F Tabor, Franz Grieser, Raymond R Dagastine, and Derek YC Chan. Measurement and analysis of forces in bubble and droplet systems using afm. *Journal of colloid and interface science*, 371(1):1–14, 2012.

[70] Raymond R Dagastine, Rogério Manica, Steven L Carnie, DYC Chan, Geoffrey W Stevens, and Franz Grieser. Dynamic forces between two deformable oil droplets in water. *Science*, 313(5784):210–213, 2006.

[71] Stefan Ecke, Markus Preuss, and Hans-Jürgen Butt. Microsphere tensiometry to measure advancing and receding contact angles on individual particles. *Journal of adhesion science and technology*, 13(10):1181–1191, 1999.

[72] Xiaomin Xiong, Shuo Guo, Zuli Xu, Ping Sheng, and Penger Tong. Development of an atomic-force-microscope-based hanging-fiber rheometer for interfacial microrheology. *Physical Review E*, 80(6):061604, 2009.

[73] Mathieu Delmas, Marc Monthioux, and Thierry Ondarçuhu. Contact angle hysteresis at the nanometer scale. *Physical review letters*, 106(13):136102, 2011.

[74] Shuo Guo, Min Gao, Xiaomin Xiong, Yong Jian Wang, Xiaoping Wang, Ping Sheng, and Penger Tong. Direct measurement of friction of a fluctuating contact line. *Physical review letters*, 111(2):026101, 2013.

[75] Julien Dupré de Baubigny, Michael Benzaquen, Laure Fabié, Mathieu Delmas, Jean-Pierre Aimé, Marc Legros, and Thierry Ondarçuhu. Shape and effective spring constant of liquid interfaces probed at the nanometer scale: Finite size effects. *Langmuir*, 31(36):9790–9798, 2015.

[76] Caroline Mortagne, Kevin Lippera, Philippe Tordjeman, Michael Benzaquen, and Thierry Ondarçuhu. Dynamics of anchored oscillating nanomenisci. *Physical Review Fluids*, 2(10):102201, 2017.

[77] Abdelhamid Maali, Rodolphe Boisgard, Hamza Chraibi, Zaicheng Zhang, Hamid Kellay, and Aloïs Würger. Viscoelastic drag forces and crossover from no-slip to slip boundary conditions for flow near air-water interfaces. *Physical Review Letters*, 118(8):084501, 2017.

[78] Cédric Jai, Touria Cohen-Bouhacina, and Abdelhamid Maali. Analytical description of the motion of an acoustic-driven atomic force microscope cantilever in liquid. *Applied physics letters*, 90(11):113512, 2007.

[79] Daniel Kiracofe and Arvind Raman. Quantitative force and dissipation measurements in liquids using piezo-excited atomic force microscopy: a unifying theory. *Nanotechnology*, 22(48):485502, 2011.

[80] Yuliang Wang, Binglin Zeng, Hadush Tedros Alem, Zaicheng Zhang, Elisabeth Charlaix, and Abdelhamid Maali. Viscocapillary response of gas bubbles probed by thermal noise atomic force measurement. *Langmuir*, 34(4):1371–1375, 2018.

[81] Pierre-Gilles De Gennes, Françoise Brochard-Wyart, and David Quéré. *Capillarity and wetting phenomena: drops, bubbles, pearls, waves*. Springer Science & Business Media, 2013.

[82] John Shipley Rowlinson and Benjamin Widom. *Molecular theory of capillarity*. Courier Corporation, 2013.

[83] LA Turski and JS Langer. Dynamics of a diffuse liquid-vapor interface. *Physical Review A*, 22(5):2189, 1980.

[84] Michele Sferrazza, C Xiao, Richard Anthony Lewis Jones, David G Bucknall, J Webster, and J Penfold. Evidence for capillary waves at immiscible polymer/polymer interfaces. *Physical review letters*, 78(19):3693, 1997.

[85] J Meunier. Liquid interfaces: role of the fluctuations and analysis of ellipsometry and reflectivity measurements. *Journal de Physique*, 48(10):1819–1831, 1987.

[86] Hyunjung Kim, A Rühm, LB Lurio, JK Basu, J Lal, D Lumma, SGJ Mochrie, and SK Sinha. Surface dynamics of polymer films. *Physical review letters*, 90(6):068302, 2003.

[87] Y Hennequin, DGAL Aarts, JH van der Wiel, G Wegdam, J Eggers, HNW Lekkerkerker, and Daniel Bonn. Drop formation by thermal fluctuations at an ultralow surface tension. *Physical review letters*, 97(24):244502, 2006.

[88] Didi Derks, Dirk GAL Aarts, Daniel Bonn, Henk NW Lekkerkerker, and Arnout Imhof. Suppression of thermally excited capillary waves by shear flow. *Physical review letters*, 97(3):038301, 2006.

[89] Masafumi Fukuto, Oleg Gang, Kyle J Alvine, and Peter S Pershan. Capillary wave fluctuations and intrinsic widths of coupled fluid-fluid interfaces: An x-ray scattering study of a wetting film on bulk liquid. *Physical Review E*, 74(3):031607, 2006.

[90] AM Willis and JB Freund. Thermal capillary waves relaxing on atomically thin liquid films. *Physics of fluids*, 22(2):022002, 2010.

[91] Dirk GAL Aarts, Matthias Schmidt, and Henk NW Lekkerkerker. Direct visual observation of thermal capillary waves. *Science*, 304(5672):847–850, 2004.

[92] Guillaume Michel, François Pétrélis, and Stéphan Fauve. Observation of thermal equilibrium in capillary wave turbulence. *Physical Review Letters*, 118(14):144502, 2017.

[93] BM Ocko, XZ Wu, EB Sirota, SK Sinha, and M Deutsch. X-ray reflectivity study of thermal capillary waves on liquid surfaces. *Physical review letters*, 72(2):242, 1994.

[94] DMA Buzza. General theory for capillary waves and surface light scattering. *Langmuir*, 18(22):8418–8435, 2002.

[95] SK Peace, RW Richards, and N Williams. Surface quasi-elastic light scattering from an amphiphilic graft copolymer at the air- water interface. *Langmuir*, 14(3):667–678, 1998.

[96] Shai Maayani, Leopoldo L Martin, Samuel Kaminski, and Tal Carmon. Cavity optocapillaries. *Optica*, 3(5):552–555, 2016.

[97] Laura Cantu, Antonio Raudino, and Mario Corti. An interferometric technique to study capillary waves. *Advances in colloid and interface science*, 247:23–32, 2017.

[98] Guido Bolognesi, Yuki Saito, Arwen II Tyler, Andrew D Ward, Colin D Bain, and Oscar Ces. Mechanical characterization of ultralow interfacial tension oil-in-water droplets by thermal capillary wave analysis in a microfluidic device. *Langmuir*, 32(15):3580–3586, 2016.

[99] John W Miles. Surface-wave damping in closed basins. *Proceedings of the Royal Society of London. Series A. Mathematical and Physical Sciences*, 297(1451):459–475, 1967.

[100] C Stenvot and D Langevin. Study of viscoelasticity of soluble monolayers using analysis of propagation of excited capillary waves. *Langmuir*, 4(5):1179–1183, 1988.

[101] Scott Thomas Milner. Square patterns and secondary instabilities in driven capillary waves. *Journal of fluid mechanics*, 225:81–100, 1991.

[102] Hui-Lan Lu and Robert E Apfel. Shape oscillations of drops in the presence of surfactants. *Journal of fluid mechanics*, 222:351–368, 1991.

[103] T Chou, SK Lucas, and Howard A Stone. Capillary wave scattering from a surfactant domain. *Physics of Fluids*, 7(8):1872–1885, 1995.

[104] TJ Asaki, DB Thiessen, and PL Marston. Effect of an insoluble surfactant on capillary oscillations of bubbles in water: Observation of a maximum in the damping. *Physical review letters*, 75(14):2686, 1995.

[105] Catherine Barentin, Christophe Ybert, Jean-Marc Di Meglio, and Jean-François Joanny. Surface shear viscosity of gibbs and langmuir monolayers. *Journal of Fluid Mechanics*, 397:331–349, 1999.

[106] Joanna Giermanska-Kahn, Francisco Monroy, and Dominique Langevin. Negative effective surface viscosities in insoluble fatty acid monolayers: Effect of phase transitions on dilational viscoelasticity. *Physical Review E*, 60(6):7163, 1999.

[107] Zachary A Zell, Arash Nowbahar, Vincent Mansard, L Gary Leal, Suraj S Deshmukh, Jodi M Mecca, Christopher J Tucker, and Todd M Squires. Surface shear inviscidity of soluble surfactants. *Proceedings of the National Academy of Sciences*, 111(10):3677–3682, 2014.

[108] Girish K Rajan and Diane M Henderson. Linear waves at a surfactant-contaminated interface separating two fluids: Dispersion and dissipation of capillary-gravity waves. *Physics of Fluids*, 30(7):072104, 2018.

[109] Andrea Prosperetti. Linear oscillations of constrained drops, bubbles, and plane liquid surfaces. *Physics of fluids*, 24(3):032109, 2012.

[110] Lord Rayleigh. On the capillary phenomena of jets. *Proc. R. Soc. London*, 29(196-199):71–97, 1879.

[111] LD Landau and EM Lifshitz. *Fluid Mechanics*, volume 6. 1959.

[112] Andrea Prosperetti. Free oscillations of drops and bubbles: the initial-value problem. *Journal of Fluid Mechanics*, 100(2):333–347, 1980.

[113] R Levy and M Maaloum. Measuring the spring constant of atomic force microscope cantilevers: thermal fluctuations and other methods. *Nanotechnology*, 13(1):33, 2001.

[114] Lars-Oliver Heim, Tiago S Rodrigues, and Elmar Bonaccurso. Direct thermal noise calibration of colloidal probe cantilevers. *Colloids and Surfaces A: Physicochemical and Engineering Aspects*, 443:377–383, 2014.

[115] HORACE Lamb. *Hydrodynamics*. Cambridge: Cambridge University Press, 1916.

[116] Françoise Brochard-Wyart. Hydrodynamics at soft surfaces: from rubber tyres to living cells. *Comptes Rendus Physique*, 4(2):207 – 210, 2003.

[117] Yumo Wang, Charles Dhong, and Joelle Frechette. Out-of-contact elastohydrodynamic deformation due to lubrication forces. *Physical review letters*, 115(24):248302, 2015.

[118] Derek YC Chan, Evert Klaseboer, and Rogerio Manica. Dynamic deformations and forces in soft matter. *Soft Matter*, 5(15):2858–2861, 2009.

[119] Denis Wirtz. Particle-tracking microrheology of living cells: principles and applications. *Annual review of biophysics*, 38:301–326, 2009.

[120] K Sekimoto and L Leibler. A mechanism for shear thickening of polymer-bearing surfaces: elasto-hydrodynamic coupling. *EPL (Europhysics Letters)*, 23(2):113, 1993.

[121] Bhargav Rallabandi, Baudouin Saintyves, Theo Jules, Thomas Salez, Clarissa Schönecker, L Mahadevan, and Howard A Stone. Rotation of an immersed cylinder sliding near a thin elastic coating. *Physical Review Fluids*, 2(7):074102, 2017.

[122] Fumio Takemura, Shu Takagi, Jacques Magnaudet, and Yoichiro Matsumoto. Drag and lift forces on a bubble rising near a vertical wall in a viscous liquid. *Journal of Fluid Mechanics*, 461:277–300, 2002.

[123] Anne-Sophie Bouchet, Colette Cazeneuve, Nawel Baghdadli, Gustavo S Luengo, and Carlos Drummond. Experimental study and modeling of boundary lubricant polyelectrolyte films. *Macromolecules*, 48(7):2244–2253, 2015.

[124] Baudouin Saintyves, Theo Jules, Thomas Salez, and L Mahadevan. Self-sustained lift and low friction via soft lubrication. *Proceedings of the National Academy of Sciences*, 113(21):5847–5849, 2016.

[125] Heather S Davies, Delphine Débarre, Nouha El Amri, Claude Verdier, Ralf P Richter, and Lionel Bureau. Elastohydrodynamic lift at a soft wall. *Physical review letters*, 120(19):198001, 2018.

[126] Bhargav Rallabandi, Naomi Oppenheimer, Matan Yah Ben Zion, and Howard A Stone. Membrane-induced hydroelastic migration of a particle surfing its own wave. *Nature Physics*, 14(12):1211–1215, 2018.

[127] Erina Sawaguchi, Ayumi Matsuda, Kai Hama, Masafumi Saito, and Yoshiyuki Tagawa. Droplet levitation over a moving wall with a steady air film. *Journal of Fluid Mechanics*, 862:261–282, 2019.

[128] Kenneth Langstreth Johnson, Kevin Kendall, and aAD Roberts. Surface energy and the contact of elastic solids. *Proceedings of the royal society of London. A. mathematical and physical sciences*, 324(1558):301–313, 1971.

[129] Zaicheng Zhang, Vincent Bertin, Muhammad Arshad, Elie Raphael, Thomas Salez, and Abdelhamid Maali. Direct measurement of the elastohydrodynamic lift force at the nanoscale. *Physical Review Letters*, 124(5):054502, 2020.

Publications

Abdelhamid Maali, Rodolphe Boisgard, Hamza Chraibi, **Zaicheng Zhang**, Hamid Kellay, and Alois Würger. Viscoelastic Drag Forces and Crossover from No-Slip to Slip Boundary Conditions for Flow near Air-Water Interfaces. Phys. Rev. Lett. 118, 084501

Yuliang Wang, Binglin Zeng, Hadush Tedros Alem, **Zaicheng Zhang**, Elisabeth Charlaix, and Abdelhamid Maali. Viscocapillary Response of Gas Bubbles Probed by Thermal Noise Atomic Force Measurement. Langmuir 34.4 (2018): 1371-1375.

Zaicheng Zhang, Vincent Bertin, Muhammad Arshad, Elie Raphaël, Thomas Salez, and Abdelhamid Maali. Direct Measurement of the Elastohydrodynamic Lift Force at the Nanoscale. Phys. Rev. Lett. 124, 054502.

Zaicheng Zhang, Yuliang Wang, Yachine Amarouchene, Rodolphe Boisgard, Hamid Kellay, Alois Wüger, Abdelhamid Maali. Near-field probe of thermal capillary fluctuations of a hemispherical bubble. Under Review.

Vincent Bertin*, **Zaicheng Zhang***, Rodolphe Boisgard, Christine Grauby-Heywang, Elie Raphaël, Thomas Salez, Abdelhamid Maali. Non-contact rheology of finite-size air-water interfaces. Under review.